Building a Better Scar:
Reengineering Extracellular Matrix Structure in Dermal Scars

Jade Montgomery

Dissertation submitted to the faculty of the Virginia Polytechnic Institute and State University in partial fulfillment of the requirements for the degree of

Doctor of Philosophy
In
Biomedical Engineering

Robert G Gourdie
Kurtis E Moyer
Steven Poelzing
John C Chappell
Jeffrey W Holmes

December 5th, 2019
Roanoke, Virginia

Keywords: wound healing, connexins, collagen, small animal wound healing model, fibroblasts

Building a Better Scar:
Reengineering Extracellular Matrix Structure in Dermal Scars

Jade Montgomery

Abstract

Cutaneous scars represent a common surgical complication, yet no effective drug therapy for scar treatment currently exists despite huge patient and physician demand. A connexin 43 (Cx43) carboxyl terminus (CT) mimetic peptide, alpha Connexin Carboxy-Terminus 1 (αCT1), has demonstrated efficacy in improving long-term scar appearance in pre-clinical and clinical trials. However, current understanding of the mechanism-of-action by which αCT1 improves long-term scar appearance with early intervention treatment is not well understood.

In vivo: Scar biopsies from 1) human, 2) Sprague-Dawley rat, and 3) IAF Hairless guinea pig trials of αCT1 were examined for collagen matrix structure at 4 weeks (all models), and 2 & 6 weeks (rat and guinea pig models only). Collagen matrix variables examined included local disorganization of the fibers, a variable that is higher in unwounded skin compared to scar tissue, and density of the fibers, which is higher in scar tissue but can also be used as an early temporal marker of the rate of healing.

In vitro: Primary murine dermal fibroblasts were isolated from the whole dermis of 3-4 week old transgenic mice expressing collagen 1(α2) GFP-tpz. Cells were sorted for expression via FACS and plated on prealigned collagen substrate for 7 days under conditions favorable to generating extracellular matrix.

All *in vivo* scar biopsies demonstrated some level of altered collagen matrix structure with αCT1 treatment. Treated scars had higher local disorganization of the collagen fibers within the wound, and an increase in collagen matrix density compared to control at certain earlier timepoints that tended to decrease or disappear at later timepoints. The IAF Hairless guinea pig, a novel splinted wound healing model presented herein, was found to closely replicate the human dermal collagen profile and changes in collagen profile spurred by αCT1, significantly outperforming the traditional rat model. Primary dermal murine fibroblasts treated *in vitro* with αCT1 significantly increased synthesis of procollagen 1, the precursor of collagen 1 necessary for constructing the extracellular matrix, suggesting that at least part of the reason for higher collagen density at early *in vivo* timepoints is due to increased collagen synthesis by fibroblasts.

αCT1 treatment in the early stages of wound healing prompts individual fibroblasts to increase their output of collagen and create a more disorganized early collagen matrix. These early changes potentially spur the long-term scar appearance improvements seen in clinical trials, and provide a basis for future work to discover the cellular pathways to alter in order to improve wound healing and cutaneous scarring outcomes.

Building a Better Scar:
Reengineering Extracellular Matrix Structure in Dermal Scars

Jade Montgomery

General Audience Abstract

Skin wounds frequently result in scars that can range from barely visible to enormous eyesores. Almost everyone will experience at least one skin wound in their lifetime leading to a scar that they wish were less visible, feeding the multi-billion dollar market for anti-scarring agents. However, many of the products on store shelves that claim to reduce scar appearance have not proven those claims. Most of the therapies that do have some degree of scientific evidence to support their claims are difficult to use properly, such as silicone sheeting, and often result in only minor improvements to scar appearance. Alpha Connexin Carboxy-Terminus 1 (αCT1), marketed in clinical trials as Granexin® gel, is a protein-based therapy that works on the cellular level to fundamentally alter the skin's initial reaction to wounding and improving long-term scar appearance. This dissertation explores the link between cellular processes altered by αCT1 and long-term clinical improvements in scar appearance by studying both the extracellular matrix present in the scar in human and animal models and the creation of that extracellular matrix by dermal fibroblasts. In both human and animal models, topical application of αCT1 had no effect on skin surface appearance at early timepoints of 2-6 weeks, correlating with previous research that found scar appearance only improved at 3+ months post-injury. However, deep within the newly constructed tissue of the scar, these studies show the collagen organizational structure of αCT1-treated scars is more similar to unwounded skin and slightly more dense at early timepoints, suggesting αCT1 marginally improved the speed of healing. These findings in humans and animals were also verified in part in cell culture experiments that found dermal fibroblasts increased collagen output in response to αCT1 treatment. A novel wound healing model in the hairless guinea pig, superior at replicating human skin than established models like the rat, is also presented and shown to have effects strongly similar to the human with αCT1 treatment. These results provide a fundamental insight into the mode-of-action by which αCT1 may improve long term scar appearance and identifies early collagen structure as a target for future therapeutics to modify, as well as a new animal model in which to test them.

Dedication

"Dream the world. Not this pallid shadow of reality. Dream the world the way it truly is. A world in which all cats are queens and kings of creation. That is my message. And I shall keep moving, keep repeating it, until I die. Or until a thousand cats hear my words, and believe them, and dream, and we come again to paradise."

"Little one, I would like to see anyone – prophet, king, or god – persuade a thousand cats to do anything at the same time."

- *Sandman* #18 "Dream of a Thousand Cats" (1990)

To the memory of my cats Samurai (02/02/2002 - 01/19/2016) and Sushi (02/02/2002 - 11/26/2019).

May we meet again in dreams.

Acknowledgements

"But this - all of this - is academic. You were made as well as we could make you."

"But not to last."

"The light that burns twice as bright burns half as long – and you have burned so very, very brightly Roy."

- *Blade Runner* (1979)

Set in the dystopian future-past of November 2019

Thank you to my parents, Phil and Kylie Montgomery - their love of bio sci-fi made me this way.

Table of Contents

Table of Figures

Table of Tables

Chapter 1

1 Literature Review

1.1 Cutaneous Scars

Injury to the skin is a common occurrence, whether as minor as a shaving mishap or as major as a limb amputation. After injury, the normal adult wound healing process can result in cutaneous scars that are not only unpleasant to look at, but also stiff, painful, and liable to cause further injury at the wound site, sometimes severely affecting the patient's quality of life[1]. Approximately 234 million major surgical procedures are performed annually, often resulting in significant scarring[2,3].

There is substantial patient and physician demand for an effective, easy to use scar reduction therapy without the side effects of current products. Scar reduction therapies were worth an estimated $16 billion in 2015 - with demand only expected to grow[4]. Despite this heavy demand, the majority of currently available post-surgical scar treatments lack evidence of efficacy[5–7]. The few treatments that have been clinically shown to improve the appearance of scars either seriously interfere with daily activities or have major side effects, and then often only result in minor improvements to appearance and/or mechanical function[7]. Currently, there is no FDA approved treatment for general scar reduction. Although a silicone steroid gel was recently accepted for treatment of hypertrophic and keloid scars[8,9], there is currently no FDA-approved treatment for general scar reduction or indeed a mechanistically based approach to drug-based scar reduction.

1.2 Wound Healing Overview

Wound healing typically progresses in what is typically divided into 4 stages: hemostasis, inflammation, proliferation, and maturation[10].

1.2.1 Hemostasis & Inflammation

Hemostasis begins immediately after the initial insult, with platelets and various clotting factors invading the wound space to create a fibrin clot that prevents further bleeding. After hemostasis is achieved, inflammation begins within an hour of the original injury. Blood vessels dilate and become more porous, allowing inflammatory leukocytes to invade the wound and phagocytize bacteria and dead/damaged cells. Neutrophils phagocytose foreign material, bacteria, and damaged tissue within the wound space. Macrophages arrive shortly thereafter, continuing the phagocytosis process initiated by neutrophils and secreting cytokines. Both macrophages and platelets release transforming growth factor beta-1 (TGF-β1)

and TGF-β2 into the wound site, while TGF-β3 is only generated by macrophages[11]. While the role of these inflammatory leukocytes in cleansing the wound space of potentially harmful material is indisputable, the inflammation stage appears to be one of the biggest double-edged swords in adult wound healing. Previous research has found that reducing inflammation and shortening the time that leukocytes spend within the wound space leads to faster wound healing by allowing the proliferative stage to proceed earlier.

1.2.2 Proliferation

The proliferative stage typically occurs within 2 days of injury, and is when angiogenesis, epithelialization, and fibroblast invasion of the wound occurs[12]. Spurred by growth factors, including TGF-β1[13], fibroblasts proliferate and travel through the fibrin clot, degrading the preliminary matrix consisting of fibrin, fibronectin, and hyaluronic acid formed by the initial clot and leaving behind type III collagen fibers and other extracellular matrix (ECM) proteins in their wake[14–17]. At the skin surface, keratinocytes migrate over the forming granulation tissue to create a new outer layer of epidermis in a process known as reepithelialization[18,19].

1.2.3 Maturation

After sufficient collagen has been deposited within the granulation tissue (scar progenitor) of the wound - usually after about one week – increased tensile forces within the wound and TGF-β1 triggers the conversion of fibroblasts into myofibroblasts, which initiate traction on the newly established collagen matrix, shrinking the wound area[20–24]. Fibroblasts and other cells continue to remodel the granulation tissue during this time, as the wound margins contract inwards due to the contractile action of the myofibroblasts. When the levels of collagen production and degradation equalize, the final stage of wound healing, scar maturation, begins[25,26]. Depending on wound size and shape, this long-term maturation phase initiates between 3 to 21 days post-wounding. During the maturation phase, type III collagen laid down during the proliferative stage is mostly replaced by type I collagen and the entire collagen matrix is repeatedly remodeled and reorganized by fibroblasts for a subsequent year or longer.

1.2.4 Normal Wound Healing Results

Normal unwounded human skin tissue is characterized by highly variable collagen fiber orientation, a structural property that allows it to resist stress in multiple directions[25–27]. In comparison, collagen fibers in remodeled scar tissue are more densely packed and more closely aligned than collagen in undamaged skin. The less variably oriented and more aligned collagen in scar tissue is less resistant to the various stresses that skin experiences and as such is more likely to mechanically fail, increasing the susceptibility

of the scar site to further injury[27]. The more aligned collagen in scar tissue is also the reason for the puckering and striations often seen within this neo-tissue[27].

1.3 Aberrant Wound Healing

The processes discussed so far occur in the typical adult wound healing response. However, there are many ways in which normal wound healing can go awry, with the affected wound either not healing at all or resulting in a visually and/or mechanically problematic scar. Several of these conditions are briefly detailed below.

1.3.1 Chronic Non-Healing Wounds

Chronic wounds encompass the many types of wounds that do not follow the normal stages of wound healing, as outlined above, in a timely fashion. Traditionally, a chronic wound is defined as one that has not progressed far enough in the scar formation process to reconstruct a basic water-tight barrier that is essential to the skin's function and purpose after a period of three months post-injury[28,29]. Chronic non-healing wounds, including diabetic ulcers, venous leg ulcers, and pressure ulcers, represent a critical strain on individual patients and the healthcare industry as a whole, most commonly manifesting secondary to other pathologies and complicating recovery[29,30].

Although the underlying disease state preceding a chronic ulcer can vary greatly, the general cause of most chronic wounds is the same – a significant interruption early in the wound healing process, arresting the wound in a persistent inflammatory state that resists progression to the proliferative and remodeling phases of wound healing. A characterizing marker of chronic wounds is overabundant neutrophil infiltration in the wound area[29,31]. Excessive numbers of neutrophils invade the wound and remain within it, overproducing reactive oxygen species (ROS) and pro-inflammatory cytokines, causing additional cellular and ECM damage which further aggravates the inflammatory response in a vicious cycle[32]. Invading neutrophils also release enzymes such as serine proteases and matrix metalloproteinases (MMPs) that degrade and inactivate growth factors essential to normal wound repair and essential ECM proteins[31,33]. Additionally, the high concentration of neutrophils often doesn't just contain its damage to within the existing wound space, but also frequently extends to the healthy surrounding cells and ECM, leading to a slow (and sometimes not so slow) progression of ulcer size and severity over time[29,32]. The prolonged lack of an adequate skin barrier also makes chronic wounds highly susceptible to infection, which further perpetuates the cycle of inflammation[29,33,34]. In serious cases, the associated tissue necrosis and/or infection can progress far enough that limb amputation becomes necessary.

Underlying pathologies associated with chronic ulcer formation include diabetes, vasculopathies such as venous hypertension or atherosclerosis, and immobility (leading to prolonged sustained pressure on specific areas of the body)[29,30,33,34]. Advanced age also increases chronic wound risk, with increased age specifically linked to earlier neutrophil invasion in wounds and a general increase in underlying inflammatory factors[29,35].

Essentially, chronic non-healing wounds are caused by a sustained inflammatory response that is pathologically severe enough that the wound healing process is indefinitely suspended. Any attempts to proceed with the normal wound healing process, such as angiogenesis and the construction of ECM, are blocked by increased release of pro-necrotic factors that damage and degrade cellular and extracellular structures[29,30,32–35]. The necrotic tissue then causes further recruitment of inflammatory cells and has increased susceptibility to infection which even further aggravates the inflammatory response, resulting in a vicious cycle of inflammatory upregulation that outright prevents the formation of even a basic collagen matrix skin barrier at the site of injury.

1.3.2 Fibrotic Scarring

Fibrosis is a disease state characterized by excessive and structurally distorted deposition of collagen within body tissues. In the skin, fibrosis manifests as hypertrophic scarring and keloid formation[31]. Hypertrophic scars and keloids are both loosely characterized by an extreme overabundance of collagen deposition at the wound site, leading to an overgrown visually- and mechanically-unappealing scar. Although hypertrophic scars and keloids may seem superficially similar, these two types of excessive scarring have different presentations and subsequent outcomes[1].

Hypertrophic scars typically manifest relatively early in the wound healing process, becoming apparent between 4-8 weeks after the initial injury and growing for up to 6 months[36–38]. They most commonly form following injuries at sites of significant mechanical, inflammatory, or ulcerative stress[37,39]. Hypertrophic scars are typically “puffy”, extending above the surface of the skin, and often cause mild-to-moderate discomfort including pruritus associated with the general area[1,36,37]. The prognosis for hypertrophic scars however is usually fairly good – following the initial 6 month period of rapid growth, hypertrophic scars typically then gradually regress over time. Eventually, after several years of healing, previously hypertrophic scars are often completely flat and otherwise indistinguishable from normally healed scars[1,38]. In cases of extreme hypertrophic scars that the patient cannot wait several years to normalize, scar removal surgery is recommended as recurrence of the hypertrophic scar following removal is exceedingly rare[40,41].

Keloids, on the hand, can spontaneously occur even years after the initial injury has apparently healed without incident, or even in skin locations not known to have ever been previously injured[1]. The prognosis for keloids is also significantly worse. Unlike hypertrophic scars, keloids typically persist and do not regress after several months[1,42]. Scar removal surgery is also not typically recommended, as the most likely outcome post-surgery is the recurrence of the keloid at the site[40,41]. Keloids, unlike hypertrophic scars, appear to have a strong genetic component[43]; more than half of all keloid scarring patients report a familial history of keloids[44], and several genes have been specifically linked to an increased chance of keloid formation[45,46]. While both keloids and hypertrophic scars can cause discomfort and itching for the patient, keloids can also in some cases become extremely sensitive to physical touch and/or become the source of significant pain to the patient[36,37].

The histological presentation of hypertrophic scars and keloids also differs in key ways. While both aberrant scar types are characterized by excessive collagen deposition, hypertrophic scars are primarily constructed of type III collagen[47], which is often described as a "more immature" collagen type since it is also present in higher ratios in the early stages of normal scar formation[48]. The primarily type III collagen matrix is also typically highly organized in the same way as a normal excisional scar in the direction of mechanical tension, parallel to the skin surface[47]. Keloids, meanwhile, are typically composed of a mixture of type I and type III collagen[1,47], which would be the same collagens one would expect to see in a normal maturing scar undergoing remodeling or even unwounded skin[48]. The collagen matrix in a keloid is also typically overall more disorganized than that of a hypertrophic scar, but locally highly oriented and organized into thick collagen bundles sometimes referred to as "keloidal collagen"[1,47,49,50].

Generally, both neoplastic scar types appear to be a failure of the body to downregulate the normal wound healing response after wound healing has sufficiently progressed. Like the opposite problem of chronic non-healing wounds, this failure to downregulate has been linked to an aberrantly persistent inflammatory phase[50,51]. Unlike chronic wounds however, where the wound is unable to progress to reconstructing the ECM, the inflammatory response is not severe enough to completely impede wound healing progression. Instead inflammation merely persists in the background as the process progresses, continuing well into the remodeling phase when hypertrophic and keloid scars begin to manifest and affecting the formation of the fundamental scar ECM structure[1,7,48,51]. But while hypertrophic scarring appears to be a transient failure of the body to downregulate slightly earlier proliferative and remodeling phase responses, that it is capable of later correcting, keloid scarring appears to be a pathological failure

of the body to downregulate later stages of healing and wound maturation that is much more difficult to correct[1,7,47–51].

1.4 Fibroblasts

1.4.1 Fibroblasts in Normal Wound Healing

Fibroblasts are essential to wound healing and scar formation, being the primary cells responsible for ECM deposition and maintenance in all the healthy tissues of the body. In normal cutaneous wound healing, as the early inflammatory phase wanes after 1-2 days, macrophages secrete growth factors that encourage fibroblast infiltration into the wound site, marking the start of the proliferative phase[12]. The invading fibroblast degrades the initial fibrin clot formed by platelets and replaces it with the fundamental provisional ECM scaffold upon which the entire scar will be built[14–17]. Subsequently invading fibroblasts and other cells will use the initial provisional matrix as a guide upon which to adhere, migrate, mature, differentiate, and contract, making fibroblasts an essential building block in the process of scar formation[12,52].

1.4.2 Fibroblast Heterogeneity

Fibroblasts, as a cell type, are most readily identified by their distinct elongated morphology under a microscope. The term “fibroblast” thus refers to an incredibly heterogeneous population that arises from an array of precursor cell types, although they do mostly trace back to the basic mesoderm germ layer formed in the early stages of embryonic development[53]. Identifying one single marker by which “fibroblasts” can all be exclusively identified and differentiated from other cell types has been an objective that many have tried and failed to accomplish. Even within dermal fibroblasts, fibroblast lineage varies wildly based on location[53]. Facial dermal fibroblasts derive from cranial neural crest cells[54–56], dorsal dermal fibroblasts originate in the dermomyotome[57–59], and ventral dermal fibroblasts derive from the lateral plate mesoderm[60–62].

Dermal fibroblasts within the same skin region also differ dependent on their depth into the dermis. Papillary dermal fibroblasts and reticular dermal fibroblasts have been identified to have distinct gene expression patterns and perform different functions[53,63]. For example, papillary dermal fibroblasts have been found to uniquely support initiation of hair follicle development during initial embryonic development[64–66]. One notable drawback of the normal adult wound healing process is the inability to adequately restore hair follicles. As such, multiple studies have attempted to identify the cellular signal that leads papillary fibroblasts to initiate hair follicle growth[67,68]. So far WNT/β-catenin signaling has been

identified as an upstream regulator, but the exact mechanism remains elusive[53,64]. Reticular fibroblasts, on the other hand, play a much larger role in normal wound healing than papillary fibroblasts[53,63,69]. In a mouse model of wounding, Driskell et al found the fibroblast population in the wound bed at 7 days consisted exclusively of reticular fibroblasts. Only by day 17 had papillary fibroblasts invaded the wound space, and they were located only in a small area immediately below the epidermis[63].

Identifying a cell as a fibroblast is useful in designating its function as a primary constructor, modulator, and maintainer of the extracellular matrix. However, it is important to keep in mind the varying cell lineages can result in wildly differing responses and behavior in fibroblasts and subsequent ECM outcomes, even in fibroblasts isolated from the same patient, dependent on their positional identity[70,71]. Experiments that reciprocally-transplanted murine adult dorsal and oral mucosa tissue and then injured the transplanted sections found conservation of the original tissue type's scarring phenotype, indicating that cellular positional identity plays a larger role in wound healing than host microenvironment[53,69]. However, other experiments have shown that human dermal fibroblast identity can be reprogrammed[72], opening the door for modulation of fibroblast positional identity and function for improved scar healing outcomes.

1.4.3 Fibroblasts as Essential Regulators of Structural Skin Repair

Beyond their role in rebuilding and maintaining the ECM, fibroblasts have also been identified as essential in initiating the regeneration of structures necessary to normal skin architecture. As discussed above, papillary fibroblasts are necessary for the initiation of hair follicle growth both during embryonic development and spontaneous hair follicle regeneration in the excisional wound bed as observed in rodents. Both processes rely on WNT signaling and the presence of papillary fibroblasts[64,73,74], but unlike embryonic development, wound induced hair follicle neogenesis also depends on Fgf9 signaling generated by the immune system[73].

Plikus et al also recently identified another role of fibroblasts in regenerating essential skin components that relies on the presence of those de novo generated hair follicles in the wound space. Neogenic hair follicles, themselves initiated by the presence of papillary fibroblasts, triggered bone morphogenetic protein (BMP) signaling which activated adipocyte transcription factors and prompted the reprogramming of murine myofibroblasts and human keloid fibroblasts into adipocytes, repopulating the wound space with cutaneous fat cells present in normal unwounded skin[75].

1.4.4 Fibroblast Response to Mechanical Signaling

Perhaps naturally as the cells in charge of extracellular matrix building and maintenance, fibroblasts are highly sensitive to mechanical cues. Exerting forces on fibroblast-populated collagen gels *in vitro* causes cell-mediated changes in collagen matrix alignment and directs fibroblast movement dependent on the exerted strain[76–79]. The reorientation and directed migration spurred by mechanical strains requires the proper functioning of various integrins and focal adhesion kinase (FAK) at focal adhesions contacting the extracellular matrix[80–83]. Increases in strain and mechanical stiffness are also associated with upregulation of $\alpha_V\beta_3$ integrin and alpha smooth muscle actin (αSMA) in fibroblasts, early markers in the differentiation of fibroblasts into myofibroblasts which are necessary for contracting the maturing wound[80,84–86].

1.5 Connexins

Connexins are a class of transmembrane proteins that form channels through the cell membrane, either directly linking adjacent cells through gap junctions or allowing extracellular communication through hemichannels. A single hexameric connexin assembly is termed a 'connexon' and on its own forms a hemichannel linking the extracellular space with the cytosol. Two docked connexons in neighboring cell membranes form a single gap junction, which cluster together in gap junction plaques. There are a multitude of different connexin isoforms, which primarily differ in cytosolic carboxyl terminus (CT) length and sequence[87]. In dermal cells, the primary connexins expressed are connexin 26 (Cx26), Cx30, Cx31.1, and Cx43, the latter of which has been studied most extensively as a potential target for scar reduction.

1.5.1 Connexin 43 (Cx43) Overview

Connexin 43 (Cx43) is a 382 amino acid length protein, with the Cx43 CT compromising ~40% of the total length[87–89]. Cx43 has four intracellular and three intracellular portions, traversing the cell membrane four times, with both the N-terminus (NT) and CT terminating inside the cell (Figure 1). The Cx43 sequence is highly conserved across vertebrate species, suggesting Cx43 performs roles and functions essential to life that are not fulfilled by alternate connexin isoforms[90,91].

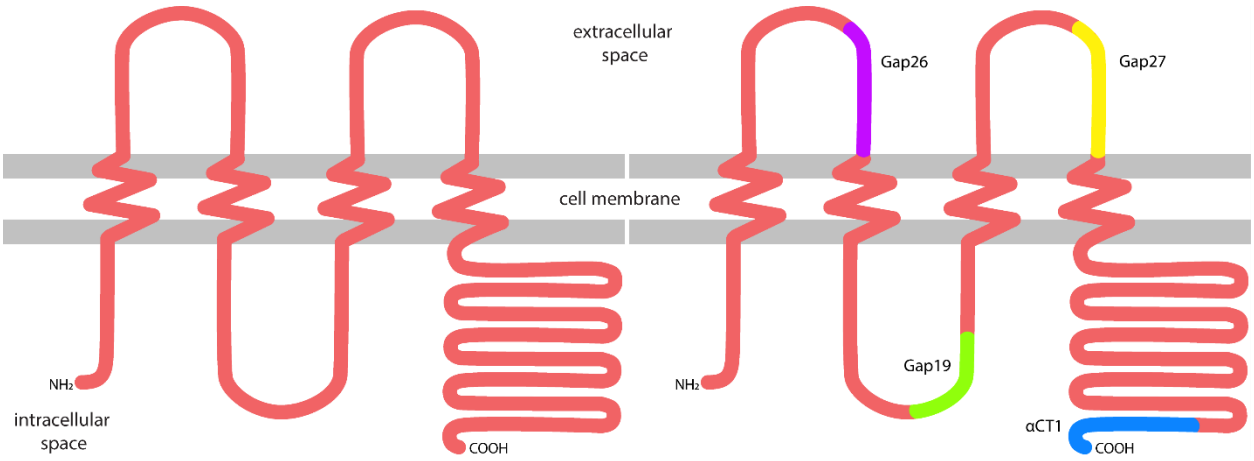

Figure 1: The basic structure of Cx43 (left) with four membrane-spanning domains, two extracellular loops, one intracellular loop, a lengthy CT, and both the amino terminal end (NH_2) and the carboxyl terminal end (COOH) terminating inside the cell. The approximate location of various Cx43 sequence derived peptides, including αCT1, are highlighted (right).

1.5.2 The Role of Cx43 in Wound Healing

Cx43 is expressed throughout the various cells that compromise both the epidermal and dermal skin layers, and has been shown to have key regulatory assignments in the dermal injury response[5,92–104]. Downregulation of Cx43 in wounded skin is essential for the normal wound healing process, with Cx43 levels remaining upregulated in chronic non-healing wounds[105]. Genetically reducing the overall level of Cx43 in mice caused wounds to heal more quickly compared to control[106], accelerating re-epithelialization and wound closure rates, increasing dermal fibroblast activity, and enhancing mediators of ECM remodeling[94].

1.6 Alpha Connexin Carboxy-Terminus 1 (αCT1)

To date, multiple drugs have been formulated to target specific sequences of Cx43, with several demonstrating encouraging results thus far. This project focuses on the manufactured peptide alpha Connexin Carboxy-Terminus 1 (αCT1), a peptide mimic of the carboxyl terminus of Cx43[92,97–99,107,108], and also the location of the binding domain for zonula occludens 1 (ZO1). At the molecular level, αCT1 reduces Cx43 hemichannel density and activity within the cell membrane[99]. At the macroscopic level, αCT1 has been shown in clinical and pre-clinical trials to increase wound closure rate, decrease numbers of inflammatory neutrophils, reduce scar tissue area, improve the mechanical properties of scar tissue, and significantly improve the long-term appearance of scars[5,98,109–112]. Scar reduction therapy with αCT1 has recently been approved for phase III clinical trials.

1.6.1 Origin of αCT1

The peptide αCT1 was originally formulated to study the interaction of the Cx43 CT and ZO1[113]. The peptide αCT1 was specifically formulated as a replicate of the CT-end PDZ2-binding domain, attached to an antennapedia sequence to ensure internalization within the cell, where it could compete with Cx43 to bind ZO1. Earlier work had identified that HeLa cells expressing a Cx43 CT tagged with GFP resulted in cells with abnormally large gap junction plaques, while expression of native Cx43 resulted in small, discontinuous gap junction plaques uniformly distributed at cell interfaces[114]. When the GFP tagged Cx43 was expressed in communication competent cells, however, the native small gap-junction phenotype persisted, suggesting that the presence of unobstructed Cx43 CT was sufficient to rescue the abnormal gap junction plaque dynamics of Cx43 CT-GFP[115]. After showing that Cx43 CT GFP-tagging did not interfere with Cx43 turnover, demonstrating that the increased gap junction size could not be due to reduced Cx43 degradation at the cellular membrane, the αCT1 peptide was used to demonstrate that the phenotype shown by Cx43 CT-GFP cells was a result of the GFP tag interfering with a ZO1 regulatory mechanism present on the CT, and that regulatory mechanism was specifically linked to the ZO1 binding site present on the most terminal end of the CT. After finding that total levels of Cx43 were unaffected by peptide treatment, it was determined that interfering with the Cx43-ZO1 interaction, or more accurately, αCT1 peptide treatment, causes cellular redistribution of Cx43 from non-junctional hemichannels to gap junction plaques[113,114]. This redistribution of Cx43 into gap junction plaques occurs relatively quickly, within two hours of αCT1 application, and has been shown to be mediated by the loss of ZO1 function spurred by αCT1 competitive binding[99].

1.6.2 Recent Work on αCT1 Mode of Action

Further studies on αCT1 have found that it not only binds the PDZ2 domain of ZO1, as it was designed to do, but also prompts increased phosphorylation of Cx43 at the serine residue located at position 368 (S368)[116]. Jiang et al reported that increased S368 phosphorylation correlated with an interaction between three negatively charged residues on αCT1 and two positively charged lysines (K345, K346) on a short α-helical domain of the Cx43 CT[117]. This increased S368 phosphorylation was found to be essential to the cardioprotective reduction in gap junction remodeling and decrease in arrhythmias caused by αCT1 pretreatment in mouse heart post-ischemia injury[117–119]. The interaction of ZO1 and αCT1 variants incapable of interacting with the Cx43 CT alone provided no cardioprotective effects[117,119]. Interestingly, a follow-up study found that removal of the antennapedia sequence from αCT1, resulting in a short 9-amino acid peptide consisting of just the PDZ2 binding domain (αCT11), had potent cardioprotective

effects even when infused post-ischemic injury[119]. Whether the beneficial effects of αCT1 noted in cutaneous wound healing applications also relies mechanistically on increased S368 phosphorylation has yet to be explored[119].

1.6.3 Application to Wound Healing Studies

Qiu et al, following studies that found upregulation of Cx43 immediately post injury was associated with poor wound healing and scar prognosis, found that application of a Cx43 antisense gel to murine incisional and excisional wounds reduced inflammation and scar formation[103]. Subsequently, suspecting that the reduction of Cx43 hemichannels and activity caused by αCT1 peptide may have a similarly beneficial effect, Ghatnekar et al performed the first αCT1 wound healing studies in murine and porcine models[98]. These initial studies found that αCT1 peptide reduced the initial inflammatory phase and subsequently decreased total scar tissue area while improving post-injury mechanical properties[98]. Since these early pre-clinical trials, αCT1 has progressed to clinical trials in humans for multiple cutaneous applications, including diabetic foot ulcers, corneal injuries, and, of course, cutaneous scarring. Phase II studies of αCT1 treatment on laparoscopic scars found a 47% improvement in treated scars compared to control after 9 months (Figure 2)[120].

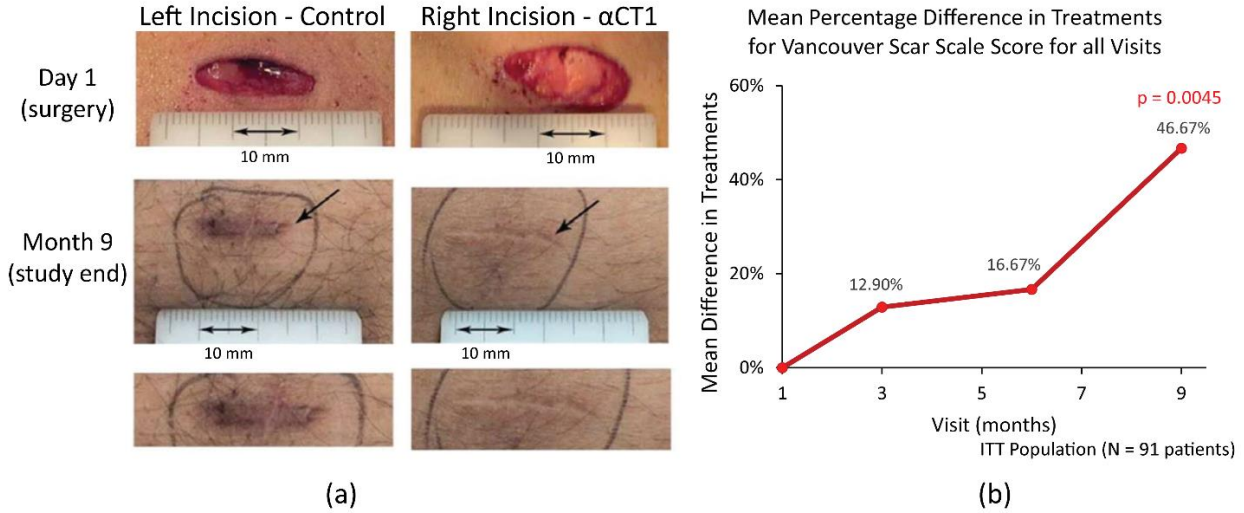

Figure 2: Phase II clinical trial results[112,120]. (a) Treatment and control scars from the same patient immediately after injury (Day 1) and at the conclusion of the study (Month 9). (b) Mean percentage difference in Vancouver Scar Scale Score (VSSS) between treatment and control scar scores for the phase II clinical trials. No difference in scar appearance was seen at 1 month after αCT1 treatment, but by nine months, αCT1-treated scars appeared 47% better than within-patient control scars in the patient population (n=91) and this result was highly significant (p=0.0045).

1.6.4 Preliminary Histological Examination of αCT1 Phase I Clinical Trial Samples

A preliminary structural analysis of haemotoxylin and eosin (H&E) stained biopsy samples at one month from the phase I scar reduction trials of αCT1 (discussed in detail in Section 2.3.2) examined multiple epidermal and dermal parameters within the tissue (Figure 3) using Aperio Imagescope[121]. No difference was found between treatment and control biopsies for epidermal thickness, dermal-epidermal junction length, epidermal length, dermal nuclear count, blood vessel area, rete peg number, or melanocyte count. Sebaceous glands, hair follicles, and eccrine glands were hardly present in the scar biopsies regardless of treatment. The only significant difference identified was in the percent eosin, a metric approximating the extracellular collagen matrix present in the sample obtained through post-imaging image deconvolution. Percent eosin also appeared to vary across the depth of the tissue differently dependent on treatment dose, suggesting depth into the tissue may play a role in these potential collagen matrix changes.

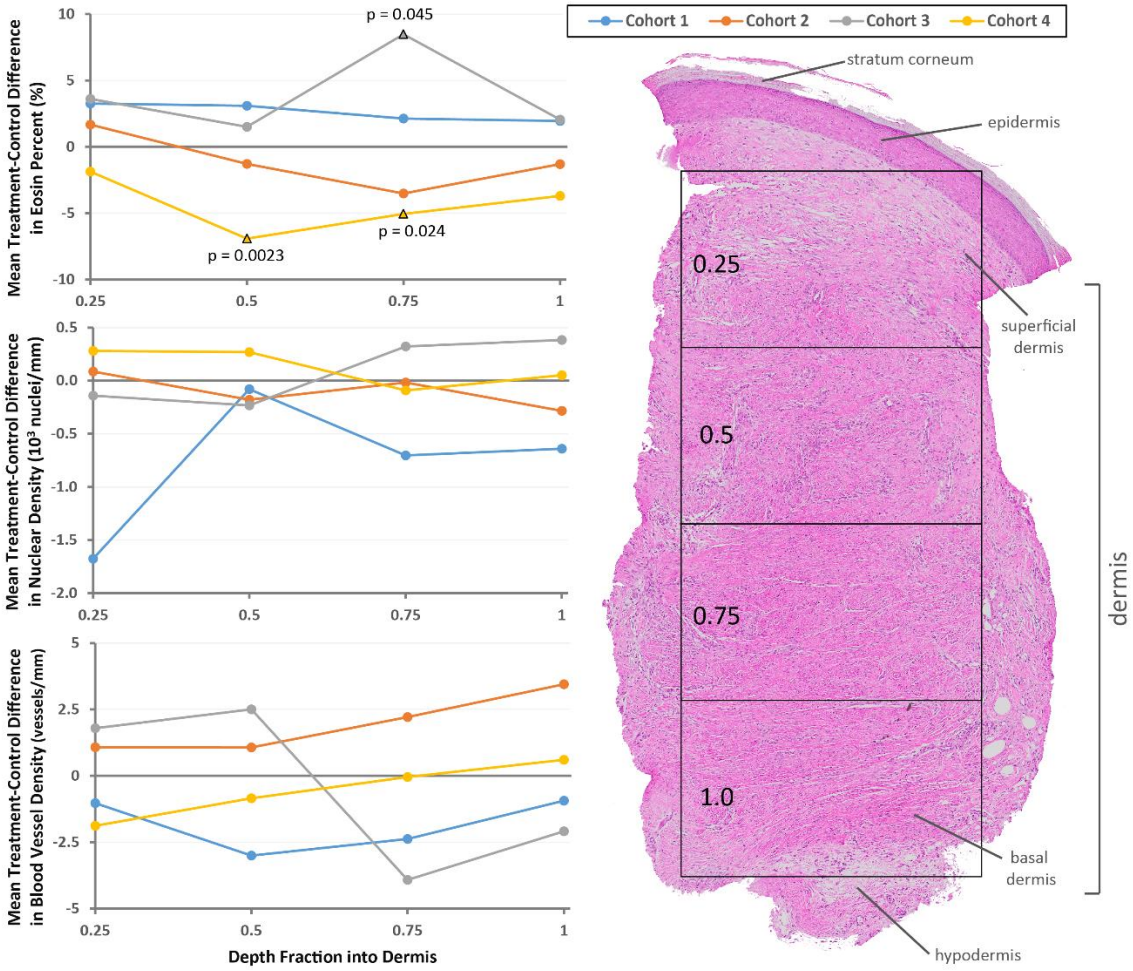

Figure 3: Preliminary H&E analysis of biopsies from the phase I clinical trials. Biopsy dermis was divided into four depthwise sections for analysis as shown (right). Overall percent eosin treatment effect differed across the different dosage cohorts: Cohort 1, 10 μM αCT1 (p=0.2946); Cohort 2, 50 μM αCT1 (p=0.5557); Cohort 3, 100 μM αCT1 (p=0.0777); Cohort 4, 200 μM αCT1 (p=0.0003). Significance at individual depths points (top-left graph) was also found 3/4ths of the way into the tissue in Cohort 3 (p=0.045) and the middle sections of Cohort 4 (p=0.0023, p=0.024).

1.6.5 αCT1-Treated Fibroblasts in 2D Culture

In recent, as-yet-unpublished work, fibroblasts treated with αCT1 in 2D *in vitro* cell culture demonstrated increased speed and more rapid and pronounced changes in orientation. 3T3 fibroblasts were treated with varying levels of αCT1, no peptide, 100 µM reverse peptide or 100 µM antennapedia sequence only. A significant, dose-dependent effect on cell speed and directional persistence was observed in αCT1-treated cultures. At the therapeutic dose of αCT1, 100 µM, fibroblasts were 3 times more likely to change migration direction than control cells (Figure 4).

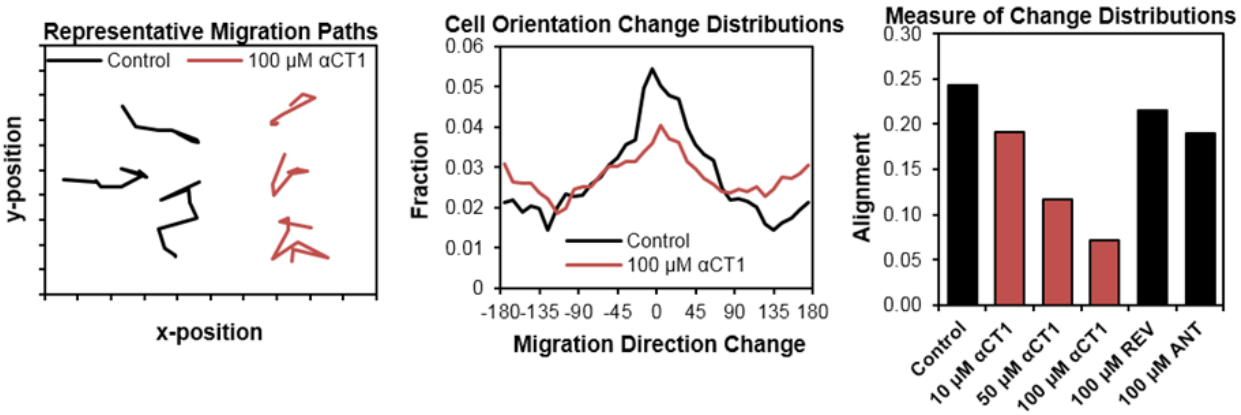

Figure 4: Data from low density fibroblast cultures. From left-to-right: representative paths of 3 control (black) and 100 µM αCT1 treated (red) fibroblasts; fractional distribution of the change in migration direction angle every 60 minutes; fractional alignment measures of the distribution of migration direction angle change where 0 = entirely random and 1 = perfect alignment of migration direction.

1.7 Project Hypothesis

While αCT1 effectively and safely improves scar appearance, the cell and molecular mechanisms accounting for this effect are unclear. The overarching goal of this PhD work was to characterize the mechanistic basis of how αCT1 improves scar appearance. Uncovering this mechanism could lead to targeted uses of the peptide and new therapeutic agents of increased potency.

We hypothesize that αCT1 reduces initial inflammatory response and prompts early activation of resident dermal fibroblasts, modifying the rate, pattern of motion, and collagen synthesis of activated scar-forming cells. We posit that these effects of αCT1 on fibroblast behavior is key to the generation of dermal collagen organization that is more characteristic of unwounded skin and mature collagen fibers deep within dermal granulation tissue during the early stages of scar maturation (1-3 months in human). With ongoing remodeling, these changes in deeper collagen order become manifest at the skin surface over time, resulting in the improvements in clinically assessed scar appearance that were reported to emerge at 6-9 months in phase II clinical testing of αCT1[120].

Chapter 2

2 Aim 1

2.1 Abstract

Introduction: Cutaneous scarring treatments represent a hugely unmet clinical need. Alpha Connexin Carboxy-Terminus 1 (αCT1) is a peptide mimic of the PDZ2 binding domain present on the carboxyl terminus of connexin 43 (Cx43) that has shown efficacy in pre-clinical and clinical studies. In a phase II clinical trial on human laparoscopic scars, αCT1 treatment in the first two days post-wounding resulted in nearly 50% improvement in scar appearance at 9 months. However, the mechanism of action by which short-term αCT1 treatment improves long term scar appearance remains to be elucidated.

Objective: Human cutaneous scar samples at one month post-wounding from the phase I clinical trials treated with αCT1 were examined for structural changes in the collagen matrix that could provide an early structural foundation for long-term improved scar appearance.

Methods: Four cohorts of varying αCT1 dose (10, 50, 100 & 200 μM) treated human clinical trial scar biopsies from 29 days post-wounding were stained for picrosirius red to enhance the natural birefringence of collagen and then imaged at (1) one polarization angle or (2) multiple overlapping polarization angles. Images were analyzed via a semi-automated MATLAB program for structural collagen matrix variables including local fiber disorganization/orientation entropy & fiber density along the depth into the dermis.

Results: When imaged at only a single polarization angle, a heavily depth-dependent αCT1 treatment difference in local collagen fiber disorganization and density emerged in cohort 3, where patients received the therapeutic 100 μM dose of αCT1. However, when imaged at multiple polarization angles, obtaining the full breadth of the collagen fibers contained within the sample, an overall αCT1 treatment effect on collagen fiber disorganization ($p=0.0076$) and disorganization variance ($p=0.0097$) for the entire length of the dermis emerged, although the effect was still strongest in the basal part of the dermis. The depth dependent increase in collagen density with treatment also disappeared with imaging at multiple polarization angles, but a notable trend in overall collagen density ($p=0.0666$) remained.

Conclusions: Treatment with 100 μM αCT1 peptide causes structural changes in the collagen matrix of human scars at 1 month post-wounding, most notably a significant increase in the disorganization of the collagen fiber arrangement. A major difference between unwounded skin and excisional scar tissue is the high alignment of collagen relative to the surface in the scar due to mechanical forces in the healing wound. A greater disorganization of collagen within the scar tissue will theoretically render the scar physically and mechanically more similar to surrounding unwounded tissue.

2.2 Introduction

Cutaneous scars represent a significant part of clinical practice across the world, and encompass a wide array of injuries from extremely minor to immediately life-threatening. Often, in the course of remedying other maladies, it is necessary to surgically injure the skin in order to access the body's internals. While surgical practice has aimed to reduce the extent of skin injury during surgery with techniques such as laparoscopies, often it is unavoidable, especially in emergency situations. Approximately 234 million major surgical procedures are performed annually worldwide, often resulting in significant scarring[2,3].

Connexins are a class of transmembrane proteins that form channels through the cell membrane, either directly linking adjacent cells through gap junctions or allowing extracellular communication through hemichannels. In dermal cells, the primary connexins expressed are connexin 26 (Cx26), Cx30, Cx31.1, and Cx43. Cx43 is expressed throughout the various cells that compromise both the epidermal and dermal skin layers, and has been shown to have key regulatory assignments in the dermal injury response[5,92–104]. Downregulation of Cx43 in wounded skin is essential for the normal wound healing process, with Cx43 levels remaining upregulated in chronic non-healing wounds[105]. Genetically reducing the overall level of Cx43 in mice caused wounds to heal more quickly compared to control[106], accelerating re-epithelialization and wound closure rates, increasing dermal fibroblast activity, and enhancing mediators of ECM remodeling[94].

Alpha Connexin Carboxy-Terminus 1 (αCT1) is a peptide mimic of the carboxyl terminus of Cx43[92,97–99,107], encompassing the PDZ2 binding domain for zonula occludens 1 (ZO1), and has also been shown to have a key mode of action through the phosphorylation of S368 on the Cx43 CT[117,119]. At the molecular level, αCT1 reduces Cx43 hemichannel density and activity within the cell membrane, sequestering Cx43 in gap junction plaques and reducing the permeability of Cx43-composed channels[99,119]. At the macroscopic level, αCT1 has been shown in clinical and pre-clinical trials to increase wound closure rate, decrease numbers of inflammatory neutrophils, reduce scar tissue area, improve the mechanical properties of scar tissue, and significantly improve the long-term appearance of scars[5,98,109–112].

Treatment with αCT1 is also very simple, making it ideal for clinical intervention or even home use. For scar reduction, the peptide suspended in a gel is applied topically to wounds directly after injury and 24 hours later. No side effects other than increased rate of wound closure and decreased inflammation have been observed in preclinical and clinical trials[5,98,107,109,110,112,120].

Phase II clinical trials for αCT1 were performed on bilateral laparoscopic wounds, with adult patients receiving topical αCT1 treatment immediately after surgery and again 24 hours later on one laparoscopic surgical wound, and an identical wound on the other side of their abdomen, which received standard of care (SOC) in order to provide within-patient controls[120]. The paired surgical wounds were then monitored over the next 9 months. At 1 month, the appearance of treated scars was indistinguishable from control scars. However, after 9 months treated scars showed a dramatic 47% improvement in appearance over control, as shown previously in Figure 2.

This delayed temporal effect, where improvements in surface scar appearance are not apparent for several months or more, is not unusual in scar treatment. Cutaneous wounds seal relatively quickly in normal wound healing, but the remodeling phase of wound healing where the scar structure continues to be slowly adjusted can last up to several years. However, given that the αCT1 peptide itself is not remaining in the scar tissue for 9+ months (and is in fact likely entirely degraded after the first several days), the improvements in scar appearance are likely linked to alterations in the histological structure caused by αCT1 treatment in the early stages of wound healing. If histological differences between treatment and control wounds can be identified, we can begin to understand the mechanism by which αCT1 affects the healing cascade to improve scar appearance.

2.3 Initial Single Polarization Angle Analysis

2.3.1 Rationale

During phase II clinical trials, a significant time component was identified as being necessary for αCT1 scar appearance improvements. At 1 month, αCT1 had no effect discernable from SOC, but at 9 months, αCT1-treated scars showed a 47% improvement in scar score compared to control. To identify the histological antecedents for this long-term effect, examination was undertaken of scar biopsies taken from αCT1- and placebo- treated scars at the end of an earlier phase I trial on the peptide in adult humans, which had concluded at approximately 1 month after skin wounding. Preliminary analysis of H&E stained sections found no difference in multiple epidermal and dermal parameters except a rough measure of collagen matrix, so a more comprehensive study of collagen matrix using a collagen birefringence-enhancing stain was undertaken.

2.3.2 Methods Overview

Phase I Clinical Trials

This initial clinical trial on the effect of αCT1 on human dermal wound scars was performed on 49 healthy human volunteers. As shown in Figure 5, on day 1 a biopsy punch was used to create a wound in the unblemished skin underneath both arms. One underarm wound from the patient was treated with an αCT1 gel, while the other wound from the same patient was treated with a placebo gel, enabling within-patient comparisons. Gel was applied immediately after injury and again 24 hours later. The αCT1 dosage in the gel depended on cohort, as shown by Table 1. Cohort 3, 100 µM of αCT1, was the same dosage used in the phase II clinical trial and considered the therapeutic dosage. The wounds were allowed to heal out to 29 days, with photographs taken of the healing wounds at regular intervals. At 29 days, the healed scars were photographed one last time and then biopsied. Biopsied scar tissue was washed, placed in 4% paraformaldehyde for 24 hours, and then embedded in paraffin for sectioning.

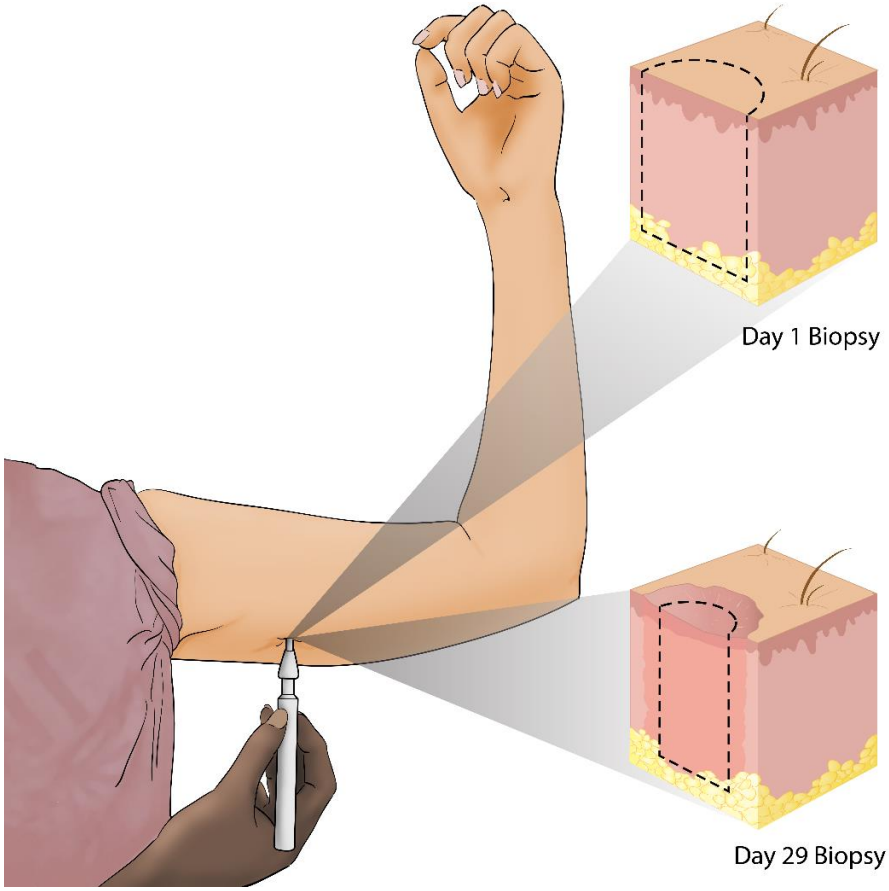

Figure 5: αCT1 phase I clinical trial sampling scheme, performed on healthy human volunteers[112]. The Day 1 Biopsy inset shows a cross-section of unwounded skin with dotted lines indicating the tissue biopsied at the start of the trial to create the study wounds, which were then immediately treated with αCT1 or placebo gel. The Day 29 Biopsy inset shows a cross-section of the subsequent study scar 28 days later, with dotted lines indicating where the center of the scar was biopsied to provide the biopsy sections examined in this chapter.

Table 1: Phase I clinical trial αCT1 dose & total number of patients with (patients included in analysis) by cohort.

Cohort	Dose	N
1	20 µM	12 (10)
2	50 µM	13 (9)
3	100 µM	12 (8)
4	200 µM	12 (10)

Picrosirius Staining

After sectioning, slides holding biopsy sections were stained with Picrosirius red to enhance the natural birefringence of the collagen fibers. Stained sections were then imaged on an Olympus slide scanning scope at 20x under polarized light to obtain whole section images of the collagen structure (Figure 6).

2.3.3 Initial Analysis Methods

Whole-Section Imaging

Whole sections of day 29 scar tissue from individual patients were imaged at 20x at a single circularly polarized light angle on the Olympus VS120 slide scanning scope[122]. A MATLAB[123] program was created and used in concert with the OrientationJ plugin[124] for ImageJ[125] to analyze each whole-section image for local collagen fiber orientation entropy, collagen fiber density, and ratio of red (mature) to green (immature) fibers at each arbitrary depth into the tissue.

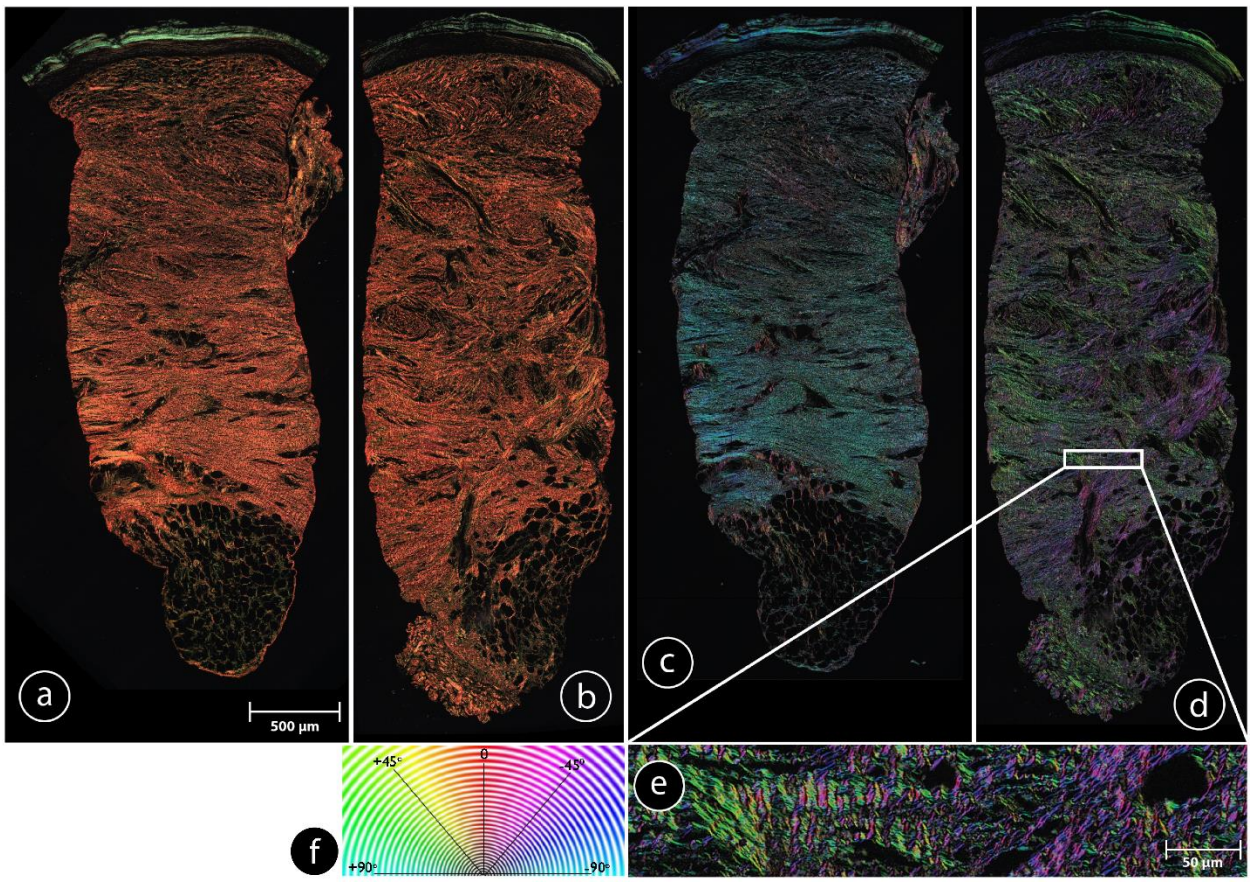

Figure 6: Picrosirius red stained (a & b) whole sections of the phase I biopsies from a single patient highlighting the collagen content, and the same images color adjusted to show collagen fiber orientation (c, d, & inset e) according to the color map key provided (f). The left arm was treated with a placebo (a & c), while the right arm was treated with 100 µM αCT1 (b, d, & e).

Orientation Entropy

The orientation of each image was calculated using the color map option in the OrientationJ plugin[124] available for ImageJ[125]. OrientationJ evaluates the local orientation and coherency of every pixel within the image based on structure tensor computation from a grayscale input image[124,126–128]. The color map option outputs these per-pixel calculations in an HSB image/matrix (shown in Figure 6c,d,e) where hue represents orientation angle based on the map code shown in Figure 6f, saturation represents coherency, and brightness comes from the source grayscale image[126].

These color map images were then fed into MATLAB[123], masked for tissue presence, oriented dependent on tissue depth, and broken into depth-wise regions for analysis after thresholding for coherency. These depth-wise regions were further broken into smaller areas which were then analyzed using the built-in entropy function[129,130] to give local orientation entropy for the area. The area local orientation entropy

was averaged over the depth region to give a mean local orientation entropy per depth per image for statistical analysis.

Collagen Density

Collagen density was calculated from the images on a depth-wise basis in a standard manner. Briefly, the original unadjusted picrosirius red stained images were fed into MATLAB[123], masked, oriented, and broken into depth-wise regions identically to the color map images above. The images were then converted to binary images by thresholding for brightness using both the inbuilt MATLAB function "graythresh"[131], which uses Otsu's method to compute a global image threshold[132], and a user-designated numeric cutoff. The sum of occupied pixels for each depth region was then divided by the total number of pixels in the depth region. Minimal differences were found between the densities calculated by the inbuilt MATLAB function vs the user-designated cutoff, so all density metrics presented in this paper are based on the inbuilt MATLAB function "graythresh"[131] calculations[132].

Red/Green Ratio

Traditionally, picrosirius red collagen images have been presumed to show "mature" type I collagen as red/orange fibers and "immature" type III collagen as green fibers[133,134] (for a more in-depth discussion, please refer to Section 5.2.1). To calculate this metric, the original unadjusted picrosirius red images were masked, oriented, and broken into depth-wise regions as above. The regions were then split into two binary images – one containing those pixels with hue 0-50 & 300-359 (red) and brightness above threshold[131], and one containing those pixels with hue 60-200 (green) and brightness above threshold[131]. The sum of occupied red pixels was then divided by the sum of occupied green pixels to give red/green ratio for the depth region.

2.3.4 Statistics Methods

All depth-wise variables extracted from the whole-section images were analyzed in JMP® Pro 12[135]. To control for within-patient variance and any potential depth-wise effects, a mixed-model analysis was used. Patient designator was set as a random effect, while treatment, depth and their interaction were set as fixed effects. Due to the parametric requirements of mixed-model analysis, data was minimally transformed when necessary to achieve a homoscedastic normal distribution of residuals. Individual treatment to control comparisons at each depth were conducted via Student's t test.

2.3.5 Results & Discussion

Scar Surface Appearance

Overall, the effect on surface appearance of scars was not found to be significant after 29 days (Figure 7). This correlates with the results of the phase II trials, which found no difference in surface scar appearance at 1 month.

Figure 7: Images taken from a single patient in Cohort 3 (therapeutic dose) over the time course of the phase I study. The top image set shows surface images from the patient's right arm that received the control gel (Placebo) while the paired bottom image set shows images from the patient's left arm that received the 100 µM αCT1 gel (Active) from day 1 (D1) of the study, immediately after wounding, to day 29 (D29) of the study, immediately prior to biopsy collection. While this particular patient appears to show early surface improvements with αCT1, the effect was not significant when analyzed over the entirety of the patients in Cohort 3.

Picrosirius Staining

Patients that received only placebo gel treatment in both arms (n=8) or whose biopsies were unusable (n=4) were excluded from the study (n_1=10, n_2=9, n_3=8, n_4=10; $n_{\text{All Cohorts}}$=37; Table 1). At 1 month after treatment, wounds treated with a therapeutic dose of αCT1 (Cohort 3/100 µM) had a collagen matrix that was significantly and consistently less organized, with a denser collection of fibers, and a higher ratio of red to green fibers (Figure 8). However, this collagen organization was not present in the ~1.5 mm superficial half of the dermis proximal to the epidermis, but characterized only the lower half of the scar, continuing all the way to the dermal base where it contacted underlying muscle and fat. Thus, in 100 µM αCT1-treated scar tissue at 1 month after wounding, while the skin surface appeared similar to untreated scar, deep within the granulation tissue the matrix is more similar to that of unwounded skin. Interestingly, when looking at the results of all the cohorts in Figure 9, Cohort 2 (50 µM) seemed to have a similar but delayed effect, potentially indicating a dose-dependent effect.

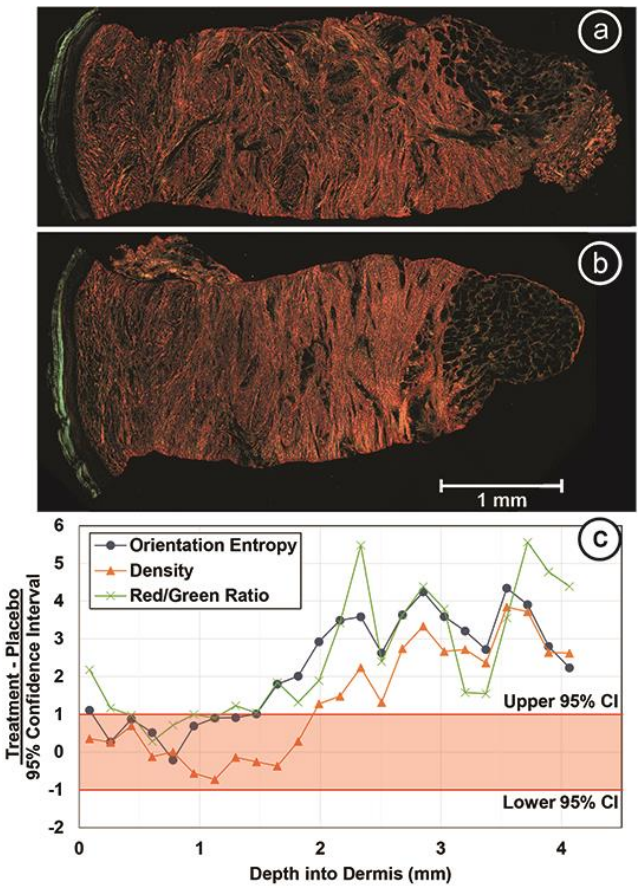

Figure 8: (a) αCT1 and (b) placebo scar tissue biopsies from the same patient at 29 days post-wounding, left-to-right superficial-to-deep. Graph (c) compares the collagen matrix of treatment and placebo biopsies from all analyzed patients in Cohort 3 (n=8) by dermal depth. Data points outside the red shaded area are significant ($p<0.05$).

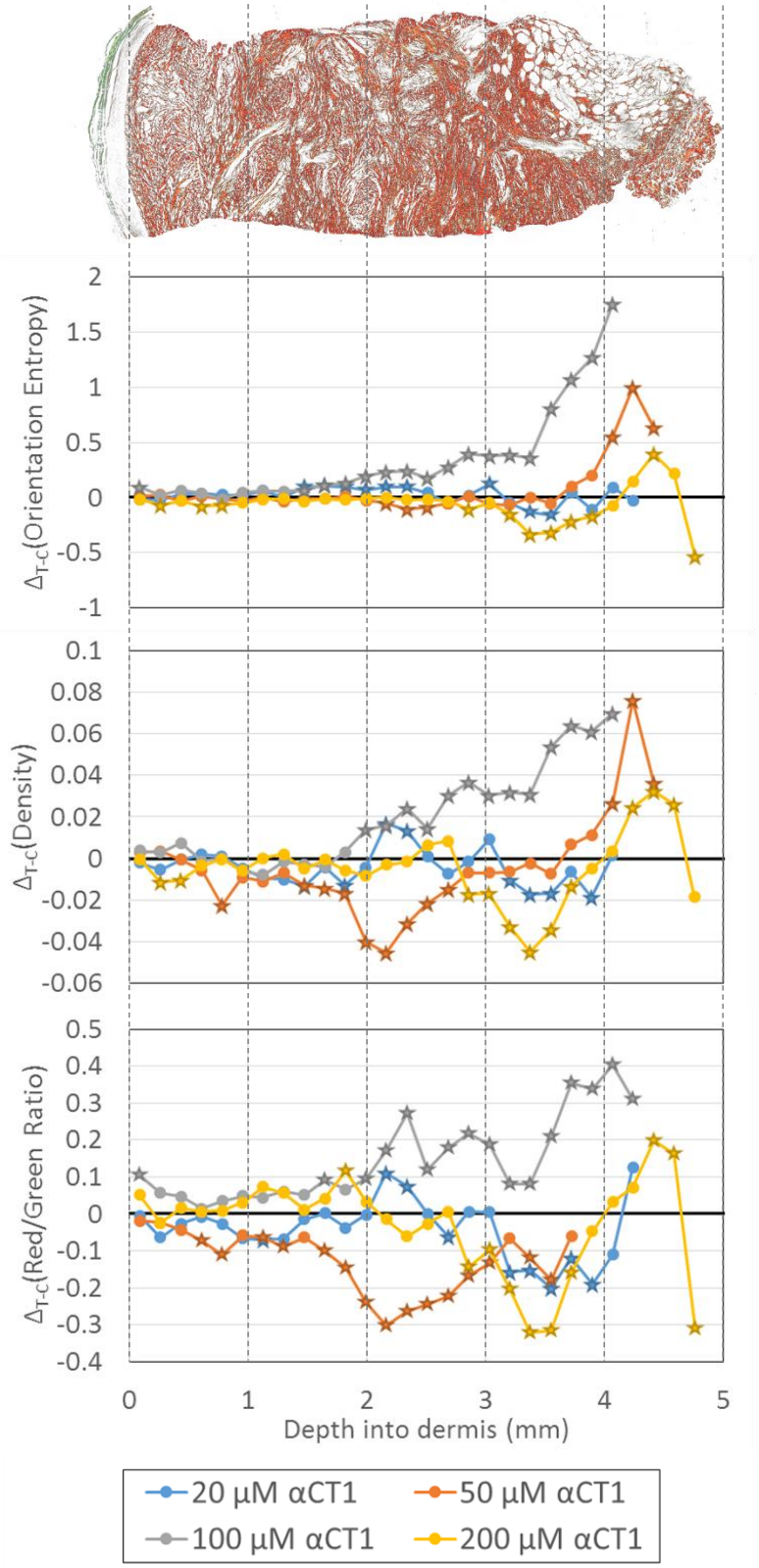

Figure 9: Difference between treatment and control biopsies for collagen fiber orientation entropy, collagen fiber density, and ratio of red (mature) to green (immature) fibers for each phase I dosage cohort, from the most superficial part of the dermis (right) to the deepest part of the dermis (left). Stars indicate a statistically significant difference between treatment & placebo.

One result that might seem contradictory is the observed increase in collagen density with treatment. Scar tissue is already more dense than the original skin tissue, and this can cause a wide range of mechanical problems. However, it is important to note that these samples were taken at 4 weeks. The scar collagen matrix is continually built up in the weeks following injury, and a large excisional wound like the punch biopsy used in this study can take 6 weeks or longer to approach what will be the final collagen density of the scar. Previous work on the αCT1 peptide has found that it both decreases the length of the initial inflammatory phase (allowing fibroblasts to invade earlier), and increases the speed of fibroblast movement, both of which would allow the fibroblasts to speed up the initial construction of the collagen matrix. Considering the long term benefits of αCT1 on scar appearance, it is likely that the increases in density are only transient and that the final collagen density of the scar at 6+ weeks is the same regardless of treatment.

2.3.6 Conclusions

Using scar tissue samples taken at day 29 during the phase I clinical trial, it was determined from an analysis of collagen labeled by picrosirius red-enhanced birefringence at a single polarization angle that αCT1 prompted a change in collagen organization deep within the dermis at this single time point after wounding. The differences in deep collagen organization observed between treated and untreated wounds suggest that remodeling by dermal fibroblasts proceeds over time from the base of the scar's plug of granulation tissue upwards towards the epidermis. Our data indicates that targeting this bottom-up process of collagen remodeling may provide a therapeutic strategy for beneficially modifying scar appearance.

2.4 Multiple Circular Polarization Angles Analysis

2.4.1 Rationale

After the initial analysis was completed, additional questions surrounding the data arose. Circularly polarized light allows one to image the birefringent collagen fibers in a sample without much interference from other tissue components. However, the birefringence of collagen highly depends upon the orientation of the particular fiber. At a single circularly polarized angle, one can only see collagen fibers at perpendicular angles with a small margin of error, which can lead to underestimation in both the density and array of angles of the collagen fibers present in a sample. A fully accurate analysis of the clinical trial biopsy samples requires imaging at sufficient, consistent circular polarization angles in order to capture the entire array of collagen fibers present in the samples followed by statistical analysis of this complete collagen matrix.

2.4.2 Methods

In order to capture the full breadth of the collagen fibers present in the system, an Arduino-based[136,137] microscope addition capable of rotating the microscope condenser and analyzer in unison was constructed (Figure 10). A user interface system allows the microscope user to specify a condenser angle, upon which point step motors actuate gears 3D printed with a MakerBot Replicator 3D printer[138] that interface with the native Olympus VS120 scanning microscope[122] polarization condenser[139] and rotatable analyzer[140]. Slides were serially imaged at six polarization angles - 0°, 15°, 30°, 45°, 60°, & 75° - in order to obtain the full array of collagen fibers present in the sample with some overlap. A MATLAB[123] program was written to combine these six separate images and process them as one sample, using the MatFiber function[141] to tally the fiber angles present in each image. Samples were analyzed along the depth of the tissue for collagen fiber density, local circular variance, local circular variance adjusted for local density ("collagen disorganization"), and standard deviation of collagen disorganization ("collagen disorganization variance"), which was used as a rough measure to identify where the tissue had regions of both high and low collagen disorganization in close proximity to one another. Statistics were analyzed as detailed in Section 2.3.4 above.

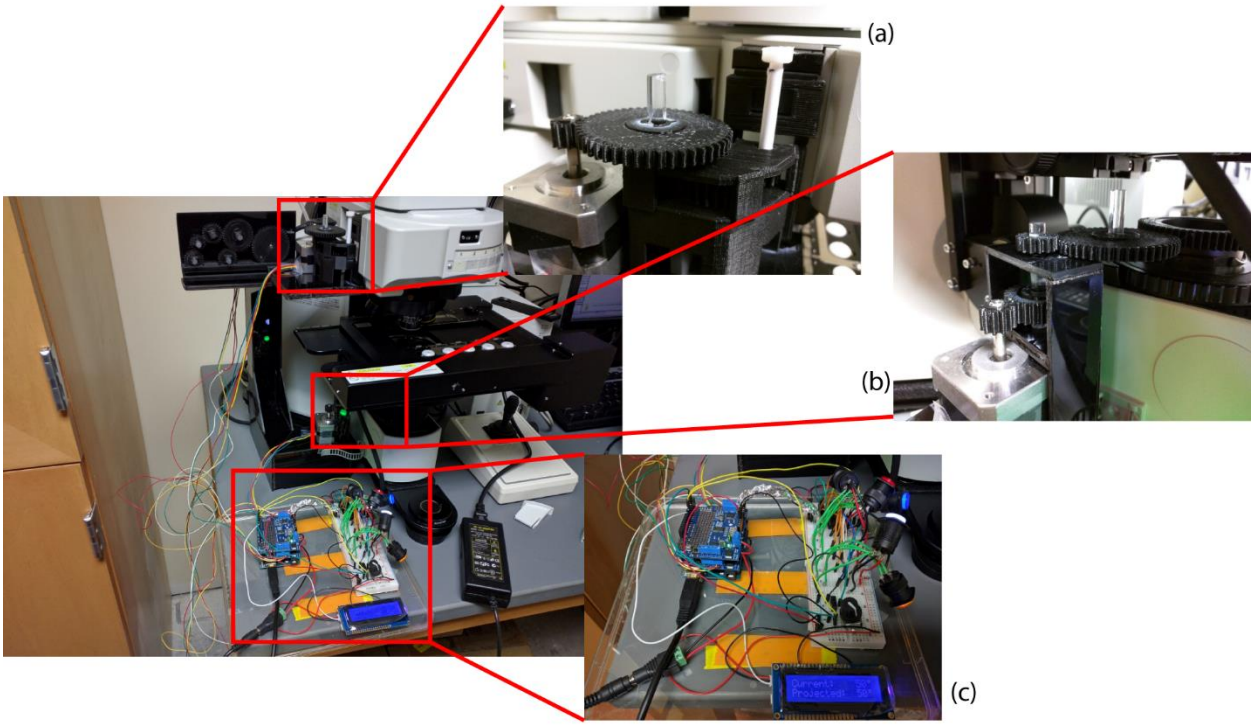

Figure 10: Microscope addition allowing imaging at multiple consistent polarization angles. The left image shows the full addition in place on the Olympus VS120[122], with inset (a) showing the upper motor-analyzer interface, inset (b) showing the lower motor-condenser interface, and inset (c) showing the user control interface and Arduino[136,142] controller system.

Multiple Angle Image Overlay

Prior to calculation of metrics for statistical analysis, the six independent images compromising the full breadth of fiber angles for each sample had to be overlaid exactly. The inbuilt MATLAB[123] function "normxcorr2"[143] calculates the normalized correlation coefficient matrix for specified 2D image regions and returns the point of best overlap[143–145]. Since the function is highly computationally intensive, and the individual images were very large whole-section images at 20x, 3 user-specified regions per image were compared to find the point of best overlap. When the 3 regions differed in their calculations, user input guidance was used to specify the point of best overlap. The overlaid image sets were then manually masked for the presence of tissue and oriented to allow depth-wise analysis.

Collagen Disorganization

Using a MATLAB[123] master program, the six angle images from each image set were independently fed into the MatFiber[141] function, which calculates fiber angles based on local gradients. The fiber angle matrices from each image were compiled together for the image set. The tissue matrix was split into regions of similar size dependent on depth, and then further subdivided into small subregions which were used to calculate local circular variance using the "circ_var" function available in the Circular Statistics Toolbox[146]. Circular variance is a measure of the breadth of fiber angles in a sample; a sample with all fibers oriented the same way will give a circular variance of zero, while a sample with all fibers oriented perfectly randomly will approach a circular variance of one[147]. While circular variance is theoretically not dependent on density, a low number of fiber angles present in a sample can skew results. To account for this, local circular variance was weighted by local density for each subregion.

Local circular variance weighted by local density was then averaged across all the subregions present in each depth region per image to give the metric hereafter referred to as "collagen disorganization".

Collagen Disorganization Variance

When comparing the collagen disorganization numbers to the original images, it became apparent that this metric did not fully describe the disorganization present in the tissue that could be observed with the naked eye. Particularly in several αCT1-treated patient samples, highly aligned subregions of tissue were interspersed in between regions of very disorganized fibers, disproportionately dragging down the mean value when averaged across the depth region. To better describe the regional disorganization, the standard deviation of the local circular variance weighted by local density for the subregions in each depth was also calculated and hereafter referred to as "collagen disorganization variance".

Collagen Density

Collagen density was calculated by thresholding the 6 individual images in each set via the inbuilt MATLAB function described previously[131]. The 6 binary images were then combined to form a single stacked binary image. The number of occupied pixels divided by the total number of pixels was calculated for each depth region for statistical analysis, and each subregion as part of the calculation of collagen disorganization and collagen disorganization variance.

2.4.3 Results & Discussion

Polarization Angle Replicates

Analysis of images taken at a single polarization angle revealed a fiber angle distribution approximately ±10° around the primary angles. Therefore, to capture the full collagen matrix in each biopsy section with sufficient overlap, each sample was imaged at every 15° interval between 0° and 90°.

Multiple Polarization Angle Analysis

The largest effect observed from imaging at multiple polarization angles was a significant increase in overall treatment effect for Cohort 3 (Table 2, Figure 11, Figure 12). The effect was still strongest in the basal sections of the tissue nearest the fat layer, but treatment effect in the more superficial and mid sections of the scar was increased by imaging at multiple polarization angles to result in a significant overall treatment effect on collagen disorganization, disorganization variance, and a notable trend in collagen density (Table 2).

Table 2: Overall p values from the statistical analysis of the multiple polarization angle imaged phase I clinical trial samples.

	Cohort	P Values	
		Treatment	Treatment*Depth
Collagen Disorganization	1	0.7007	0.4001
	2	0.4608	0.0111
	3	0.0076	0.9846
	4	0.0766	0.1545
Collagen Disorganization Variance	1	0.1100	0.8266
	2	0.7580	0.0001
	3	0.0097	0.4459
	4	0.5497	0.2267
Collagen Density	1	0.1180	0.8310
	2	0.2605	0.0001
	3	0.0666	0.9974
	4	0.8424	0.7778

For the other 3 cohorts (Figure 11, Table 2), no significant effect was found for cohort 1 (10 μM dose of αCT1) as expected due to the dosage in this group being an order of magnitude lower than the therapeutic dose. Overall treatment disorganization, disorganization variance, and density were all slightly higher than control, but these effects did not approach significance. Cohort 2 (50 μM dose of αCT1) had a significant treatment-depth interaction effect, but no significance overall (Table 2) where the greatest effect was found about midway through the dermis and then sharply tapered off. Cohort 4 (200 μM dose of αCT1) was alone in having a negative trend on the collagen matrix disorganization (Figure 11). This corresponds with previous data that found that while 10-100 μM of αCT1 had beneficial effects on cell migration, a 200 μM dose had a deleterious effect on cells, reducing cell viability.

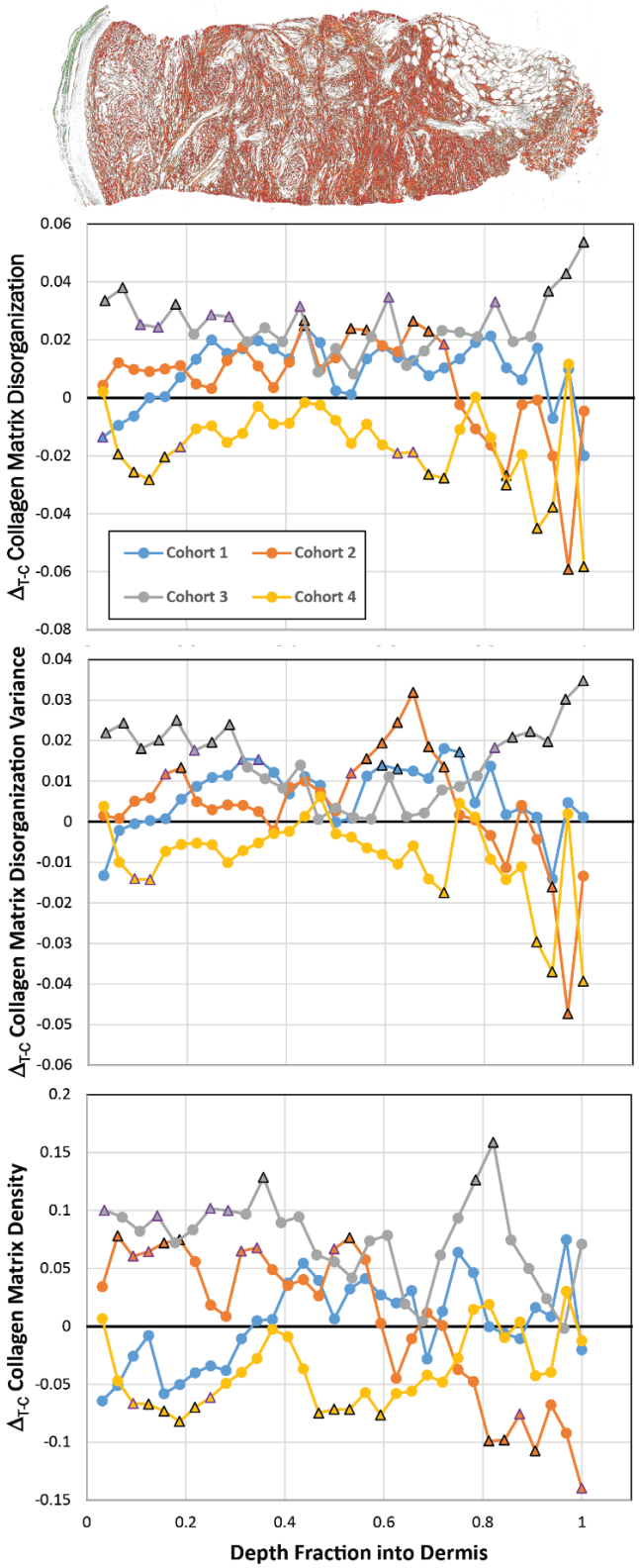

Figure 11: Difference between treatment and control biopsies imaged at multiple polarization angles for the 3 measured metrics (collagen disorganization, disorganization variance, and density) across the depth of the dermis for all 4 cohorts from the phase I clinical trials. Individually significant points ($p<0.05$) are denoted with a black triangle. Individually trending points ($0.05 \leq p < 0.08$) are denoted with a purple triangle.

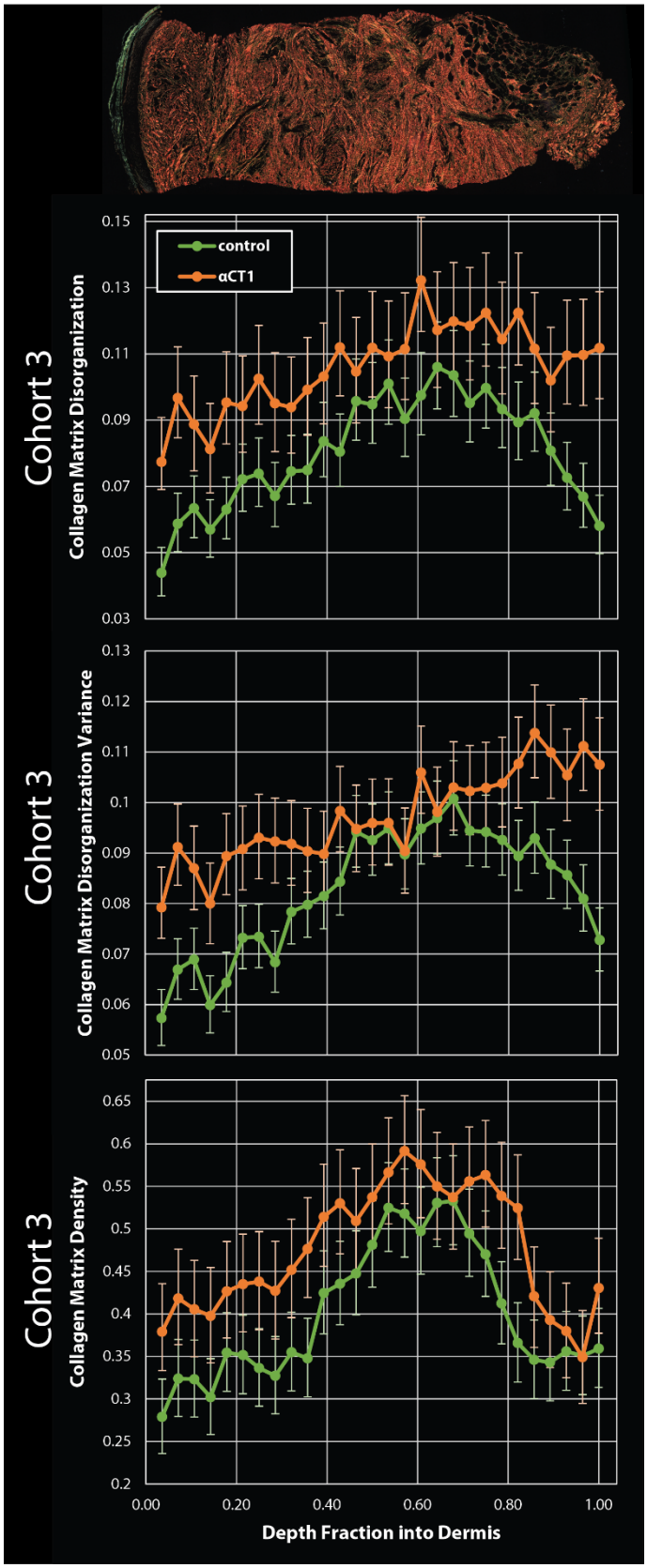

Figure 12: Cohort 3 collagen matrix disorganization, disorganization variance, and density by depth into dermis for treatment (orange) and control (green) biopsy sections imaged at multiple polarization angles. Error bars ± standard error (SE).

Imaging at multiple polarization angles also reduced the significant treatment effect on density in Cohort 3 to only that of a strongly indicative trend (Table 2). This further bolsters the hypothesis that αCT1 may cause a transient increase in collagen density in the early stages of the scar as the treated scar fills in with collagen matrix faster, but that effect disappears as the scar matures and the control scar matrix catches up with the treated scar. However, this theory requires further study to confirm.

2.4.4 Conclusions

Treatment of human phase I clinical trial biopsies with a therapeutic dosage of 100 μM αCT1 led to a significant increase in local collagen disorganization and disorganization variance across the tissue, with a notable trend for overall increased collagen density. The strongest effect was found in the deepest part of the dermis, which may partly explain the delayed skin surface appearance improvements seen in phase II clinical trials at 9 months.

While the initial analysis led us to believe that the treatment effect was entirely depth dependent, increasing the scope of the analysis with multiple polarization angles revealed an *overall* treatment effect with 100 μM of αCT1 that was strongest at the base of the tissue. This demonstrates the importance of understanding the ramifications of collagen's birefringence being dependent upon polarization angle under circularly polarized light and accounting for it in studies, which many in the field fail to do[133,134,148].

Chapter 3

3 Aim 2: Identifying an Animal Model for Replicating Clinical Trial Results

3.1 Abstract

Objective: To identify a small animal wound healing model capable of replicating the αCT1 treatment results observed in previous human clinical trial studies, to allow further histological study of the temporal nature of αCT1-related long-term scar improvements.

Methods: Presupposing the need for replication of the human mechanical wound healing environment, multiple wound splint methods previously established in the literature were tested in an initial study on Sprague-Dawley rats. Afterwards, wound splint studies of rodent excisional skin wounds in two different small animal models, the Sprague-Dawley rat and the IAF Hairless guinea pig, were carried out over the course of six weeks, with paired αCT1 treatment and control wound biopsies collected every two weeks. Scar biopsies were fixed, sectioned, and stained with picrosirius red for analysis. Scars were judged on their overall histological similarity to the human clinical trial scar biopsies, as well as their ability to replicate the organizational changes seen in human scar collagen matrix structure after αCT1 treatment.

Results: (1) Silicone wound splints of 0.8 mm thickness, surrounding 8 mm diameter wounds and secured with 6-8 nylon sutures were identified as the optimal method of wound splinting and employed in the subsequent two studies. (2) Sprague-Dawley rats healed quickly, and demonstrated early αCT1-related improvements in biopsies taken at week 2. Week 4 biopsies from the rat appeared to have healed beyond the human samples at the same time point, and while treatment effects persisted significantly in collagen disorganization variance and marginally in collagen disorganization, the rat wounds had no difference in collagen density between treatments. Complications in the rat model prevented statistical analysis of the week 6 samples. (3) The IAF Hairless guinea pig healed more slowly than the rat model; average collagen density in the week 4 guinea pig samples was slightly less than that of the rat samples at week 2, but this correlated closely with observations in the human samples from Chapter 2. Week 4 & 6 guinea pig scars correlated highly with the human scars, both in general values and profile through the skin thickness of the collagen variables assessed, and effect of αCT1 treatment on the collagen variables tested.

Conclusions: While the rat model is cheaper and requires less IACUC scrutiny, it is a rather poor model of long-term human wound healing. The IAF Hairless guinea pig was superior in every statistical measure, resulting in scars that had similar αCT1 treatment effects and were overall more human-like. The guinea pig was also superior in ease of use, being less antagonistic towards the study implements and maintaining a naturally hair-free environment on which to observe the progress of the healing wound.

3.2 Introduction

The ideal model in which to study the human cutaneous wound healing response is, of course, the human. However, trials in humans are exceedingly expensive and difficult to obtain approval for. A recent study that looked at data from 2015-2016 found that the average price tag of a controlled human trial had soared to US$35M, with some trials costing more than US$347M[149]. Compliance is also a significant problem with trials in humans[150], unlike animal models which can be stringently monitored and controlled.

Porcine models are generally considered the next best model for study, with human and porcine skin being comparable in a number of ways including in skin thickness and reduced number of hair follicles[150–153]. There are still a number of key cutaneous differences between the two mammals though, including a less developed dermal vasculature in the pig[153], but when compared to the majority of other animal models available pig skin appears to be the closest mimic of human skin and thus human cutaneous wound healing. However, porcine models are also considerably expensive to both purchase and maintain. Pig wound studies also require dedicated large animal vivariums that not all institutions maintain, unlike small animal vivariums which are much more common[152].

The biggest benefits of small mammal models, and the reason they are preferred by many researchers over human and pig models, are reduced costs, plentiful supply, and ease of handling[150,153]. Small animals also usually demonstrate accelerated healing speeds when compared to the human, allowing studies to be performed on a much shorter timescale[150]. However, the biggest problem with currently employed small animal models is their low fidelity with the basic structure of human skin. Mice, a commonly employed small animal model, in particular have incredibly thin skin when compared to the human, making histological comparison far more difficult. Mechanical considerations are also an important difference in small animal wounding models. Unlike humans and pigs, which have “tight skin” where the skin is attached to the underlying fat, small animals have “loose skin” that is not attached to the underlying fat (Figure 13). This has the effect of creating a completely different mechanical profile in the healing wound[150–153]. However, there are existing methods to overcome these mechanical differences, most notably the wound splint model where an excisional wound in a small animal model is fixed open by a splint secured to the top of the skin[154].

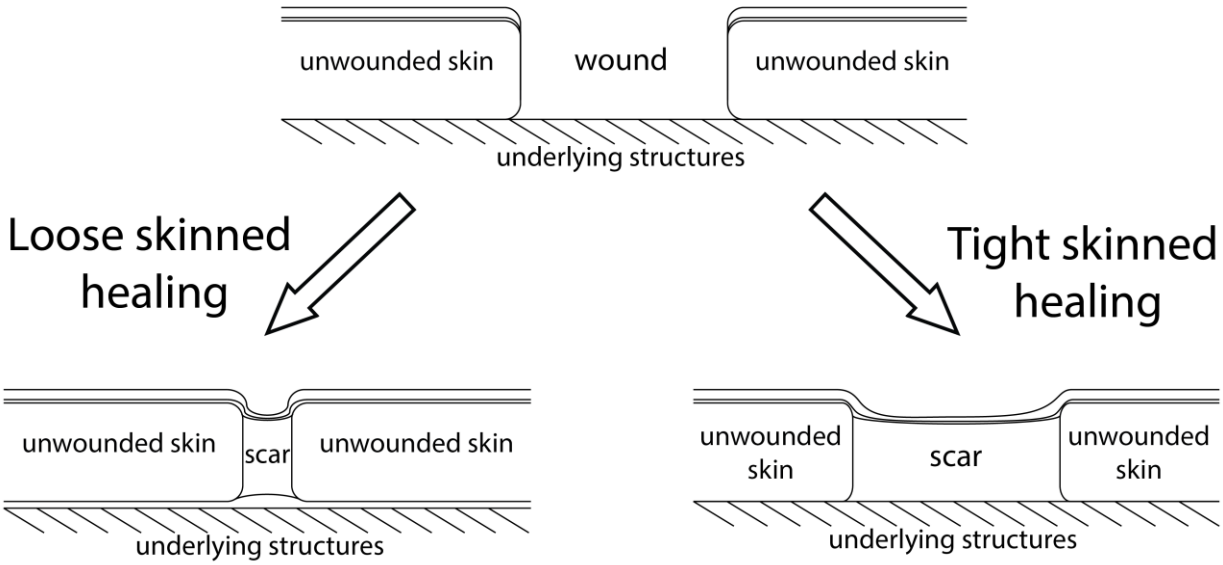

Figure 13: Result of the differing mechanical environments of “loose skin” vs “tight skin” on the healing excisional wound.

So far studies in humans have identified two key αCT1 treatment effects in cutaneous scars. Treated scars at one month from the phase I clinical trials, while exhibiting no difference in surface scar appearance, have been found to have a more unwounded-skin like collagen matrix histologically (discussed in detail in Chapter 2). Treated scars from the phase II clinical trials also exhibited no difference in surface scar appearance at month 1 post-wounding, but by month 9 treated scars showed a 47% improvement over control in skin surface appearance (Figure 2)[120]. Histological samples at month 9 were not available, nor were there biopsies taken in the intervening months. Given these two data points so separated in time, we can currently only hypothesize that the improved collagen matrix at month 1 later leads to a collagen matrix at month 9 that is so much more similar to unwounded skin that it has visible effects on the surface appearance, or that has facilitated the regrowth of other normal skin markers not normally present in the scar.

In order to further characterize the development of the observed changes in the healing of wounded skin after treatment with αCT1, and determine if it directly or indirectly contributed to improved scar appearance at 9 months, resolution of the phenomena at multiple, progressive time points over the scar remodeling process is required. As a first step towards this goal, we attempted to identify an animal model that could closely replicate the results seen in the human at ~1 month.

3.3 Splint Type & Size Determination

3.3.1 Rationale

Utilizing the cell culture data from Figure 4 and the results of the analysis of the phase I clinical trial biopsies (discussed in detail in Chapter 2), a collaboration with the Holmes laboratory created a computer simulation of αCT1-treated fibroblasts repairing a wound space (Figure 14). Importantly, the simulation identified the potential importance of mechanical strain within the system. Without mechanical strain, both αCT1 and control simulations resulted in a highly disorganized collagen matrix. However, with mechanical strain parallel to the surface, as what is naturally present in human skin, the control simulation resulted in a collagen structure highly oriented parallel to the surface, while the αCT1 simulation remained mostly unchanged, resulting in a highly disorganized collagen structure. This made it clear to us that any experimental model of αCT1 treated scars must account for mechanical strain within the healing wound.

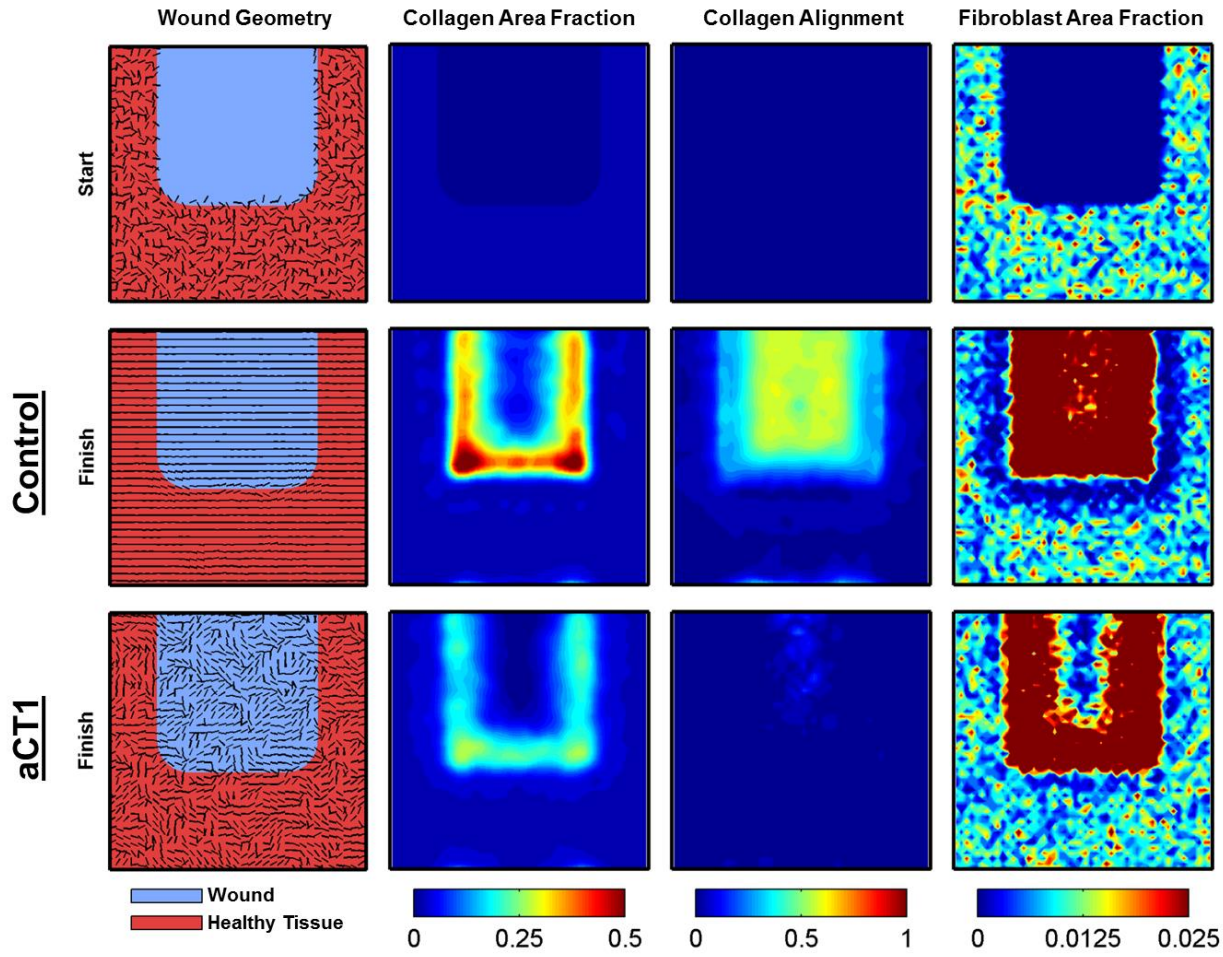

Figure 14: Initial computational model of fibroblast invasion into the wound space and the resulting collagen matrices with or without αCT1 treatment at Day 29.

Unfortunately, as discussed previously, mechanical strain within the healing wound is completely different in tight-skinned vs loose-skinned animals (Figure 13). Loose-skinned animals heal primarily by wound contraction due to the relatively unrestricted movement of the skin, while tight-skinned animals heal primarily by the formation of granulation tissue due to the skin's relative immobility. However, a wound splint model is a well-known method of forcing excisional wounds in loose-skinned animals to heal more similarly to tight-skinned animals[154]. The wound splint prevents wound contraction by suturing ring-shaped silicone splints around an excisional wound, inducing a mechanical environment in the wound similar to that naturally present in tight skin. Several methods of wound splinting have been presented in the literature[154–156], so it was decided an initial analysis would be carried out in order to determine the optimal method of wound splinting for further study.

3.3.2 Methods

Hair Removal

Male Sprague-Dawley rats[157] (n=15), chosen for their ready availability and adequately thick skin, were first allowed to acclimatize to the facility. Four days before surgery, animals were anesthetized and their dorsal fur removed by #7 size clippers followed by Nad's®[158] and VEET®[159] brand cold wax strips. The Nad's®[158] strips were used first, to remove the majority of the fur, and then the VEET®[159] strips (which are more adhesive) were used to remove the remaining strands. The waxed dorsal area was then treated with olive oil to remove excess wax and moisturize the skin to alleviate any irritation. The waxed area was then gently covered with a piece of gauze and a commercial rat jacket[160] along with a custom-made wound covering that attaches to the jacket was secured on the rat. The jacket and covering was left on the rat until the time of surgery in order to acclimate them to the clothing.

Commercial Rat Jacket & Custom-made Wound Covering

The jacket and covering (Figure 15) was used, with 100% success, to prevent rats from removing the study devices through chewing and/or scratching (Figure 16). Most rats adjusted within 1-2 days to wearing the garments. Although the rats tended to chew and scratch at the edges and straps of the garments, garments could hold up to continuous wear on a single rat without adjustment or replacement for one week or more. The largest issue with the garments actually came not from the custom-made wound covering the majority of their body, but from the commercially available jacket that held it in place. Several rats managed to get their lower incisors caught in the threads of the jacket and were unable to free themselves, tearing their gums in the process and sometimes bleeding quite heavily before they could be freed with human assistance.

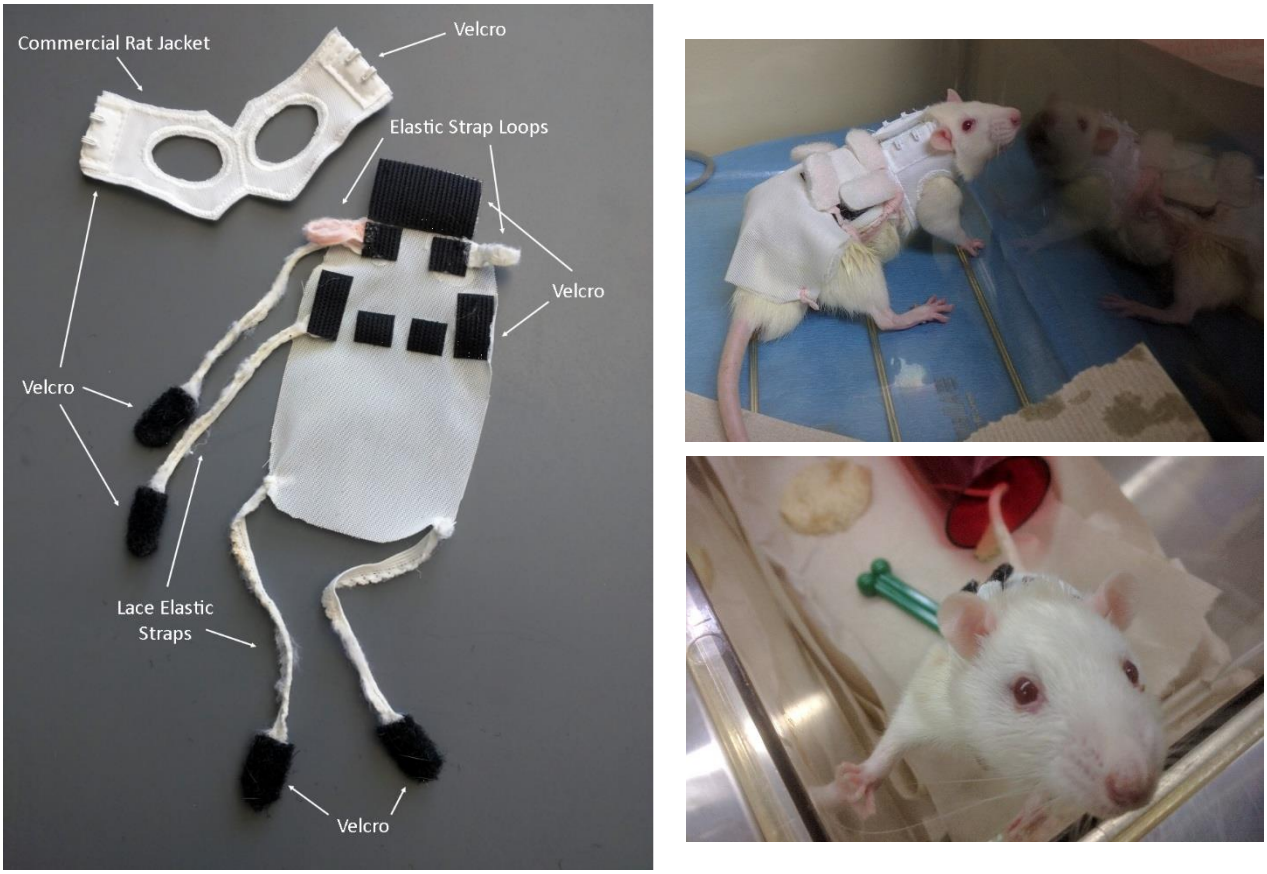

Figure 15: Photographs of the Lomir® rat jacket[160] and custom wound covering by itself (left) and in position on a rat (right).

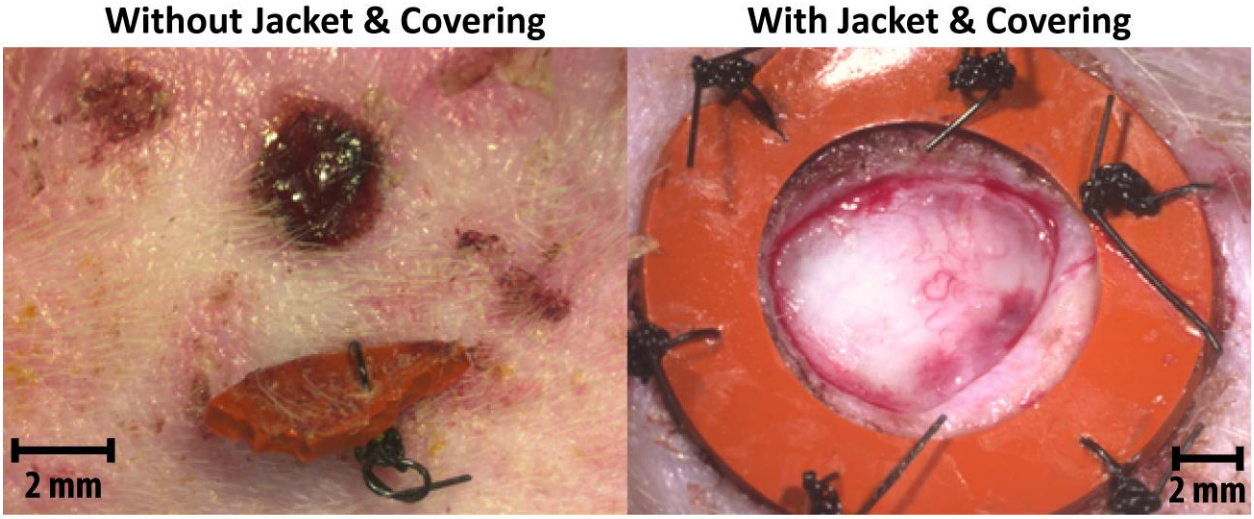

Figure 16: Two days after wounding and surgical application of the splint with the jacket and covering applied (right) and without the jacket and covering used (left).

Surgery

On the day of surgery, animals were anesthetized via isoflurane[161], placed on a prewarmed isothermal pad, and then given 0.2 mg/kg buprenorphine SR™-LAB[162] for analgesia. Animals were given 5 mL warm saline to maintain temperature and hydration throughout the surgery. The dorsal region was prepped via 6 alternating scrubs of betadine[163] and 70% alcohol, applied in a circular motion beginning at the center of the surgical area and working towards the periphery. The surgical site was then covered with a sterile disposable surgical drape. Plane of anesthesia was monitored throughout the surgery through toe pinch, respiration, and any reaction to surgical procedure. Six full thickness excisional wounds, 3 on either side of the spine, were created in the dorsal surface. Sterile splints with inside diameter approximating the wound edge were then first secured with Krazy® glue[164] around the wound, and subsequently sutured through the full thickness of the skin with at least 6 interrupted 4-0 nylon sutures with a P-13 needle size[165]. After surgery, animals were transferred to the draped platform of the Nikon SMZ1500 dissection microscope[166] for imaging. The wound area was then covered with sterile gauze and secured with the jacket[160] and covering. Animals were then returned to the recovery cage and placed on a heating pad for monitoring while they roused from anesthesia. Animals were monitored carefully until sufficiently ambulatory and aware of their surroundings, and then left overnight on the heating pad for a more comfortable initial recovery period.

Imaging

Animals were anesthetized and their wounds imaged using the same dissection scope[166] at set time points after surgery. After imaging, soiled or sufficiently damaged jackets and/or coverings were exchanged for fresh garments and replaced on the animal.

Splint Type and Size Analysis

Fifteen rats underwent surgery to place various thickness silicone[167–171] and metal[172] splints around 5 mm and 8 mm diameter wounds made using 5 or 8 mm Miltex® disposable biopsy punches[173,174]. Silicon splints were cut using a Mayhew Pro 66000 hollow punch set[175]. Thirteen rats made it to the study end point of 2 weeks (one rat was euthanized at 3 days and another managed to remove the majority of its splints within the first few days). Fourteen days after surgery, animals were euthanized. Wounds were imaged as before[166]. Splints were then removed and the scar tissue and surrounding unwounded skin biopsied. Biopsied scar tissue was washed, placed in 4% paraformaldehyde for 24 hours, sectioned across the approximate midline of the scar, and then embedded in paraffin. Paraffin sections were stained with picrosirius red and H&E.

Potential Diffusion of Gel-Suspended Treatment Across the Dorsal Midline

Since the goal of this study was to recapitulate the human clinical trials in an animal model, and we planned on employing within-patient controls by applying a treatment and placebo gels to paired wounds on either side of the spine, it was important to ensure that the treatments would not cross the dorsal midline and result in treatments being applied to both wounds. Immediately after splinting surgery was completed, prior to placing the jacket and wound covering, fluorescent beads were mixed into a 0.4% natrosol[176] gel and applied to the 3 wounds on the left side of the dorsum. A 0.4% natrosol[176] gel with no additives was added to the 3 right side wounds. The wounds were imaged under brightfield on the Nikon SMZ1500[166] as per usual, but then also imaged under fluorescence to highlight the fluorescent beads. The wounds were then covered as per usual and the animal allowed to recover. Twenty-four hours post-surgery, the wounds were imaged again to identify any potential diffusion of the treatment gel across the midline.

3.3.3 Results

Splint Type, Thickness, & Wound Size

Using the images obtained from the dissection scope[166], the size and shape of the scar at 14 days was judged compared to the initial wound (Table 3). Silicone splints[167–171] were more effective than metal washers[172] at maintaining scar surface area and shape. Sectioned tissue samples were used to judge the profile of the wound through the thickness of the skin. The larger initial wounds, at 8 mm, maintained a significant amount of scar tissue throughout the depth of the tissue while the 5 mm wounds were more likely to have significant wound contraction and thus minimal or no scar tissue at the base of the dermis. No significant differences were noted between the resultant scars from the different reasonable thicknesses of silicone[167–169,171] splints.

Table 3: Images of the various types of splints applied to 5 & 8 mm diameter wounds on the dorsum of the Sprague-Dawley rat. The 2.4 mm thickness silicone was only applied to 5 mm diameter wounds, and the metal lock washer was only applied to 8 mm diameter wounds. All splints were autoclaved prior to application.

	0.5 mm silicone	0.8 mm silicone	1.6 mm silicone	2.4 mm silicone	0.6 mm silicone (alternate)	Metal lock washer
5 mm wound						
8 mm wound			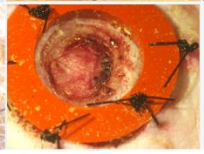	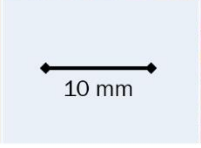		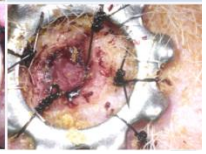

No Dorsal Midline Diffusion of Potential Treatment Gel

After 24 hours, fluorescence was still contained to the left side wounds, with no fluorescence identified in the right side wounds treated with fluorescent-negative gel (Figure 17).

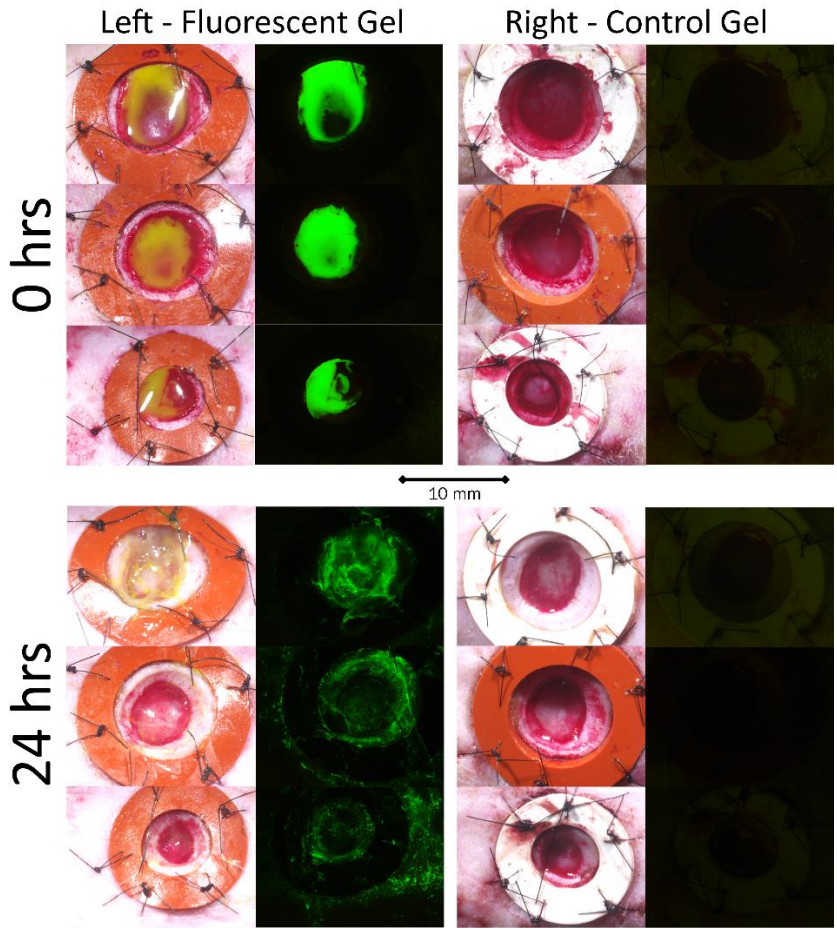

Figure 17: Fluorescent gel[176] evaluation of potential treatment diffusion across the midline (n=1 rat). While the gel was clearly smeared and somewhat absorbed over the course of 24 hours, there was no transfer of fluorescence between opposite sides of the dorsum. This indicates that αCT1 treatment gel can be applied to one side of the dorsum and we can expect the gel to remain locally, dispersing at the intended wound site over the 24 hours of peptide release.

3.3.4 Conclusions

Given the 0.5-0.6 mm[168,171] splints were more liable to tear during surgical application, and the thicker silicone[169,170] splints dulled sutures faster, the 0.8 mm thickness silicone[167] splints secured around 8 mm diameter wounds[174] were chosen for use in all subsequent animal tests.

In a test involving fluorescent gel, no transfer of fluorescence across the dorsal midline was identified after 24 hours, suggesting that treatment gel applied to one side of the dorsum will remain locally. This allows us to use paired within-patient treatment-control comparison wounds on either side of the dorsum in the small animal models, since the release of αCT1 from the gel occurs over 24 hours.

3.4 Sprague-Dawley Rat

3.4.1 Rationale

The scar tissue samples from the phase I clinical trials (detailed in Chapter 2) provided a single timepoint at 29 days that suggested that αCT1 prompted a change in collagen organization deep within the dermis. In order to further characterize the development of this change in the healing of wounded skin, and determine if it directly or indirectly contributed to improved scar appearance at 9 months, resolution of the phenomena at multiple, progressive time points over the scar remodeling process is required. Since it is not possible to repeat the experiment at multiple long-term time points in humans due to IRB-related reasons, it is necessary to develop an animal model that sufficiently replicates the human results. To keep costs to a minimum, and due to the limitations of available facilities, the animal model also needed to be a small laboratory animal that could be kept in conventional facilities.

A murine model was excluded immediately, as their skin is not thick enough for a depth-wise analysis. Skin samples from several rat strains, including the OM rat, were examined to determine whether skin thickness varied significantly by strain (data not shown). No significant differences were found between strains, but overall it was determined that the thickest skin came from the dorsum of young adult (6 week+) male rats. Sprague-Dawley rats were therefore chosen as the first animal model for examination due to their ready availability and general hardiness.

3.4.2 Methods

Male Sprague-Dawley rats[157] (n=10) were used in this study for the reasons discussed above. Hair removal, surgery, imaging, and application of rat jackets[160] was performed as described in Section 3.3.2. Due to the results listed in Section 3.3.3, wounds were created with an 8 mm Miltex® disposable biopsy punch[174] and then secured with an 0.8 mm thickness silicone[167] splint of inner diameter 9.5 mm and outer diameter 16 mm[175] using Krazy® glue[164] and 6-8 sutures[165].

αCT1 & Placebo Natrosol Gels

Replicating the methods used in Cohort 3 of the phase I clinical trial of αCT1, 100 µM of αCT1 was suspended in a 0.4% natrosol gel[176] solution for the active treatment. A 0.4% natrosol gel[176] solution was used as control to replicate the placebo vehicle control used in the trial. Each animal received approximately 75 µL of gel per wound immediately after surgery and again 24 hours later; 3 wounds on one side of the spine would receive the active treatment, while the 3 wounds on the other side of the

spine would receive control gel (Figure 18). Which side of the spine received which treatment was randomized between animals.

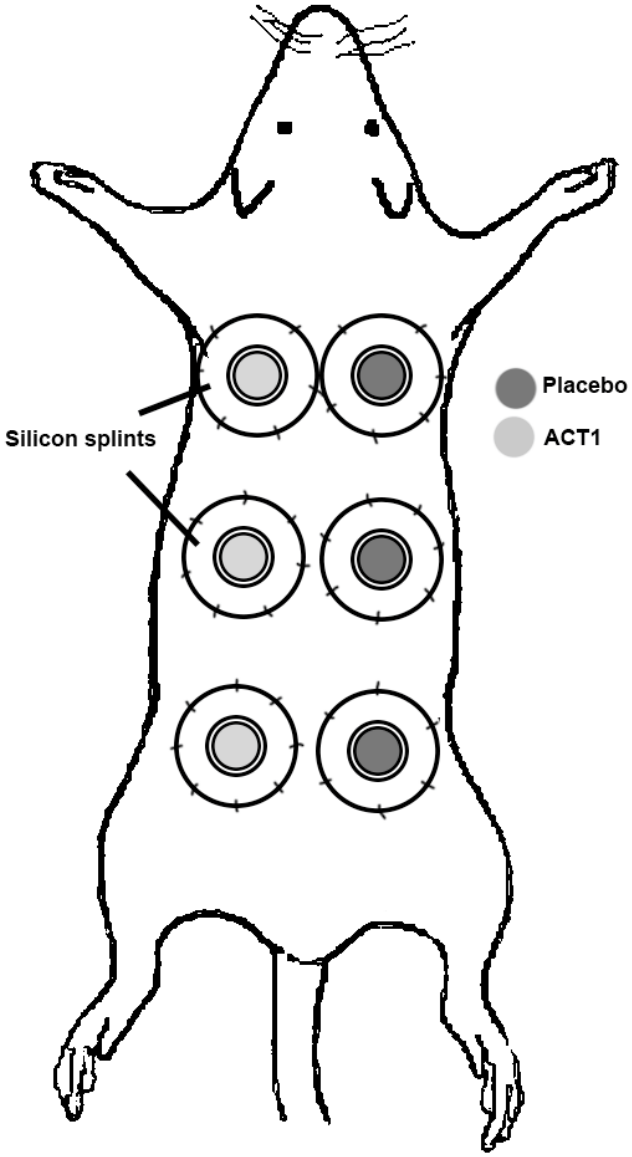

Figure 18: Diagram showing animal study testing scheme. One randomized side of the spine received αCT1 treatment suspended in natrosol gel, while the other side received a placebo gel containing no peptide.

Biopsies

One paired set of active and control wounds was taken from each animal at 2, 4, and 6 weeks using a 10 mm biopsy punch[177]. Animals received 4 mg/kg carprofen[178] or 0.2 mg/kg buprenorphine SR™-LAB[162] for analgesia prior to the biopsies at 2 and 4 weeks. Animals were euthanized at the 6 week timepoint.

Biopsied scar tissue was washed, placed in 4% paraformaldehyde for 24 hours, sectioned across the approximate midline of the scar, and then embedded in paraffin.

Analysis

Paraffin sections were stained with picrosirius red and then imaged at multiple linear polarization angles using an automated system (briefly discussed in Section 2.4.2). The multiple angle images were then compiled and analyzed for collagen structure using a MATLAB program as per Section 2.4.2. Statistics were analyzed in JMP® Pro[135,179] as discussed in Section 2.3.4.

3.4.3 Results

The basic patterns of collagen alignment and density observed in the phase I patient controls were recapitulated in the rat model (Figure 19, Figure 20). Treatment scars had consistently higher collagen fiber density and collagen fiber disorientation (circular variance), but treatment effect was much less apparent than what was observed in the human. Interestingly, it appears that while the mechanical effects of the splint are effective throughout the tissue at Week 2, by Week 4 the convergence of the density and circular variance approximately 1 mm into the tissue suggests that imposition of mechanical strain by the splint may vary by depth.

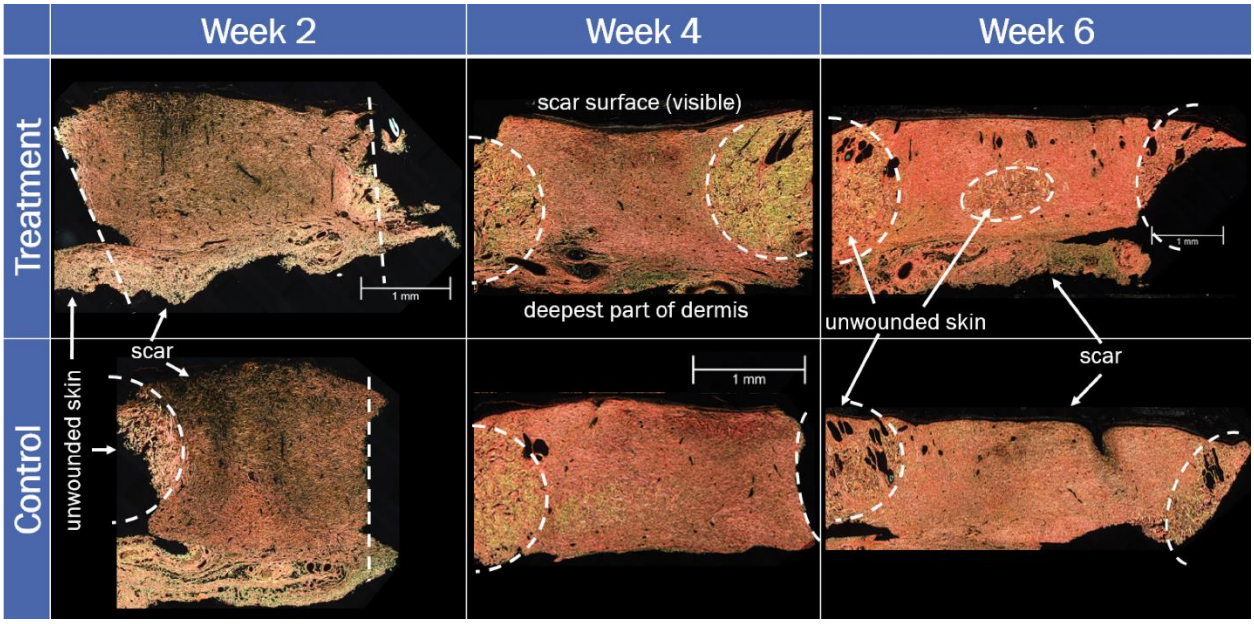

Figure 19: Sprague-Dawley rat treatment & control scar biopsy sections from all 3 timepoints collected. The scar samples were sectioned through the middle of the tissue and are oriented with the skin surface towards the top of the page and the basal part of the tissue towards the bottom. Dotted lines mark the edges of the scar boundary. Note the infiltration of unwounded skin into the middle of the week 6 treatment biopsy. In several cases, the scar could not even be identified in the week 6 biopsies because the infiltration of normal tissue had progressed so severely, leading to a loss of statistical power.

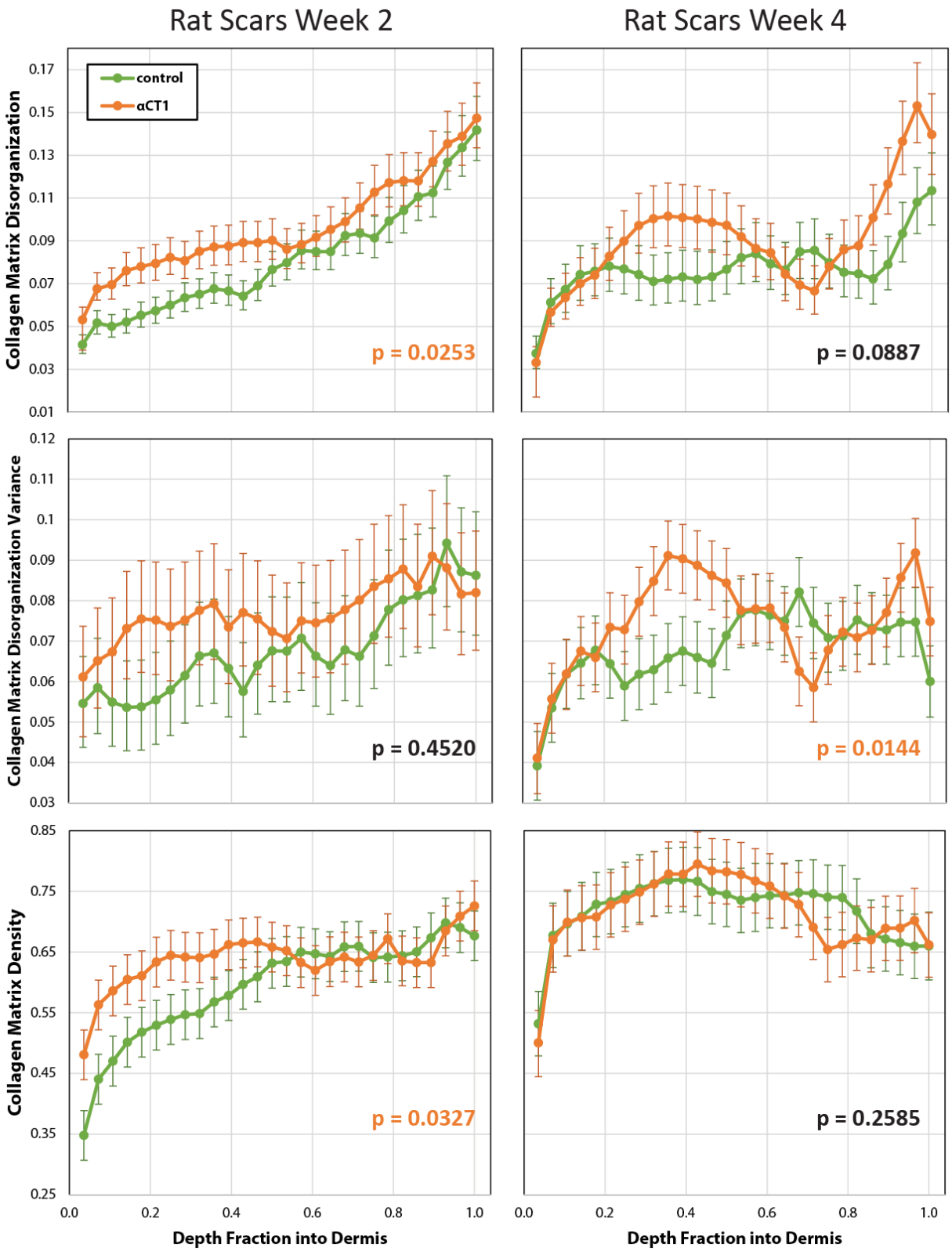

Figure 20: Results of the statistical analysis of Week 2 & Week 4 splinted rat wounds. Error bars ±SE.

Week 6 results could not be analyzed due to splint loosening and difficulty identifying the scar tissue within biopsied samples, significantly reducing the number of samples available for analysis (Figure 19). The samples that could be accurately identified had such a large range of variance that normalization of the data for remotely accurate statistical analysis was not possible. As such, the week 6 rat samples were excluded from further analysis.

3.4.4 Discussion

Treatment of rat scars with αCT1 results in a general increase in collagen disorganization, disorganization variance, and a notably transient increase in collagen density, much the same as the human. However, the most major limitation was the inability to progress to week 6 with enough statistical power for adequate analysis. While the rat jackets prevented the rats from removing the splints by biting or rubbing, they also prevented casual observance of the splints, making it more difficult to determine when splints needed to be resutured to maintain the mechanical force on the scar. Suture expulsion by the skin over time, and hair regrowth pushing up at the splints from underneath, contributed to loosening the splints and causing the loss of enough week 6 scars to significantly reduce the statistical power of the analysis.

If rats were to be employed as a long term model of human scar remodeling and maturation, more animals would need to be used for the longer time points to retain statistical power, and more manpower to adequately monitor those splints on a daily basis would be necessary. A major problem however would still be the hair regrowth underneath the splints and around the edges of the wounds, since waxing or epilating would likely damage the skin and be an additional variable to account for, shaving would be a very temporary solution, plucking would be extremely time-consuming, and all four methods would require complete removal and replacement of the wound splints. A more ideal model would be hairless, avoiding this problem altogether, which leads to the other animal tested in this aim, the IAF Hairless guinea pig.

3.5 IAF Hairless Guinea Pig

3.5.1 Rationale

While the Sprague-Dawley rat is cheap and readily available, it does have some significant drawbacks as a model of human skin. Like most animals, it has a significant amount of fur, meaning that a much larger percentage of the skin is occupied by highly developed hair follicles which can alter skin mechanics and wound healing. Rat strains without visible fur have been developed for laboratory use, however these strains fall into one of two categories: they are either immunocompromised (nude rats) or they have

normal hair follicles, but the shaft of the hair is unable to pierce the surface of the skin (hairless rats), making them poor models for replicating human wound healing and scar formation.

Originating from a random mutation among albino Hartley guinea pigs at Montreal's Institute Armand Frappier (IAF), the IAF Hairless guinea pig[180] (Figure 21) is unique among rodents in that its hairlessness is caused by a reduction in fully developed hair follicles, the same reason that humans are mostly hairless. This results in most of the skin being lightly peppered with smaller hair follicles, with certain limited areas retaining normal hair growth. IAF Hairless are immunocompetent, and as guinea pigs they also have the added advantage of slightly thicker skin than rats. A previous study determined that IAF Hairless guinea pigs had an epidermal thickness similar to that of humans, with a more developed dermal vasculature also more similar to that of humans than normal haired guinea pigs, making their skin the most similar to that of humans among rodents[181]. Thus, the IAF Hairless guinea pig is worth investigating as a potential model for recapitulating the results of the phase I clinical trials.

Figure 21: IAF Hairless guinea pig pictured prior to surgery (left) and several days post-surgery (right). Note that while they display increased hair thickness and density around the snout and feet, the majority of the animal appears to be "hairless", covered only with sparse, fine hair very similar to that of a human.

3.5.2 Methods

Housing

Male IAF Hairless guinea pigs weighing approximately 300 g (n=15) were obtained from Charles River Laboratories[180]. Animals were kept in group housing of up to 6 animals prior to surgery. After surgery, animals were placed in cages separated in half by plastic dividers with holes drilled into it in order to maintain social ties while preventing splint removal by mutual grooming. The front of the cages were also set face to face, so that each animal had a maximum of 3 other animals it could see and interact with.

Anesthesia

All animals were fasted for at least 6 hours prior to initiation of anesthesia. Their mouths were also rinsed prior to anesthesia with tap water applied through a large syringe and their cheeks swabbed with sterile cotton buds in order to prevent aspiration pneumonia.

Hair Removal

Although the animals are mostly hairless, much of their dorsum is covered with thin, fine hairs like that found on a human. Two days prior to surgery, animals were anesthetized and the fine hair removed from their dorsum using Nad's® waxing strips[158], in order to create the best surface for surgically applying the splints. Olive oil was used to remove excess wax and relieve any skin irritation incurred. Animals were allowed to recover from anesthesia on a heating pad and then returned to group housing.

Guinea Pig Jackets

Guinea pig jackets acquired from Lomir®[182] were modified by removing some of the portion that covered the stomach, reducing guinea pig discomfort and accumulation of bedding and feces on the jacket. Guinea pig jackets were only placed on guinea pigs as necessary, once they had started disturbing the splints. The majority of guinea pigs in this study did not disturb their splints and thus did not require the jackets.

Surgery & Biopsies

Surgery on the guinea pigs was performed the same as the rats as described in Section 3.3.2 with several exceptions. Guinea pigs were given 0.3 mg/kg buprenorphine SR™-LAB[162] after induction of anesthesia prior to surgery for analgesia, and 4 mg/kg carprofen[178] prior to survival biopsies at weeks 2 &4. Guinea pigs were given maximum 1-3 mL warm sterile saline prior to surgery due to difficulties injecting large volumes of liquids SQ. Heart rate, temperature, and respiration rate were monitored carefully throughout surgery.

3.5.3 Results & Discussion

Two guinea pigs were lost within 24 hours of initial surgery due to complications (stomach torsion from necessary fasting & aspiration pneumonia from anesthesia). All samples from the 13 surviving guinea pigs were included in the analysis.

In the guinea pig scars, week 4 and 6 samples showed significant treatment effects for collagen disorganization and disorganization variance (Figure 22, Figure 23). Collagen density in week 4 was significantly higher in treatment samples ($p=0.0481$), and in keeping with the postulated theory that αCT1 only temporarily increases collagen scar density, the effect declined to a trend by week 6 ($p=0.0645$).

When initially imaging the samples, it was qualitatively observed that there was often very little difference in density between the week 2 and week 4 samples (Figure 22). While the week 4 samples are overall slightly denser than the week 2, the difference between week 4 control samples and the week 2 samples is only about 10%. This is a stark difference from the rat samples, which were much denser at week 2 than the guinea pig at week 4. Also, interestingly, there was no significance found in the guinea pig samples at week 2 – there was a slight trend for a depth-dependent effect on disorganization variance, but that was it. When observed overall in Figure 23 the week 2 treatment samples averaged higher disorganization and disorganization variance, but controlling for patient eliminated any significance.

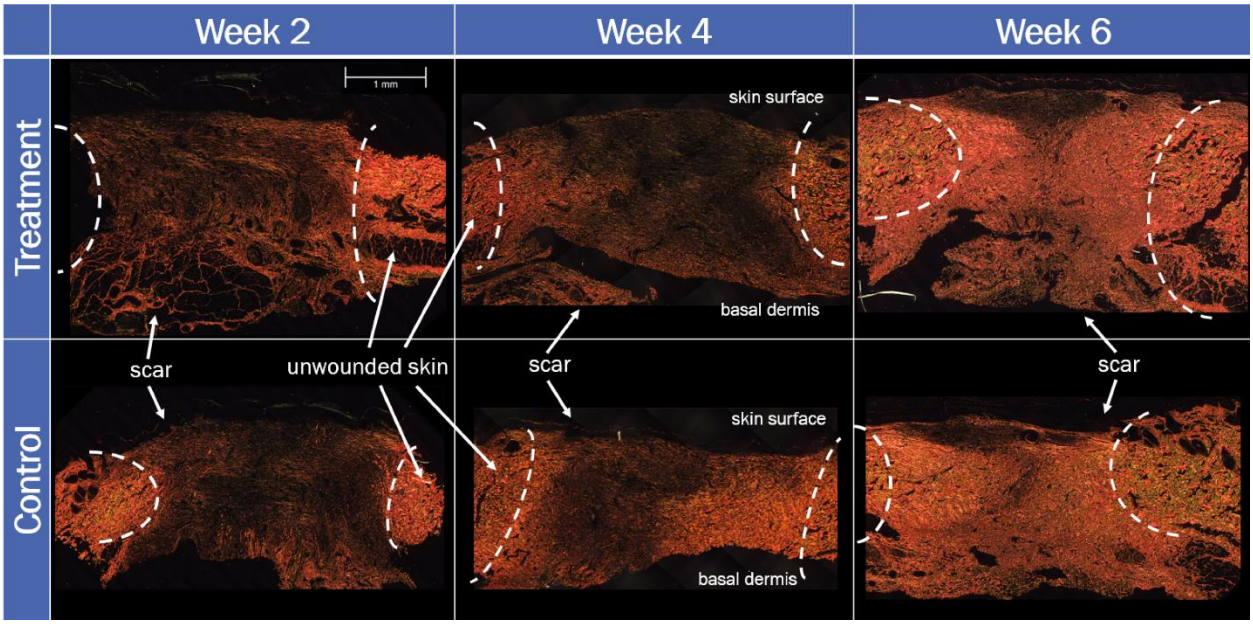

Figure 22: IAF Hairless guinea pig scar biopsy sections from all 3 timepoints. The edges of the scar are indicated by the dotted lines. The skin surface is oriented upwards with the basal part of the dermis at the bottom of the image. Unlike the rat scars, the week 6 scars in the guinea pig were all successfully maintained and collected.

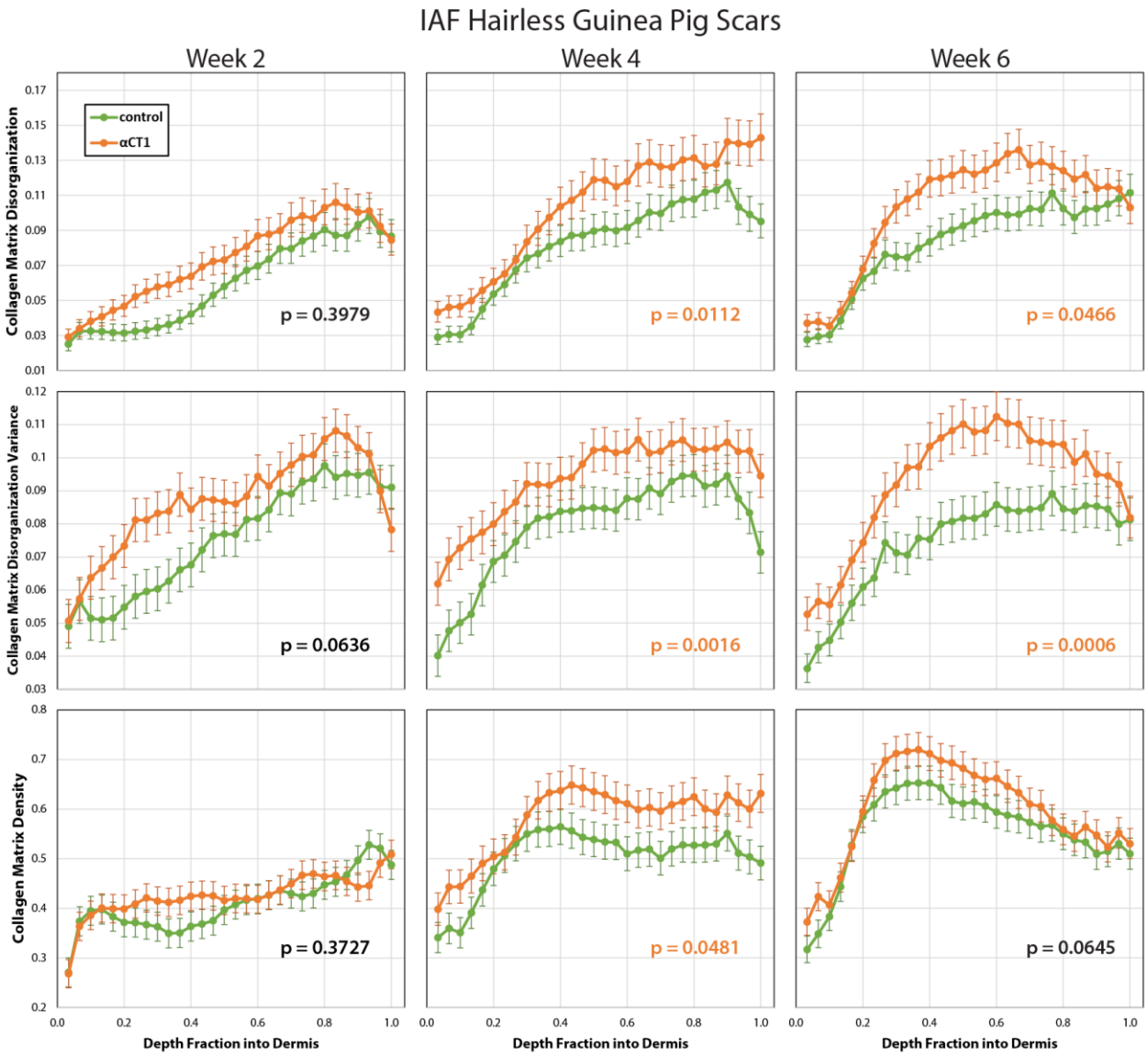

Figure 23: Guinea pig scar collagen disorganization, disorganization variance, and density across weeks. Error bars ±SE.

The results when comparing the IAF Hairless guinea pig to the human clinical trials are, overall, positive. When looking at the values and trend of the lines across depth for disorganization, disorganization variance, and density, the guinea pig at weeks 4 and 6 strongly resemble that of the human. The week 2 results however present at odds with all other observed time points, but it is clear that all the scars are at the very beginning stages of construction. Is it possible that if we had human samples at week 2, they would also have no observable treatment effect at this early stage of healing? The initial goal of the analysis of the clinical trial samples had been to identify a structural "link" between the treatment applied in the first two days and the surface level effect that only starts appearing by month 3. But what these

guinea pig results seem to be implying is that there's still a step missing in between the treatment and the collagen matrix differences that have been observed.

3.5.4 Conclusions

An improvement over the standard Sprague-Dawley rat model, the IAF Hairless guinea pig appears to more closely replicate the human cutaneous wound healing condition, with sparse hair follicles, thicker skin, similar dermal collagen matrices in the healing wound, and similar peptide treatment effects on the collagen matrix. Beyond the human-like qualities, the guinea pigs are also much easier to work with than rats. They are far less irritable and physically flexible, with most of them not disturbing the splints at all for the entire six week duration of the study. The sparseness of hair follicles was also beneficial in maintaining the wound splints for a duration as long as six weeks.

The only clear drawbacks to the IAF Hairless guinea pig model are the problems associated with anesthesia and the extra level of IACUC involvement required for guinea pigs vs rats. Despite these, the IAF Hairless guinea pig presented here represents a novel small animal wound healing model more similar to human clinical biopsies than existing models. Closer replication of the human wound healing condition in preclinical small animal trials has the potential for wide reaching effects, including reducing the cost and time associated with bringing scar reduction and wound healing drugs to market.

Chapter 4

4 Aim 3: Collagen1(α2) GFP-topaz Primary Murine Dermal Fibroblast Cultures

4.1 Abstract

Introduction: Previous research has identified αCT1 treatment effects on *in vivo* human, rat, and guinea pig skin biopsies, as well as *in vitro* dose-dependent effects on NIH 3T3 fibroblast directional persistence and movement speed. *In silico* models have predicted the increased collagen matrix disorganization *in vivo* is largely a result of fibroblast behavior *in vitro*, and has an important mechanical cue component.

Objective: To experimentally confirm the computational model, directly linking the αCT1-mediated changes in fibroblast behavior *in vitro* with the persistently more disorganized and transiently more dense collagen matrices seen in healing skin wounds *in vivo*.

Methods: Primary dermal fibroblasts were isolated from 3-4 week old collagen 1(α2) GFP-topaz (Col1tpz) mice and sorted by FACS for GFPtpz expression after culturing in ascorbic acid negative media for several days to retain collagen within the cell membrane. Aligned collagen coated wells were seeded with ~1000 cells/cm^2 and allowed to adhere for 24 hrs. After 24 hrs, macromolecular crowded (MMC) media to encourage extracellular matrix formation and peptide treatment was added to each well. Cells were treated over the course of 7 days with either no peptide (CTRL), 100 µM reverse peptide (REV), 100 µM antennapedia-only peptide (ANT), or 10, 50, or 100 µM αCT1. On the final day cells were fixed and stained for collagen 1, paxillin, and nuclei for quantification of final cell and matrix values.

Results: No significant difference in final cell numbers was observed. Treatment with αCT1 was found to significantly increase procollagen synthesis by primary dermal fibroblasts, as measured by both final pixel density fraction (PF) and fluorescence intensity (FI) of antibody-stained collagen, and that effect was dose dependent. The effect of 100 µM αCT1 treatment was significant regardless of which control treatment was used as statistical control (ANT [p_{PF}=0.0002 & p_{FI}=0.0003], CTRL [p_{PF}=0.0020 & p_{FI}=0.0224], REV [p_{PF}=0.0044 & p_{FI}=0.0129]). When ANT was used as statistical control, the 50 µM dose of αCT1 was also significantly more collagen dense by both measures (p_{PF}=0.0441 & p_{FI}=0.0275).

Conclusion: Treatment with the therapeutic dose of 100 µM αCT1 caused primary dermal fibroblasts to increase procollagen synthesis by 1.5-2x over control in MMC-enhanced *in vitro* culture conditions, and this effect was likely dose dependent. Previous research had found slightly increased collagen matrix density in αCT1-treated scars at 2-6 weeks, and it had previously been suspected that this was due to earlier fibroblast infiltration. This study, however, reveals a new role for αCT1 in directly increasing the extracellular matrix protein output of individual cells.

4.2 Introduction

After the initial wound healing stages of hemostasis and inflammation have tapered off, dermal fibroblasts begin to invade the wound space. They degrade the fibrin clot formed by platelets and begin to lay down the first components of a new extracellular matrix. As the days and weeks progress, more fibroblasts invade and, using that preliminary matrix as a guide, strengthen and expand the new extracellular matrix[14–17].

Histological examination of the collagen structure present in *in vivo* studies in the human, rat, and guinea pig (detailed in the previous two chapters of this dissertation) have found distinct differences in scars treated with αCT1 early in the wound healing process. Specifically, the collagen structure present in αCT1 treated wounds was significantly more disorganized, with high regional variability in disorganization, with a transient increase in fiber density that did not persist to longer time points. These results, and the early post-wounding timeline of αCT1 treatment, suggest that the long-term improvements in scar appearance results seen in the phase II clinical trials[120] may have been structurally programmed into the early scar matrix by the action of dermal fibroblasts affected by αCT1 treatment in the first few days after injury.

Previously, NIH 3T3 fibroblasts treated with αCT1 in 2D *in vitro* cell culture demonstrated increased speed and more rapid and pronounced changes in orientation. 3T3 fibroblasts were treated with varying levels of αCT1, no peptide, 100 µM reverse peptide or 100 µM antennapedia sequence only. A significant, dose-dependent effect on cell speed and directional persistence was observed in αCT1-treated cultures. At the therapeutic dose of αCT1, 100 µM, fibroblasts were 3 times more likely to change migration direction than control cells (Figure 4). Computational simulations incorporating the data from these experiments has also indicated that the specific behavior induced by αCT1 is consistent with an improved collagen structure more similar to unwounded skin within the scar, and may be due to a reduction in the fibroblast's tendency to follow mechanical cues (Figure 14).

4.3 Objective

This study will specifically examine the effects of αCT1 treatment on dermal fibroblasts and the resultant extracellular matrix using primary murine dermal fibroblasts expressing a fluorescent collagen protein *in vitro* in a 2D environment designed to mimic aligned mechanical cues. The goal is to directly link αCT1 treatment, changes in fibroblast behavior, and changes in the extracellular collagen matrix in the healing wound.

4.4 Methods

Collagen 1(α2) GFP-topaz (Col1tpz) Mice

A genetically modified mouse strain expressing GFP-topaz on the α2 strand of collagen 1 on a C57-BL6 background was obtained as a kind gift from Dr Sarah Dallas (University of Kansas City Missouri Medical Center). Highly expressing individuals could be easily identified by use of a 515nm LED light source and 550nm filter glasses[183,184] , due to the high collagen 1 content of skin. Highly expressing individuals selected as breeders were either outbred to WT C57-BL6[185] or interbred.

Primary Dermal Fibroblast Isolation

Highly expressing Col1tpz mice 21-26 days of age were selected by skin fluorescence as described above. Animals were humanely euthanized via CO2 exposure followed by internal decapitation. Mice were pinned and the dorsum and belly were shaved. Starting from the genital region, the skin was cut along the midline up to the chin and along the axes of the limbs. The mouse was then flipped over and the entire skin up to the facial area was collected in a single piece. Ears were also collected and frozen for record-keeping purposes. The skin was rinsed twice in EtOH, twice in sterile phosphate buffered saline (PBS), and once in sterile harvest media (10 mM glucose, 3mM KCl, 130 mM NaCl, 1 mM disodium phosphate, 30 mM HEPES @ pH 7.4). The skin was then floated epidermis-side down in working harvest solution containing 0.25-0.5% trypsin[186] on a rocker at 4°C for 20-26 hrs. The skin was then rinsed again in harvest solution and the epidermis removed from the dermis via light mechanical action. The epidermis was discarded. The dermis was rinsed in Hank's buffered saline solution (HBSS) and then diced using a sterile scalpel and/or razor blade.

The diced dermis was transferred to a sterile 125 mL Erlenmeyer flask and 6 mL of HBSS containing ~275 u/mL collagenase type I[187] was added. The flask was placed in a water bath at 37°C on a rotator for 45 min, then the flask contents were agitated using a wide bore pipet and another 6 mL of collagenase type I in HBSS was added before the Erlenmeyer flask was returned to the water bath. After 30 minutes, the flask was again removed, the liquid contents were strained through a 70-100 µm nylon cell strainer[188,189] into a 50 mL conical tube, and another 6 mL of collagenase type I[187] in HBSS was added before the flask was again returned to the water bath. This last step was repeated 3-5 times until the diced dermis was entirely digested. The contents of the conical tube(s) were spun down at 1000 rpm for 6 minutes, then the cells were resuspended in DMEM[190] containing 10% calf serum (CS)[191], 50 µg/mL ascorbic acid[192], and antibiotics (2.5 µg/mL amphotericin B[193], 50 U/mL penicillin streptomycin[194], & 50 µg/mL gentamicin[195]) for plating. Antibiotic concentration was slowly scaled down over the course of 1-1.5 weeks, removing the

gentamicin[195] entirely and reducing the amphotericin B[193] and penicillin streptomycin[194] to 1/4th their original concentrations (0.625 µg/mL & 12.5 U/mL, respectively).

Fluorescence Activated Cell Sorting (FACS) of Highly Expressing Col1tpz Cells

After isolation, cells were cultured for 0.5-2 weeks until a sufficient quantity for cell sorting was achieved. To simplify the cell sorting procedure, ascorbic acid was removed from the media 1-2 days prior to fluorescence activated cell sorting (FACS). Removing ascorbic acid from the media prevents cells from properly externalizing collagen proteins, causing the buildup of fluorescent procollagen proteins within the cell membrane. In the case of our Col1tpz fibroblasts, cells that highly express collagen will have a large buildup of fluorescent GFP-topaz within the cell, allowing them to be easily identified by FACS without having to use any external markers or dyes. Thus, for the purposes of this experiment, a fibroblast is any cell isolated from the dermis that highly expresses our Col1tpz protein.

Cells were sorted solely for high GFP-topaz expression using a Sony SH800S Cell Sorter[196] with a linear sorting gate set from ~10^4 to 10^6 compensated EYFP detection, collecting ~20-25% of the highest expressing cells in each culture. Sample pressure was set on the lower side (4-5 in the system's arbitrary settings) to prevent shearing of the cells during sorting. Cells were then replated and allowed to regrow back to confluency prior to peptide experiments.

Aligned Collagen Coating of ibidi Polymer Coverslip Plates

In 3D collagen gel cultures, force can be directly applied to the gel to provide mechanical cues to the cells. However, in 2D cultures directly exerting a plate-wide mechanical force is rather difficult. Instead, contact guidance cues were substituted using a pre-aligned collagen matrix coated onto the plates before passaging cells. Due to the GFPtpz fluorescence to be imaged, regular cell culture plastic plates could not be used for the experiment since it interferes with transmission in those light wavelengths. Normally glass would be used instead – however, due to the hydrophilic nature of glass it is extremely difficult to get collagen to adhere, let alone align on a glass-bottomed plate (Figure 24b), and solutions often involve complicated procedures and expensive equipment. Instead, ibidi µ-Slide 2 well chambered polymer coverslip plates[197] were used. Instead of traditional glass, the bottom of these plates is a thin polymer with optical properties ideal for fluorescent and most other kinds of imaging that collagen readily adheres to and aligns on (Figure 24c).

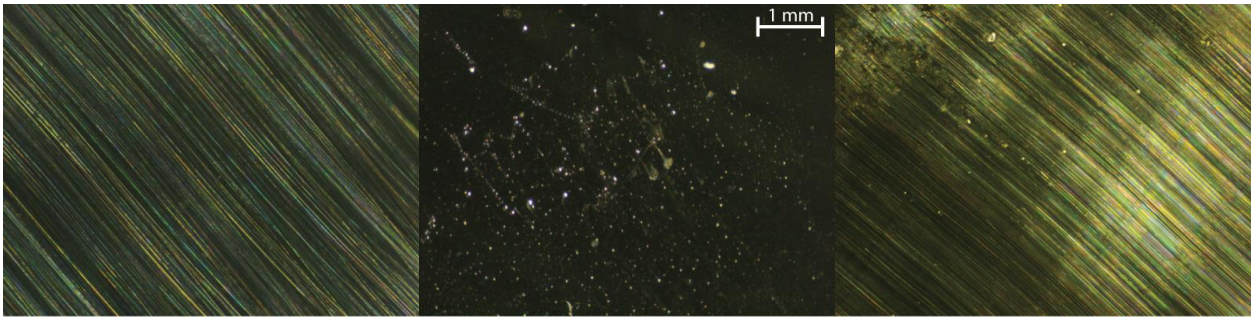

Figure 24: Attempted aligned collagen coating on various surfaces.

To coat the ibidi polymer coverslip plates with an aligned collagen matrix, 12 µL of 8.24mg/mL rat tail collagen[198] was diluted to 100µg/mL in 1 mL of 0.02M acetic acid. For each well, 100 µL was deposited on one side and then a cell scraper[199] was used to firmly drag the collagen solution across the length of the well. The plate was elevated on the side that the solution was initially deposited on, and then allowed to incubate for 1 hr. After 1 hr, the wells were gently washed twice with sterile PBS and then allowed to air dry overnight. The process was repeated the next day to create a double coating, which is less likely to lift off of the plate during culturing. Coated plates were stored at 4°C as necessary. One hour prior to plating cells, the plates were removed from 4°C and incubated with 2% w/v bovine serum albumin[200] in PBS to saturate free binding sites. After 1 hour, plates were rinsed 3x with sterile PBS and the cells were plated in standard cell culture media.

Macromolecular Crowding of Cell Culture Media for Enhanced Matrix Deposition

One significant challenge in the *in vitro* creation of extracellular matrix is that procollagen, the uncleaved precursor of collagen, is water-soluble[201]. Procollagen must first be excreted by the cell before it can be processed and arranged into collagen fibers, which means that a large amount of potential matrix is lost to drifting away in the cell culture media[201]. The solution to this is macromolecular crowding (MMC), filling the soluble space of the media with a large number of inert molecules nonharmful to the cells. MMC has previously been found to increase matrix deposition *in vitro* by an order of magnitude[201–204].

To create MMC imaging media, 37.5 mg/mL Ficoll 70[205] and 25 mg/mL Ficoll 400[206] were added to supplemented[207,208] phenol red-negative DMEM[209], 10% CS[191], and 50 µg/mL ascorbic acid[192] media[203]. Antibiotics were added as needed at low concentrations, 1/4th-1/10th their original concentrations (0.63-0.25 µg/mL amphotericin B[193], 12.5-5 U/mL penicillin streptomycin[194]).

αCT1 Peptide Dermal Fibroblast Experiments

FACS-sorted Col1tpz dermal fibroblasts were plated at ~1000 cells/cm^2 (~5000 cells/well) on aligned collagen coated[198] ibidi polymer coverslip 2 well plates[197] in standard cell culture media[190–194] and allowed to adhere for 24 hrs. The media was then siphoned off at 24 hrs and replaced with MMC media (detailed above). One of the treatments listed below in Table 4 was also applied to each well at this time[108,210,211]. Peptide treatment was reapplied every 24 hrs. Cells were washed with calcium-positive DPBS and the MMC media replaced every 48 hours. Cells were live-imaged on a Perkin Elmer spinning disk microscope system[212–229]. Each well was cultured for 7 days from the time of addition of MMC media and was then fixed with 4% paraformaldehyde and stained for nuclei[230], mouse collagen 1[231,232], and paxillin[233,234]. Antibody-stained cells were imaged at 63x on a Leica SP8 system[235].

Table 4: Peptides used in the *in vitro* experiments.

Label	Peptide	Concentration	Condition
CTRL	none	-	control
ACT1_10	αCT1[108]	10 µM	treatment
ACT1_50	αCT1[108]	50 µM	treatment
ACT1_100	αCT1[108]	100 µM	treatment
REV	Reverse αCT1[211]	100 µM	control
ANT	Antennapedia only[210]	100 µM	control

Density Metrics

Density of collagen and pro-collagen deposited on the surface of the culture plate was measured in the final collagen matrix SP8 fluorescence images by two slightly different metrics. The first was image fluorescence intensity. Indexed collagen 1 (568nm excitation)[231,232] fluorescence TIF images were summed for total pixel value (0-255) and then divided by the total number of pixels in the image. Where multiple images of the same well were taken, a per-well image set mean was calculated to be used in the statistical analysis.

The second metric was thresholded pixel fraction. The same indexed TIF images were converted to binary images with pixel values 0-4 set to zero and values 5-225 set to one. Pixel sum was calculated per image and divided by the total number of pixels to determine a thresholded pixel fraction per image. Again, where multiple images of the same well were taken, a per-well mean was calculated for statistical use.

Statistics

Both density metrics were analyzed in parallel in JMP® Pro 14[179] using a one-way ANOVA. After ensuring that the data fulfilled parametric requirements, Dunnett's method for control comparison was used for each control condition.

4.5 Results

Three wells containing REV, ACT1_10, and ACT1_50 peptide treatment were lost due to contamination (REV, ACT1_10, & ACT1_50 [n=3]). All other wells were included in the analysis (ACT1_100 & CTRL [n=5], ANT [n=4]).

At a concentration of 100 µM, αCT1 caused a significantly greater deposition of collagen 1 on the cell culture dish as measured by both fluorescence intensity and thresholded pixel fraction (Figure 25), regardless of which control treatment was held as control (antennapedia-only peptide, no peptide control, or reverse peptide). When antennapedia-only peptide was used as the statistical control, the 50 µM dose of αCT1 was also found to have significantly higher collagen 1 deposition.

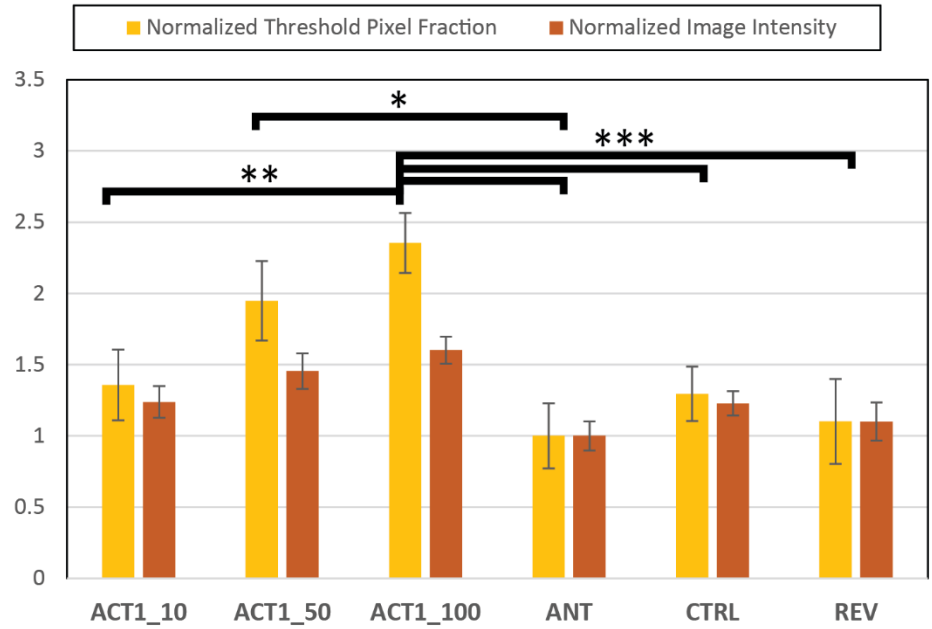

Figure 25: Treatment differences in collagen density measured by either the fraction of pixels in the image above a threshold intensity, or the weighted fluorescent intensity of the image ± SE. Numbers were normalized to the antennapedia-only control (ANT) for visual purposes only. At the 100 µM dose, αCT1 was significantly more collagen dense as measured by both values and when compared to all 3 controls as well as the small 10 µM dose. When using the antennapedia-only peptide as control, the 50 µM dose was also significant for both measurements.

Table 5: Results of statistical analysis of the two density measures, shown by which control treatment was held as statistical control. Regardless of measurement or control peptide used, αCT1 was significant at a 100 µM dose.

Treatment	P-values When Used as Control					
	Threshold Pixel Fraction			Image Intensity		
	ANT	CTRL	REV	ANT	CTRL	REV
ACT1_10	0.7453	0.9999	0.9247	0.3914	1.0000	0.8603
ACT1_50	0.0441	0.2255	0.1366	0.0275	0.4727	0.1801
ACT1_100	0.0002	0.0020	0.0044	0.0003	0.0224	0.0129
ANT	-	0.8107	0.9983	-	0.3288	0.9461
CTRL	0.7847	-	0.9616	0.3072	-	0.8476
REV	0.9990	0.9804	-	0.9650	0.9074	-

4.6 Conclusions

Addition of αCT1 at the therapeutic dosage of 100 µM in an MMC-media enhanced fibroblast culture resulted in approximately 1.5-2x greater collagen deposition when compared to all controls. This effect was also likely dose dependent based on the approximately linear increase in mean density across treatments, although the 50 µM dose was only significant when compared to one of the control peptides and the 10 µM dose was barely distinguishable from all three controls.

Enhanced collagen deposition after treatment with αCT1 correlates strongly with our results in the human and rat scars that found increased collagen density at 4 and 2 weeks respectively. Our hypothesis, that this *in vitro* data further supports, was that αCT1 application transiently increased initial collagen deposition rate but did not affect the final collagen density of the scar. Previously we had relied on earlier data that found αCT1 decreased the length of the inflammatory phase and increased cell speed to explain this, suggesting that αCT1 was causing more fibroblasts to infiltrate the wound space earlier, leading to the increase in collagen density through sheer numbers. But with similar plating densities and no observed difference in final cell counts, these *in vitro* results would suggest that a significant part of that increase is actually due to αCT1 directly increasing the synthesis of procollagen 1 within dermal fibroblasts. Further study is needed to see if it enhances the production of other extracellular matrix proteins or affects the final composition of the extracellular matrix both *in vitro* and *in vivo*.

Chapter 5

5 Discussion

5.1 Summary

Scars are emblematic of the villain in popular culture: Scar from Lion King, Darth Vader, Scarface, just to name a few. We don't just dislike cutaneous scars, as a culture we judge them and the characters that bear them negatively[236]. Painful, stiff, or highly contracted scars can also severely negatively impact our daily lives beyond the judgement of others. The reasons for desired improvement of cutaneous scars may vary from the vain to the strictly practical, and everything in between, but αCT1 could treat scars regardless of reason. This dissertation has presented several studies exploring the mechanism of action of scar improvement with the Cx43 CT mimetic peptide αCT1, and presented a novel small animal model exhibiting greater fidelity with the human healing scar than established models.

In Chapter 2, we identified key structural collagen differences in αCT1 treated phase I human clinical trial biopsies at 1 month post-wounding. In human subjects, the peptide appears to spur the creation of a collagen matrix that is more similar to the high disorganization present in unwounded skin, particularly at the basal layers of the tissue. It also appears to slightly increase the density of the collagen matrix, although whether this increased density is transient (as other data suggests) cannot be definitively determined with only a single time point. This structural improvement in collagen matrix at one month, as the only histological treatment effect identified, is suspected to be a key driver of the scar surface improvements seen at much later timepoints in the phase II trials[120].

In Chapter 3, we explored wound-splinted rodent models of wound healing and established that the IAF Hairless guinea pig can be used to create a novel, more human-like environment for testing scar reduction drugs in a small animal model. The IAF Hairless guinea pig has been remarkably underutilized by wound healing scientists for the 41 years since its spontaneous emergence in a colony of albino Hartley guinea pigs. To our knowledge, this is the first time an IAF Hairless guinea pig has been employed in excisional wounding studies or as a splinted wound model. To date, the animal has primarily been employed in dermatologic studies of cutaneous drug and allergen absorption[237–239]. This study did not just establish that the IAF Hairless guinea pig is a better model for replicating human αCT1 treatment results, it found the model has an overall improved capacity to replicate the human wound healing environment compared to rat or mouse. Use of this hairless guinea pig model could increase the efficiency of evaluation of other wound healing therapeutics in the pre-clinical/clinical pipeline.

In Chapter 4, we delved into *in vitro* work with primary dermal fibroblasts isolated from a relatively novel transgenic mouse line stably expressing Col1(α2)GFPtpz, allowing analysis of the matrix constructed under MMC-enhanced *in vitro* conditions and revealing new data that αCT1 causes individual fibroblasts to increase procollagen synthesis and output. Transiently increased collagen density in the *in vivo* biopsies had previously been identified, but was suspected to be caused purely by increased early fibroblast infiltration due to earlier experiments that found αCT1 both decreased the length of the inflammatory phase[98] and increased fibroblast movement speed (Figure 4). These experiments provide new data that αCT1 increases the extracellular matrix building capacity of individual cells without requiring the recruitment of new fibroblasts to the wound space.

5.2 Challenges, Limitations, and Future Work

5.2.1 Phase I Clinical Trial Biopsies

This study into the collagen structural changes associated with αCT1 treatment originally emerged from a histological examination of H&E stained sections from the same trial that found no treatment differences in commonly used histological markers of improved scar healing, such as the presence of rete pegs or hair follicles (Figure 3). The only difference the histological evaluation found was a small potential difference in collagen density in the deepest part of the tissue using a very rough eosin deconvolution method. The goal of the study was to definitively determine, with histological staining for collagen specifically, whether there was a structural collagen difference between treatment samples.

Limitations: Single Polarization Angle Analysis

The initial analysis, carried out on only a single linearly polarized angle image, is the standard method of collagen bundle analysis widely used among biologists (Figure 26). However, while this is acceptable for circularly polarized systems, which will allow imaging of the entire array of collagen fibers regardless of angle, the birefringence of collagen under linearly polarized light is highly dependent upon the fiber angle and corresponding angle of the polarization condenser and analyzer[133,134,148,240] (Figure 27). Since the single analysis work was performed, the data was included in Section 2.3. But it should be understood as an initial analysis to provide context for the subsequent more involved and more accurate multiple angle analysis described in full in Section 2.4.

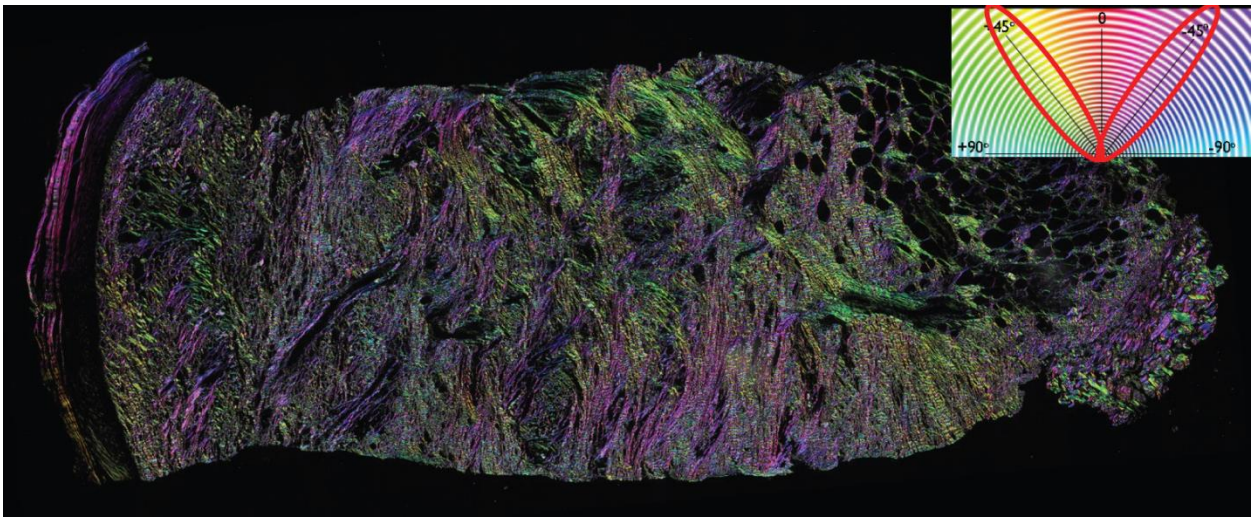

Figure 26: Example of a biopsy from Cohort 3 of the clinical trial imaged at a single polarization angle colorized dependent on collagen fiber angle, with color wheel key inset. Notice that the vast majority of the fiber angles lie within the highlighted narrow angle ranges perpendicular to one another.

Red/Green ratio analysis is another analysis traditionally performed with birefringent collagen samples that doesn't quite hold up to advanced scrutiny. Traditionally, the more red-orange fibers in picrosirius red-stained collagen samples have understood to be type I collagen, while the more green fibers have been understood to be type III. However, studies have shown that the color of the birefringent collagen fibers under polarized light only represent the orientation, thickness, and packing density of the fibers, and have no direct correlation with specific collagen subtypes[133,134]. The red/green ratio values and p values for the samples were included in this dissertation since they were examined and analyzed, but they remain an interesting side note and not something upon which to base solid conclusions or hypotheses upon.

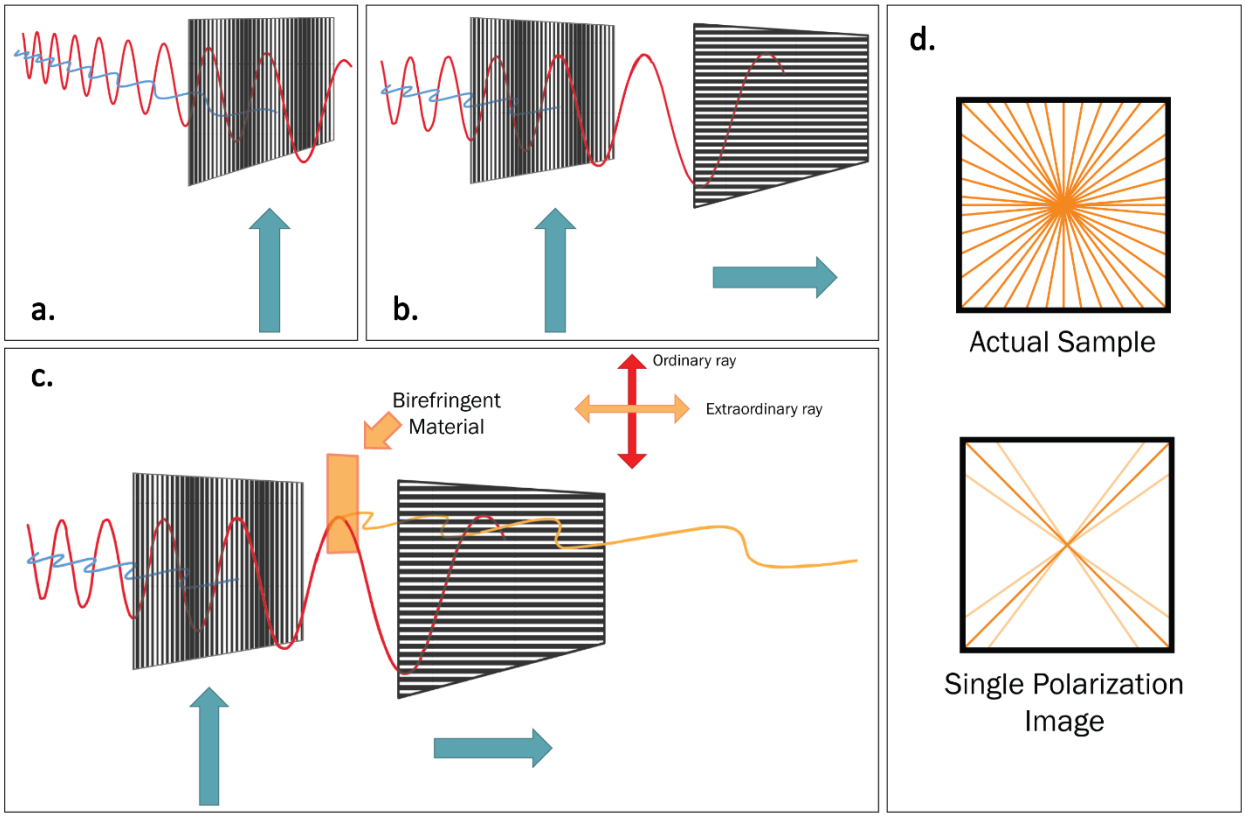

Figure 27: Overview of how polarization and polarized imaging of birefringent collagen samples work. (a) Understanding light as made up of two component wavelengths, a single polarized lens (condenser) will block one wavelength component. (b) Placing a second polarized lens (analyzer) after the condenser and orienting it perpendicularly to the first will block the second component wavelength, completely blocking the passage of light. (c) A birefringent material, when placed in between the condenser and analyzer, is one that generates what is known as an "extraordinary ray" that can then pass through the analyzer and be seen alone in an otherwise dark field. (d) Collagen birefringence depends on the relationship between fiber angle and the angle of the condenser and analyzer. Taking the top image as an example of how an entire collagen sample actually appears, the bottom image is what would be seen when imaging at a single polarization angle.

Challenges: Multiple Polarization Angle Analysis

While it is very easy to list the results of the multiple angle analysis in short, neat tables and graphs, it should be understood that the multiple angle analysis was an enormous undertaking, involving the planning, construction, and programming of a user-operated semi-automated microscope addition, the need to image all the samples at six different angles which increased the imaging time and data storage required by six times, and the programming, verification, and operation of a semi-automated MATLAB[123] program to assemble the images together and then break them down into their constituent quantitative data variables.

Future Work

A major drawback of the study, since red/green ratio analysis is not reliable, is the inability to determine the specific collagen subtypes present in the scar. Unwounded skin and scar tissue are primarily constructed of a mixture of type I and type III collagen, but the ratios of the mixture vary wildly between the two and in the healing scar over time. Studies in fetal skin[241,242] and the Acomys regenerative skin mouse[243] have linked an increase in early type III collagen to type I collagen deposition ratio in the wound space to improved scar outcomes. To discover whether the collagen changes prompted by αCT1 are not just structural, but also differ at the protein level, the most reliable method of analysis is antibody staining specific for collagen subtypes. Antibody stains of the samples could also be used to explore potential differences in alpha smooth muscle actin (αSMA), MMP, TGFβ, and the various other protein markers linked to altering final scar outcomes[243–247].

5.2.2 Long-term Wound Splinted Small Animal Model of Healing

The main challenges associated with the animal models came from the rats, which is one more reason why I recommend the IAF Hairless guinea pigs as a front-line researcher personally dealing with the study animals. Following is a brief list of complications encountered with the rat model and the solutions employed to subvert the rats' repeated challenges to the successful completion of the study.

Rat: Analgesia-related Challenges

High recommended post-surgical opiate doses: The majority of surgical studies that IACUC approves involve significantly more extreme surgery than our proposed cutaneous excisional wounds and sutured wound splints. In that context, requiring a buprenorphine dose of 1.2 mg/kg is perfectly reasonable. However, for our particular protocol, the postoperative pain felt by the rats appeared to not be too severe. In fact, the first rat operated upon and given the IACUC-mandated 1.2 mg/kg buprenorphine SR was so negatively affected by the high opiate dose, not the pain, that it had to be euthanized for humane reasons. The dose was lowered significantly, to 0.2 mg/kg, which gave the rats adequate pain relief without the concern of overdose harm.

Pica: While the lowered opiate dose appeared to affect the rats less severely, leaving them more active and alert post-surgery with minimal pain response, for a large subset of the study population the dose was still large enough to induce pica, compelling them to consume a notable number of the alpha chips that make up typical rodent bedding in our animal facilities. For those animals, "pica-proof" bedding sheets were tried – and failed in spectacular fashion, as animals mentally affected by the opiate managed

to rip it up and consume it anyway. The only solution found was to give the rats only a small amount of alpha chip bedding material in cages immediately post-surgery until 2-3 days and the opiate-related pica had passed.

Severe allergic reaction after secondary buprenorphine SR dose: Animals in the 6-week studies had to undergo multiple survival surgeries: first to create the excisional wounds and adhere the splints, then twice at 2 and 4 weeks wounds were biopsied before the final end point at week 6. Originally, we saw no reason not to use buprenorphine SR for all 3 surgeries, even though the first was the one likely to cause the most pain. The first rat to receive a second dose of buprenorphine had a severe allergic reaction, with obvious alarming edema present. While there is not any information out there specifically on buprenorphine SR allergy upon multiple exposures, we decided in consultation with the IACUC vets that to be safe, subsequent rats would receive 4 mg/kg carprofen at the weeks 2 & 4 biopsies, which was tolerated well.

Rat: Wound Splint-related Challenges

Consumption of the study devices: When the post-surgical dorsum was left uncovered, rats recovered from surgery immediately began to pick at the wound splints with their teeth, claws, and the edges of any enrichment devices provided to them. Multiple commercial solutions were tried and failed to prevent splint removal by the rats. Eventually, the solution of a commercial rat jacket combined with a handmade cloth wound covering, with soft elastic straps securing it firmly across the belly, was successful at preventing rats from interfering with the study devices for the entire 6 week duration of the study (Figure 16). However, the jackets and covering did introduce limitations of their own. With the wound splints covered, it was difficult to tell when the splints needed to be resutured due to splint deadherence and suture expulsion. Animals needed to be lightly anesthetized twice weekly to remove soiled jackets and coverings, resuture splints if needed, and replace the jackets and coverings with freshly laundered ones.

De-adherence of the study devices: While the jackets were effective at preventing the animals from removing the wound splints themselves, they could not prevent factors like the natural expulsion of sutures from the skin over time. Additionally, at approximately weeks 3-4, hair that had been removed by waxing several days prior to wounding began to reemerge from the unwounded dermis in force, including directly underneath where the splints were placed. The hair regrowth pushed up on the splints, facilitating suture expulsion, and in more than a few cases completely obscuring the location of the original wound biopsy by week 6.

Guinea Pig: Minor Challenges

While the rat presented the primary challenges in Aim 2, the guinea pig was not without its minor complications. Two of the study animals did not make it to the study end point due to death from anesthesia-related complications within the first 24 hours post-surgery.

Anesthesia-related aspiration pneumonia: Guinea pigs, unlike rats, have small cheek pockets where food can be stored/trapped in the mouth. Before anesthesia, to prevent aspiration pneumonia from occurring while sedated, their mouths must be gently rinsed out with water and cotton buds. After their first experience with this short procedure, most of the guinea pigs were highly uncooperative with subsequent mouth rinsing. However, this uncooperative behavior was confined solely to this single procedure and not general handling or other examination when the animals were handled gently and bribed with treats such as dried fruits.

Stomach torsion from fasting prior to anesthesia: Guinea pigs, like most herbivores, are grazers that require constant access to food. However, to prevent aspiration pneumonia, animals must be removed from food at least several hours prior to sedation. In rare cases, even a short imposed fast can cause gastric torsion, a condition that is almost always quickly fatal in guinea pigs, with very little chance of clinical rescue[248].

Future Work

The entire goal of creating a viable small animal model of human-like wound healing that replicated the αCT1 treatment results found in Aim 1 was to then utilize it in a long-term study, tracking the histological changes in the scar from the time of injury to the long-term scar surface appearance results seen in the phase II clinical trials. Originally this had been planned to be completed as part of this dissertation work. However, IACUC delays and early complications, combined with the lengthy biopsy analysis, made it clear that any plans for a long term study will have to be the subject of future work.

5.2.3 Collagen1(α2) GFP-topaz Primary Murine Dermal Fibroblast Cultures

Many challenges were encountered in the process of completing Aim 3 since the experiments relied on a multitude of factors, from the breeding of transgenic mice and availability of highly-expressing individuals in the right age range for isolation, to survival of large primary cells post-FACS and an unideal live-imaging humidity/CO2 setup.

Selection of a Highly Expressing Col1(α2)tpz Fibroblast Population with FACS

Initially, experiments were attempted with fibroblasts directly after isolation and culturing. However, it quickly became apparent that the expression of Col1(α2)tpz was highly variable across the isolated population, even within the same animal. FACS sorting of the fibroblasts was necessary to select for the portion of the fibroblast population that expressed enough Col1(α2)tpz to be reliably imaged in culture. Luckily, the FACS sorting process was made easier by the nature of the tagged protein. Scurvy is a condition most people are aware of and typically associate with pre-18th century sailors, who had no access to fresh fruit or vegetables on long sea voyages. Scurvy is characterized by the breakdown and persistent bleeding of oral mucosa and the reopening of old, previously healed wounds. In modern times, scurvy is understood to be a slow breakdown of the extracellular matrix caused by lack of vitamin C, also known as ascorbic acid. Without ascorbic acid, fibroblasts are unable to traffic procollagen out of the endoplasmic reticulum, preventing the normal trafficking of procollagen out of the cell and subsequent extracellular collagen fibril formation[249]. Therefore, identification of cells that highly express Col1(α2)tpz was easily accomplished by removing ascorbic acid from the cell culture media 1-2 days before FACS, causing a buildup of fluorescence within the cell that could be selected for.

Limitations in 2D

It is well understood that the behavior of fibroblasts, and most cell types in general, can vary greatly between 2D and 3D cultures[85,250–252]. One limitation of 2D culture is the inherent stiffness of the substrate – fibroblasts exposed to stiff substrates show decreased expression of $\alpha_2\beta_1$ integrin, reducing fibroblast migration[84,86]. Additionally, while 3D collagen gels can be exposed to varying strains and mechanical forces, which have been shown to direct fibroblast migration[15,80,84,85,253], it is much more difficult to directly exert force on a traditional 2D culture. However, 3D cultures are significantly more difficult to image than traditional 2D cultures, especially at high magnifications like 63x or 100x that require objectives with very thin focal planes. Various 2D approximations of 3D cultures have been established in the literature, like collagen-coated membranes[80] and thin gels, but these all present their own problems, especially when desiring to live-image the cells instead of capturing a single end time point. In this study, a prealigned collagen I matrix on a 2D plate was used to create contact guidance as a rough substitute for mechanical force for biasing fibroblast migration in a particular direction[77,79,254–256]. Future experiments on these fibroblasts should likely focus on the transition to 3D and the direct application of skin-like mechanical strain to confirm these initial experiments.

Future Work

A large quantity of data was collected during the *in vitro* experiments, but time constraints and technological limitations have prevented analysis of many of the variables collected from being included in this dissertation. An overview of these variables and expected outcomes is provided below.

Final collagen matrix orientation: An initial exploratory pre-study experiment (n=1) using no peptide treatment was performed prior to the full set of peptide experiments to see if the prealigned collagen substrate would bias the fibroblasts to align synthesized Col1(α2)tpz fluorescent collagen fibrils in the same direction. Analysis of this initial exploratory experiment showed the final assembled collagen matrix was highly oriented in the original direction of the prealigned substrate (Figure 28). If our hypothesis that αCT1 causes a loss of mechanical signaling in fibroblasts, causing defects in their migration directionality and thereby disorganizing synthesized collagen matrix alignment holds true, then we should expect to find no bias for the 0° direction and a greater deviation in mean angle in αCT1 treated cultures.

There are several methods of angle analysis, including MatFiber[141] and directionality functions included in FIJI[125]. Unfortunately, with some very thin barely fluorescent matrices, some very densely packed matrices, and a large amount of unpolymerizered pro-collagen globules present in many of the collagen matrix images, none of the programs tested thus far have been able to process all of the images with acceptable accuracy. Time-consuming manual alignment determination will likely have to be performed for the subset of images that cannot be processed automatically.

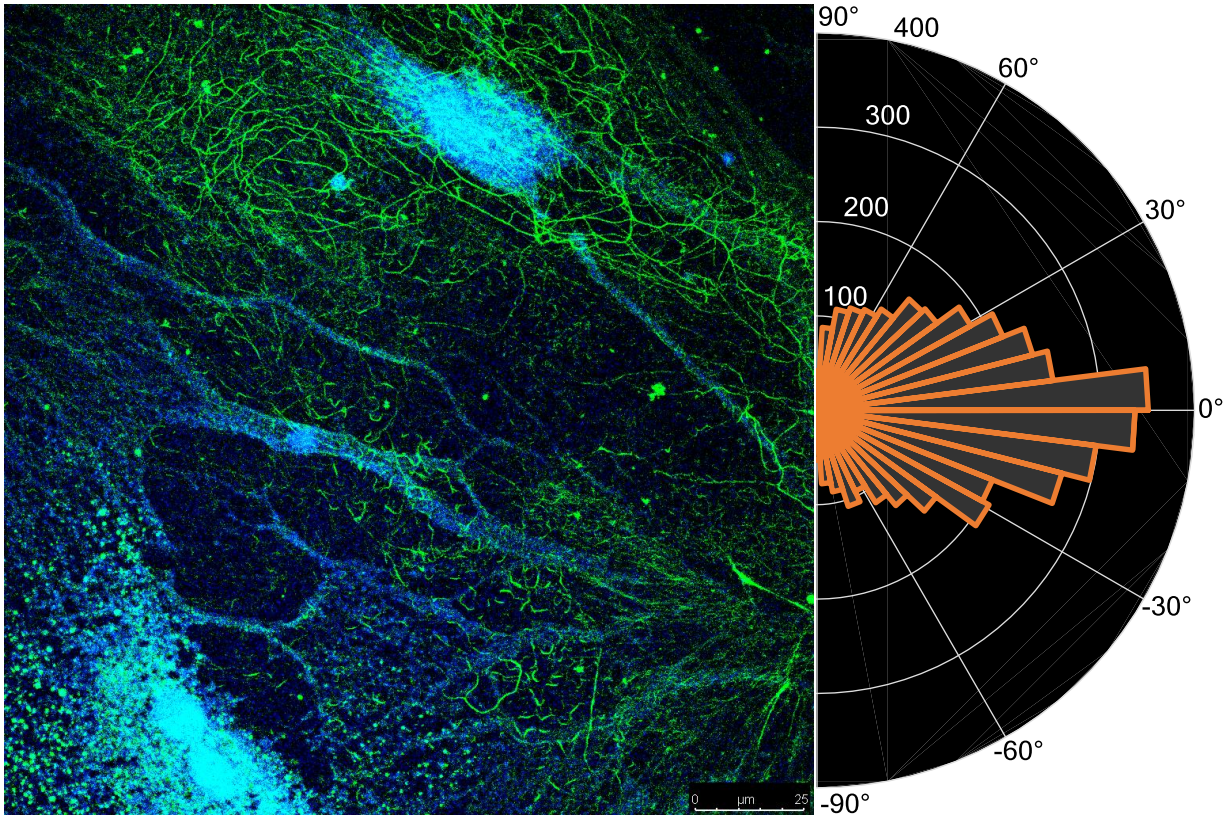

Figure 28: (left) Col1(α2)tpz primary murine dermal fibroblasts plated on an ibidi polymer plate pre-coated with aligned collagen substrate and cultured in MMC media for 7 days under no peptide (CTRL) conditions and stained for nuclei in blue with native GFPtpz expression in green. (right) Orientation analysis of the deposited collagen fibers from a single CTRL well reveals a preference for deposition along the pre-aligned collagen substrate.

Final focal adhesion distribution: In addition to nuclei and a confirmatory collagen 1 stain, day 7 fixed cells were also stained for paxillin, a focal adhesion protein. This protein was chosen due to the similarities between the unusual NIH 3T3 fibroblast migration dynamics observed in previous αCT1 experiments, of stretching very thin with a non-moving trailing edge before releasing it and rocketing forwards, was very similar to the migration dynamics found by Mrkonjic et al when they interfered with HEK293 cells' ability to recycle focal adhesions at the trailing edge[257]. While many of their findings were transient and would have required live-imaging transfected cells to confirm, one persistent finding was that interference with the recycling of focal adhesions at the trailing edge resulted in overall larger focal adhesions in the cells. If αCT1 does in fact induce the observed phenotype in fibroblasts by interfering with the recycling of focal adhesions at the trailing edge of the fibroblast, we should expect to see similarly large focal adhesions, as designated by the paxillin staining, in our αCT1-treated cell cultures.

Live-imaged fibroblast dynamics: The movement of the primary murine dermal fibroblasts, tracked by brightfield microscopy, in select fields of view from each experimental well were collected for at least 48 hours of the experimental period of 7 days. Previously, movement of NIH 3T3 fibroblasts plated on cell culture plastic was found to be affected by αCT1 treatment, increasing movement speed slightly and decreasing directionality in a dose-dependent fashion (Figure 4). It also resulted in an altered behavioral phenotype discussed above. Our current expectation is that the primary murine dermal fibroblasts will replicate these results, although early analysis seems to suggest that in general, the murine fibroblasts have a much more delayed migration speed than the NIH 3T3 fibroblasts.

Live-imaged collagen matrix assembly interaction with fibroblasts: Simultaneously to collecting the brightfield-imaged movement of the fibroblasts, GFPtpz fluorescence images were collected at designated timepoints. By directly comparing the movement of the fibroblasts with the Col1(α2)tpz fluorescence, we should be able to directly examine how the movement of the fibroblasts directly alters the construction of the collagen matrix.

References Cited

1. Gauglitz, G. G., Korting, H. C., Pavicic, T., Ruzicka, T. & Jeschke, M. G. Hypertrophic scarring and keloids: pathomechanisms and current and emerging treatment strategies. *Mol. Med.* **17**, 113–25.

2. Ferguson, M. W. *et al.* Prophylactic administration of avotermin for improvement of skin scarring: three double-blind, placebo-controlled, phase I/II studies. *Lancet* **373**, 1264–1274 (2009).

3. Weiser, T. G. *et al.* An estimation of the global volume of surgery: a modelling strategy based on available data. *Lancet* **372**, 139–144 (2008).

4. Scar Treatment Market - Global Study on Scar Treatment: Asia to Witness Highest Growth by 2022.

5. Rhett, J. M. *et al.* Novel therapies for scar reduction and regenerative healing of skin wounds. *Trends Biotechnol.* **26**, 173–80 (2008).

6. Bush, J. A. *et al.* Recommendations on clinical proof of efficacy for potential scar prevention and reduction therapies. *Wound Repair Regen.* **19 Suppl 1**, s32-7 (2011).

7. Tziotzios, C., Profyris, C. & Sterling, J. Cutaneous scarring: Pathophysiology, molecular mechanisms, and scar reduction therapeutics Part II. Strategies to reduce scar formation after dermatologic procedures. *J. Am. Acad. Dermatol.* **66**, 13–24; quiz 25–6 (2012).

8. Chittoria, R. K. & Padi, T. R. A prospective, randomized, placebo controlled, double blind study of silicone gel in prevention of hypertrophic scar at donor site of skin grafting. *J. Cutan. Aesthet. Surg.* **6**, 12–6 (2013).

9. Medhi, B., Sewal, R. K., Kaman, L., Kadhe, G. & Mane, A. Efficacy and safety of an advanced formula silicone gel for prevention of post-operative scars. *Dermatol. Ther. (Heidelb).* **3**, 157–67 (2013).

10. Nguyen, D. T., Orgill, D. P. & Murphy, G. F. Chapter 4: The Pathophysiologic Basis for Wound Healing and Cutaneous Regeneration. in *Biomaterials For Treating Skin Loss* 25–57 (Woodhead Publishing (UK/Europe) & CRC Press (US), 2009). doi:10.1016/S1369-7021(09)70141-5.

11. Singer, A. J. & Clark, R. A. F. Cutaneous Wound Healing. *N. Engl. J. Med.* **341**, 738–746 (1999).

12. *Wound healing and wound infection: theory and surgical practice*. (Appleton-Century-Crofts, 1980).

13. Roberts, A. B. & Sporn, M. B. Transforming growth factor-β. in *The molecular and cellular biology*

of wound repair (ed. Clark, R. A. F.) 275–308 (Plenum Press, 1996).

14. Xu, J. & Clark, R. A. Extracellular matrix alters PDGF regulation of fibroblast integrins. *J. Cell Biol.* **132**, 239–49 (1996).

15. Greiling, D. & Clark, R. A. Fibronectin provides a conduit for fibroblast transmigration from collagenous stroma into fibrin clot provisional matrix. *J. Cell Sci.* **110 (Pt 7)**, 861–70 (1997).

16. Clark, R. A., Nielsen, L. D., Welch, M. P. & McPherson, J. M. Collagen matrices attenuate the collagen-synthetic response of cultured fibroblasts to TGF-beta. *J. Cell Sci.* **108 (Pt 3)**, 1251–61 (1995).

17. Gray, A. J., Bishop, J. E., Reeves, J. T. & Laurent, G. J. A alpha and B beta chains of fibrinogen stimulate proliferation of human fibroblasts. *J. Cell Sci.* **104 (Pt 2)**, 409–13 (1993).

18. Werner, S. *et al.* The function of KGF in morphogenesis of epithelium and reepithelialization of wounds. *Science* **266**, 819–22 (1994).

19. Paladini, R. D., Takahashi, K., Bravo, N. S. & Coulombe, P. A. Onset of re-epithelialization after skin injury correlates with a reorganization of keratin filaments in wound edge keratinocytes: defining a potential role for keratin 16. *J. Cell Biol.* **132**, 381–97 (1996).

20. Welch, M. P., Odland, G. F. & Clark, R. A. Temporal relationships of F-actin bundle formation, collagen and fibronectin matrix assembly, and fibronectin receptor expression to wound contraction. *J. Cell Biol.* **110**, 133–45 (1990).

21. Desmoulière, A., Redard, M., Darby, I. & Gabbiani, G. Apoptosis mediates the decrease in cellularity during the transition between granulation tissue and scar. *Am. J. Pathol.* **146**, 56–66 (1995).

22. Gabbiani, G. The myofibroblast in wound healing and fibrocontractive diseases. *J. Pathol.* **200**, 500–503 (2003).

23. Schiro, J. A. *et al.* Integrin alpha 2 beta 1 (VLA-2) mediates reorganization and contraction of collagen matrices by human cells. *Cell* **67**, 403–10 (1991).

24. Montesano, R. & Orci, L. Transforming growth factor beta stimulates collagen-matrix contraction by fibroblasts: implications for wound healing. *Proc. Natl. Acad. Sci. U. S. A.* **85**, 4894–7 (1988).

25. Levenson, S. M. *et al.* The healing of rat skin wounds. *Ann. Surg.* **161**, 293–308 (1965).

26. Bailey, A. J. *et al.* Characterization of the collagen of human hypertrophic and normal scars. *Biochim. Biophys. Acta* **405**, 412–21 (1975).

27. Stephens, P. (Cardiff U. Chapter 1: Dysfunctional wound healing in chronic wounds. in *Advanced Wound Repair Therapies* (ed. Farrar, D.) 3–38 (Woodhead Publishing Limited, 2011).

28. Iqbal, A., Jan, A., Wajid, M. A. & Tariq, S. Management of Chronic Non-healing Wounds by Hirudotherapy. *World J. Plast. Surg.* **6**, 9–17 (2017).

29. Zhao, R., Liang, H., Clarke, E., Jackson, C. & Xue, M. Inflammation in Chronic Wounds. *Int. J. Mol. Sci.* **17**, (2016).

30. Sen, C. K. *et al.* Human skin wounds: A major and snowballing threat to public health and the economy. *Wound Repair Regen.* **17**, 763–771 (2009).

31. Diegelmann, R. F. & Evans, M. C. Wound healing: an overview of acute, fibrotic and delayed healing. *Front. Biosci.* **9**, 283 (2004).

32. Mast, B. A. & Schultz, G. S. Interactions of cytokines, growth factors, and proteases in acute and chronic wounds. *Wound Repair Regen.* **4**, 411–420 (1996).

33. Demidova-Rice, T. N., Hamblin, M. R. & Herman, I. M. Acute and Impaired Wound Healing. *Adv. Skin Wound Care* **25**, 304–314 (2012).

34. Han, G. & Ceilley, R. Chronic Wound Healing: A Review of Current Management and Treatments. *Adv. Ther.* **34**, 599–610 (2017).

35. Ashcroft, G. S., Mills, S. J. & Ashworth, J. J. Ageing and wound healing. *Biogerontology* **3**, 337–45 (2002).

36. Hawkins, H. Pathophysiology of the burn scar. in *Total Burn Care* (ed. Herndon, D.) (Saunders Elsevier, 2007).

37. Wheeland, R. Keloids and hypertrophic scars. in *Cutaneous Medicine and Surgery* (eds. Arndt, K., Robinson, J., Leboit, P. & Wintroub, B.) 900–905 (Saunders Elsevier, 1996).

38. Alster, T. S. & West, T. B. Treatment of Scars: A Review. *Ann. Plast. Surg.* **39**, 418–432 (1997).

39. Assad, D. L. Neoplasms, pseudoneoplasms, and hyperplasia of supporting tissue origin. in *Dermatology in General Medicine* (ed. Jeffers, JD; Englis, M.) 1198–99 (McGraw-Hill, 1993).

40. Muir, I. F. K. On the nature of keloid and hypertrophic scars. *Br. J. Plast. Surg.* **43**, 61–69 (1990).

41. Leventhal, D., Furr, M. & Reiter, D. Treatment of Keloids and Hypertrophic Scars. *Arch. Facial Plast. Surg.* **8**, 362–8 (2006).

42. Murray, J. C. Keloids and hypertrophic scars. *Clin. Dermatol.* **12**, 27–37.

43. Niessen, F. B., Spauwen, P. H. M., Schalkwijk, J. & Kon, M. On the Nature of Hypertrophic Scars and Keloids: A Review. *Plast. Reconstr. Surg.* **104**, 1435–1458 (1999).

44. Bayat, A., Arscott, G., Ollier, W. E. R., Mc Grouther, D. A. & Ferguson, M. W. J. Keloid disease: clinical relevance of single versus multiple site scars. *Br. J. Plast. Surg.* **58**, 28–37 (2005).

45. Marneros, A. G., Norris, J. E. C., Watanabe, S., Reichenberger, E. & Olsen, B. R. Genome Scans Provide Evidence for Keloid Susceptibility Loci on Chromosomes 2q23 and 7p11. *J. Invest. Dermatol.* **122**, 1126–1132 (2004).

46. Brown, J. J., Ollier, W. E. R., Thomson, W. & Bayat, A. Positive association of HLA-DRB1*15 with keloid disease in Caucasians. *Int. J. Immunogenet.* **35**, 303–307 (2008).

47. Slemp, A. E. & Kirschner, R. E. Keloids and scars: a review of keloids and scars, their pathogenesis, risk factors, and management. *Curr. Opin. Pediatr.* **18**, 396–402 (2006).

48. Profyris, C., Tziotzios, C. & Do Vale, I. Cutaneous scarring: Pathophysiology, molecular mechanisms, and scar reduction therapeutics Part I. The molecular basis of scar formation. *J. Am. Acad. Dermatol.* **66**, 1–10; quiz 11–2 (2012).

49. Sephel, G. C. & Woodward, S. C. Repair, regeneration, and fibrosis. in *Rubin's Pathology* (ed. Rubin, E.) 84–117 (Lippincott, Williams & Wilkins, 2001).

50. Ogawa, R. Keloid and Hypertrophic Scars Are the Result of Chronic Inflammation in the Reticular Dermis. *Int. J. Mol. Sci.* **18**, (2017).

51. Huang, C., Akaishi, S., Hyakusoku, H. & Ogawa, R. Are keloid and hypertrophic scar different forms of the same disorder? A fibroproliferative skin disorder hypothesis based on keloid findings. *Int. Wound J.* **11**, 517–22 (2014).

52. Reinke, J. M. & Sorg, H. Wound Repair and Regeneration. *Eur. Surg. Res.* **49**, 35–43 (2012).

53. Thulabandu, V., Chen, D. & Atit, R. P. Dermal fibroblast in cutaneous development and healing.

Wiley Interdiscip. Rev. Dev. Biol. **7**, (2018).

54. Jiang, X., Iseki, S., Maxson, R. E., Sucov, H. M. & Morriss-Kay, G. M. Tissue Origins and Interactions in the Mammalian Skull Vault. *Dev. Biol.* **241**, 106–116 (2002).

55. Yoshida, T., Vivatbutsiri, P., Morriss-Kay, G., Saga, Y. & Iseki, S. Cell lineage in mammalian craniofacial mesenchyme. *Mech. Dev.* **125**, 797–808 (2008).

56. Baker, C. V, Bronner-Fraser, M., Le Douarin, N. M. & Teillet, M. A. Early- and late-migrating cranial neural crest cell populations have equivalent developmental potential in vivo. *Development* **124**, 3077–87 (1997).

57. Atit, R. *et al.* β-catenin activation is necessary and sufficient to specify the dorsal dermal fate in the mouse. *Dev. Biol.* **296**, 164–176 (2006).

58. Ben-Yair, R., Kahane, N. & Kalcheim, C. Coherent development of dermomyotome and dermis from the entire mediolateral extent of the dorsal somite. *Development* **130**, 4325–4336 (2003).

59. Scaal, M. & Christ, B. Formation and differentiation of the avian dermomyotome. *Anat. Embryol. (Berl).* **208**, 411–24 (2004).

60. Ohtola, J. *et al.* -Catenin has sequential roles in the survival and specification of ventral dermis. *Development* **135**, 2321–2329 (2008).

61. Nowicki, J. L., Takimoto, R. & Burke, A. C. The lateral somitic frontier: dorso-ventral aspects of anterio-posterior regionalization in avian embryos. *Mech. Dev.* **120**, 227–40 (2003).

62. Fliniaux, I., Viallet, J. P. & Dhouailly, D. Signaling dynamics of feather tract formation from the chick somatopleure. *Development* **131**, 3955–3966 (2004).

63. Driskell, R. R. *et al.* Distinct fibroblast lineages determine dermal architecture in skin development and repair. *Nature* **504**, 277–281 (2013).

64. Chen, D., Jarrell, A., Guo, C., Lang, R. & Atit, R. Dermal -catenin activity in response to epidermal Wnt ligands is required for fibroblast proliferation and hair follicle initiation. *Development* **139**, 1522–1533 (2012).

65. Zhou, L., Yang, K., Wickett, R. R., Andl, T. & Zhang, Y. Dermal sheath cells contribute to postnatal hair follicle growth and cycling. *J. Dermatol. Sci.* **82**, 129–131 (2016).

66. Fujiwara, H. *et al.* The Basement Membrane of Hair Follicle Stem Cells Is a Muscle Cell Niche. *Cell* **144**, 577–589 (2011).

67. Jiang, T. X., Jung, H. S., Widelitz, R. B. & Chuong, C. M. Self-organization of periodic patterns by dissociated feather mesenchymal cells and the regulation of size, number and spacing of primordia. *Development* **126**, 4997–5009 (1999).

68. Hardy, M. H. The secret life of the hair follicle. *Trends Genet.* **8**, 55–61 (1992).

69. Rinkevich, Y. *et al.* Identification and isolation of a dermal lineage with intrinsic fibrogenic potential. *Science (80-.).* **348**, aaa2151–aaa2151 (2015).

70. Chang, H. Y. *et al.* Diversity, topographic differentiation, and positional memory in human fibroblasts. *Proc. Natl. Acad. Sci.* **99**, 12877–12882 (2002).

71. Rinn, J. L., Bondre, C., Gladstone, H. B., Brown, P. O. & Chang, H. Y. Anatomic Demarcation by Positional Variation in Fibroblast Gene Expression Programs. *PLoS Genet.* **2**, e119 (2006).

72. Collins, C. A., Kretzschmar, K. & Watt, F. M. Reprogramming adult dermis to a neonatal state through epidermal activation of -catenin. *Development* **138**, 5189–5199 (2011).

73. Wang, X. *et al.* Principles and mechanisms of regeneration in the mouse model for wound-induced hair follicle neogenesis. *Regeneration* **2**, 169–181 (2015).

74. Ito, M. *et al.* Wnt-dependent de novo hair follicle regeneration in adult mouse skin after wounding. *Nature* **447**, 316–320 (2007).

75. Plikus, M. V *et al.* Regeneration of fat cells from myofibroblasts during wound healing. *Science* **355**, 748–752 (2017).

76. Knezevic, V., Sim, A. J., Borg, T. K. & Holmes, J. W. Isotonic biaxial loading of fibroblast-populated collagen gels: A versatile, low-cost system for the study of mechanobiology. *Biomech. Model. Mechanobiol.* **1**, 59–67 (2002).

77. Wang, H., Abhilash, A. S., Chen, C. S., Wells, R. G. & Shenoy, V. B. Long Range Force Transmission in Fibrous Matrices Enabled by Tension-Driven Alignment of Fibers. *bioRxiv* 048579 (2016) doi:10.1101/048579.

78. Rouillard, A. D. & Holmes, J. W. Mechanical boundary conditions bias fibroblast invasion in a

collagen-fibrin wound model. *Biophys. J.* **106**, 932–43 (2014).

79. Vader, D., Kabla, A., Weitz, D. & Mahadevan, L. Strain-Induced Alignment in Collagen Gels. *PLoS One* **4**, e5902 (2009).

80. Wen, H., Blume, P. A. & Sumpio, B. E. Role of integrins and focal adhesion kinase in the orientation of dermal fibroblasts exposed to cyclic strain. *Int. Wound J.* **6**, 149–158 (2009).

81. Plotnikov, S. V & Waterman, C. M. Guiding cell migration by tugging. *Curr. Opin. Cell Biol.* **25**, 619–26 (2013).

82. Rid, R., Schiefermeier, N., Grigoriev, I., Small, J. V. & Kaverina, I. The last but not the least: The origin and significance of trailing adhesions in fibroblastic cells. *Cell Motil. Cytoskeleton* **61**, 161–171 (2005).

83. Friedland, J. C., Lee, M. H. & Boettiger, D. Mechanically Activated Integrin Switch Controls a 5 b 1 Function.

84. Jones, C. & Ehrlich, H. P. Fibroblast expression of α-smooth muscle actin, α2β1 integrin and αvβ3 integrin: Influence of surface rigidity. *Exp. Mol. Pathol.* **91**, 394–399 (2011).

85. Tracy, L. E., Minasian, R. A. & Caterson, E. J. Extracellular Matrix and Dermal Fibroblast Function in the Healing Wound. *Adv. wound care* **5**, 119–136 (2016).

86. Lygoe, K. A., Wall, I., Stephens, P. & Lewis, M. P. Role of vitronectin and fibronectin receptors in oral mucosal and dermal myofibroblast differentiation. *Biol. Cell* **99**, 601–614 (2007).

87. Leithe, E., Mesnil, M. & Aasen, T. The connexin 43 C-terminus: A tail of many tales. *Biochim. Biophys. Acta - Biomembr.* **1860**, 48–64 (2018).

88. Ambrosi, C. *et al.* Connexin43 Forms Supramolecular Complexes through Non-Overlapping Binding Sites for Drebrin, Tubulin, and ZO-1. *PLoS One* **11**, e0157073 (2016).

89. Axelsen, L. N., Calloe, K., Holstein-Rathlou, N.-H. & Nielsen, M. S. Managing the complexity of communication: regulation of gap junctions by post-translational modification. *Front. Pharmacol.* **4**, 130 (2013).

90. Chatterjee, B. *et al.* Developmental regulation and expression of the zebrafish connexin43 gene. *Dev. Dyn.* **233**, 890–906 (2005).

91. Bai, D. Structural analysis of key gap junction domains—Lessons from genome data and disease-linked mutants. *Semin. Cell Dev. Biol.* **50**, 74–82 (2016).

92. Hunter, A. W., Barker, R. J., Zhu, C. & Gourdie, R. G. Zonula Occludens-1 Alters Connexin43 Gap Junction Size and Organization by Influencing Channel Accretion. **16**, 5686–5698 (2005).

93. Lorraine, C., Wright, C. S. & Martin, P. E. Connexin43 plays diverse roles in co-ordinating cell migration and wound closure events. *Biochem. Soc. Trans.* **43**, 482–8 (2015).

94. Cogliati, B. *et al.* Connexin 43 deficiency accelerates skin wound healing and extracellular matrix remodeling in mice. *J. Dermatol. Sci.* **79**, 50–6 (2015).

95. Tarzemany, R., Jiang, G., Larjava, H. & Häkkinen, L. Expression and function of connexin 43 in human gingival wound healing and fibroblasts. *PLoS One* **10**, e0115524 (2015).

96. Scott, C. A., Tattersall, D., O'Toole, E. A. & Kelsell, D. P. Connexins in epidermal homeostasis and skin disease. *Biochim. Biophys. Acta* **1818**, 1952–61 (2012).

97. Gourdie, R. G. *et al.* The unstoppable connexin43 carboxyl-terminus: new roles in gap junction organization and wound healing. *Ann. N. Y. Acad. Sci.* **1080**, 49–62 (2006).

98. Ghatnekar, G. S. *et al.* Connexin43 carboxyl-terminal peptides reduce scar progenitor and promote regenerative healing following skin wounding. **4**, 205–223 (2009).

99. Rhett, J. M., Jourdan, J. & Gourdie, R. G. Connexin 43 connexon to gap junction transition is regulated by zonula occludens-1. *Mol. Biol. Cell* **22**, 1516–28 (2011).

100. Wright, C. S., Berends, R. F., Flint, D. J. & Martin, P. E. M. Cell motility in models of wounded human skin is improved by Gap27 despite raised glucose, insulin and IGFBP-5. *Exp. Cell Res.* **319**, 390–401 (2013).

101. Churko, J. M. *et al.* The G60S Cx43 mutant enhances keratinocyte proliferation and differentiation. *Exp. Dermatol.* **21**, 612–8 (2012).

102. Márquez-Rosado, L., Singh, D., Rincón-Arano, H., Solan, J. L. & Lampe, P. D. CASK (LIN2) interacts with Cx43 in wounded skin and their coexpression affects cell migration. *J. Cell Sci.* **125**, 695–702 (2012).

103. Qiu, C. *et al.* Targeting connexin43 expression accelerates the rate of wound repair. *Curr. Biol.* **13**,

1697–703 (2003).

104. Becker, D. L., Thrasivoulou, C. & Phillips, A. R. J. Connexins in wound healing; perspectives in diabetic patients. *Biochim. Biophys. Acta - Biomembr.* **1818**, 2068–2075 (2012).

105. Brandner, J. M., Houdek, P., Hüsing, B., Kaiser, C. & Moll, I. Connexins 26, 30, and 43: differences among spontaneous, chronic, and accelerated human wound healing. *J. Invest. Dermatol.* **122**, 1310–20 (2004).

106. Kretz, M. *et al.* Altered connexin expression and wound healing in the epidermis of connexin-deficient mice. *J. Cell Sci.* **116**, 3443–52 (2003).

107. Moore, K. *et al.* A synthetic connexin 43 mimetic peptide augments corneal wound healing. *Exp. Eye Res.* **115**, 178–88 (2013).

108. BIOTN-AN αCT1. Seq: Biotin-Ahx-RQIKIWFQNRRMKWKK-RPRPDDLEI. LifeTein LLC, Somerset, NJ USA.

109. Ghatnekar, G. S., Grek, C. L., Armstrong, D. G., Desai, S. C. & Gourdie, R. G. The effect of a connexin43-based Peptide on the healing of chronic venous leg ulcers: a multicenter, randomized trial. *J. Invest. Dermatol.* **135**, 289–98 (2015).

110. Grek, C. L. *et al.* Topical administration of a connexin43-based peptide augments healing of chronic neuropathic diabetic foot ulcers: A multicenter, randomized trial. *Wound Repair Regen.* **23**, 203–12 (2015).

111. Kirsner, R. S., Baquerizo Nole, K. L., Fox, J. D. & Liu, S. N. Healing refractory venous ulcers: new treatments offer hope. *J. Invest. Dermatol.* **135**, 19–23 (2015).

112. Montgomery, J., Ghatnekar, G. S., Grek, C. L., Moyer, K. E. & Gourdie, R. G. Connexin 43-Based Therapeutics for Dermal Wound Healing. *Int. J. Mol. Sci.* **19**, E1778 (2018).

113. Hunter, A. W., Barker, R. J., Zhu, C. & Gourdie, R. G. Zonula occludens-1 alters connexin43 gap junction size and organization by influencing channel accretion. *Mol. Biol. Cell* **16**, 5686–98 (2005).

114. Hunter, A. W., Jourdan, J. & Gourdie, R. G. Fusion of GFP to the Carboxyl Terminus of Connexin43 Increases Gap Junction Size in HeLa Cells. *Cell Commun. Adhes.* **10**, 211–214 (2003).

115. Jordan, K. *et al.* Trafficking, Assembly, and Function of a Connexin43-Green Fluorescent Protein

Chimera in Live Mammalian Cells. *Mol. Biol. Cell* **10**, 2033–2050 (1999).

116. O'Quinn, M. P., Palatinus, J. A., Harris, B. S., Hewett, K. W. & Gourdie, R. G. A peptide mimetic of the connexin43 carboxyl terminus reduces gap junction remodeling and induced arrhythmia following ventricular injury. *Circ. Res.* **108**, 704–15 (2011).

117. Jiang, J. *et al.* Phosphorylation of Connexin43 at Serine368 is Necessary for Induction of Cardioprotection by a Connexin43 Carboxyl-Terminal Mimetic Peptide. *Circulation* **134**, (2016).

118. Ongstad, E. L., O'Quinn, M. P., Ghatnekar, G. S., Yost, M. J. & Gourdie, R. G. A Connexin43 Mimetic Peptide Promotes Regenerative Healing and Improves Mechanical Properties in Skin and Heart. *Adv. wound care* **2**, 55–62 (2013).

119. Jiang, J. *et al.* Interaction of α Carboxyl Terminus 1 Peptide With the Connexin 43 Carboxyl Terminus Preserves Left Ventricular Function After Ischemia-Reperfusion Injury. *J. Am. Heart Assoc.* **8**, e012385 (2019).

120. Grek, C. L. *et al.* A Multicenter Randomized Controlled Trial Evaluating a Cx43-Mimetic Peptide in Cutaneous Scarring. *J. Invest. Dermatol.* **137**, 620–630 (2017).

121. Aperio Imagescope Software. Leica Biosystems Inc., Wetzlar DE. Version 12.0.

122. VS120 Virtual Slide Microscope. Olympus Corporation, Shinjuku, Tokyo JP.

123. MATLAB Release 2014a. The Mathworks, Inc., Natick, MA USA.

124. Rezakhaniha, R. *et al.* Experimental investigation of collagen waviness and orientation in the arterial adventitia using confocal laser scanning microscopy. *Biomech. Model. Mechanobiol.* **11**, 461–473 (2012).

125. Schneider, C. A., Rasband, W. S. & Eliceiri, K. W. NIH Image to ImageJ: 25 years of image analysis. *Nat. Methods* **9**, 671–675 (2012).

126. Sage, D. Biomedical Imaging Group - OrientationJ - A series of ImageJ plugins for directional image analysis. http://bigwww.epfl.ch/demo/orientation/ (2016).

127. Püspöki, Z., Storath, M., Sage, D. & Unser, M. Transforms and Operators for Directional Bioimage Analysis: A Survey. in *Advances in anatomy, embryology, and cell biology* vol. 219 69–93 (2016).

128. Fonck, E. *et al.* Effect of Aging on Elastin Functionality in Human Cerebral Arteries. *Stroke* **40**, 2552–

2556 (2009).

129. Entropy of grayscale image - MATLAB entropy. https://www.mathworks.com/help/images/ref/entropy.html (2005).

130. Gonzalez, R. C., Woods, R. E. & Eddins, S. L. *Digital Image Processing Using MATLAB*. (Prentice Hall, 2003).

131. Global image threshold using Otsu's method - MATLAB graythresh. https://www.mathworks.com/help/images/ref/graythresh.html (2005).

132. Otsu, N. A Threshold Selection Method from Gray-Level Histograms. *IEEE Trans. Syst. Man. Cybern.* **9**, 62–66 (1979).

133. Lattouf, R. *et al.* Picrosirius Red Staining. *J. Histochem. Cytochem.* **62**, 751–758 (2014).

134. Whittaker, L. R. P., Whittaker, P., Rich, L. & Whittaker, P. COLLAGEN AND PICROSIRIUS RED STAINING: A POLARIZED LIGHT ASSESSMENT OF FIBRILLAR HUE AND SPATIAL DISTRIBUTION. *J. Morphol. Sci.* **22**, 0–0 (2017).

135. JMP® Pro 12. SAS Institute Inc., Cary, NC USA.

136. Arduino Uno. Adafruit Industries, New York, NY USA.

137. Arduino IDE. Arduino Software, Somerville, MA USA.

138. MakerBot Replicator. MakerBot Industries LLC, Brooklyn, NY USA.

139. Optical Microscope Accessory Model U-CO1.25X. Olympus Corporation, Shinjuku, Tokyo JP.

140. Optical Microscope Accessory Model U-AN360-3. Olympus Corporation, Shinjuku, Tokyo JP.

141. Fomovsky, G. M. & Holmes, J. W. Evolution of scar structure, mechanics, and ventricular function after myocardial infarction in the rat. *Am. J. Physiol. Heart Circ. Physiol.* **298**, H221-8 (2010).

142. Adafruit Motor/Stepper/Servo Shield for Arduino. Adafruit Industries, New York, NY USA.

143. Normalized 2-D cross-correlation - MATLAB "normxcorr2" https://www.mathworks.com/help/images/ref/normxcorr2.html?s_tid=doc_ta (2005).

144. Haralick, R. M. & Shapiro, L. G. *Computer and Robot Vision*. (Addison-Wesley, 1992).

145. Lewis, J. P. Fast Normalized Cross-Correlation. *Ind. Light Magic* (1995).

146. Berens, P. CircStat: A Matlab Toolbox for Circular Statistics. *Jounral Stat. Softw.* **31**, (2009).

147. Zar, J. H. *Biostatistical Analysis*. (Prentice Hall, 1999).

148. Wegner, K. A., Keikhosravi, A., Eliceiri, K. W. & Vezina, C. M. Fluorescence of Picrosirius Red Multiplexed With Immunohistochemistry for the Quantitative Assessment of Collagen in Tissue Sections. *J. Histochem. Cytochem.* **65**, 479–490 (2017).

149. Moore, T. J., Zhang, H., Anderson, G. & Alexander, G. C. Estimated Costs of Pivotal Trials for Novel Therapeutic Agents Approved by the US Food and Drug Administration, 2015-2016. *JAMA Intern. Med.* **178**, 1451–1457 (2018).

150. Perez, R. & Davis, S. C. Relevance of animal models for wound healing. *Wounds a Compend. Clin. Res. Pract.* **20**, 3–8 (2008).

151. Sullivan, T. P., Eaglstein, W. H., Davis, S. C. & Mertz, P. THE PIG AS A MODEL FOR HUMAN WOUND HEALING. *Wound Repair Regen.* **9**, 66–76 (2001).

152. Seaton, M., Hocking, A. & Gibran, N. S. Porcine Models of Cutaneous Wound Healing. *ILAR J.* **56**, 127–138 (2015).

153. Grada, A., Mervis, J. & Falanga, V. Research Techniques Made Simple: Animal Models of Wound Healing. *J. Invest. Dermatol.* **138**, 2095-2105.e1 (2018).

154. Galiano, R. D., Michaels, J., Dobryansky, M., Levine, J. P. & Gurtner, G. C. Quantitative and reproducible murine model of excisional wound healing. *Wound Repair Regen.* **12**, 485–92 (2004).

155. Davidson, J. M., Yu, F. & Opalenik, S. R. Splinting Strategies to Overcome Confounding Wound Contraction in Experimental Animal Models. *Adv. wound care* **2**, 142–148 (2013).

156. Carlson, M. A., Longaker, M. T. & Thompson, J. S. Wound Splinting Regulates Granulation Tissue Survival 1. (2003) doi:10.1006/jsre.2002.6602.

157. SAS Sprague-Dawley Rat. Charles River Laboratories, Wilmington, MA USA. Strain #400. Sex: male, Weight: approx 225g.

158. Nad's Hypoallergenic Facial Wax Strips. SI&D Inc., Garden Grove, CA USA.

159. VEET® Ready-To-Use Wax Strip Kit Hair Remover. Reckitt Benckiser LLC, Parsippany, NJ USA.

160. Stretch Mesh Rat Jackets (small & medium sizes). Lomir Biomedical Inc.®, Malone, NY USA. Catalog #RJ01 & #RJ02.

161. Isothesia. Henry Schein Animal Health, Dublin, OH USA. NDC #11695-6776-2. Catalog #029405. Various Lots.

162. Buprenorphine SR™-LAB. ZooPharm, Fort Collins, CO USA.

163. Povidone Iodine Surgical Scrub Solution. Dynarex Corporation, Orangeburg, NY USA. NDC #67777-142. Catalog #1425. Various Lots.

164. All Purpose Krazy Glue®. Elmer's Products Inc., Westerville, OH USA. Catalog #KG585.

165. Unify® Nylon Surgical Sutures 4-0, 18", 13mm 3/8 Reverse Cutting. AD Surgical, Sunnyvale, CA USA. Catalog #S-N418R13. Various Lots.

166. Nikon SMZ1500 Dissection Microscope. Nikon Instruments Inc., Melville, NY USA.

167. Silicone Sheet (0.8 mm thickness, red). Grace™ Bio-Labs Inc., Bend, OR USA. Catalog #664182.

168. Silicone Sheet (0.6 mm thickness, red, one-sided adhesive). Grace™ Bio-Labs Inc., Bend, OR USA. Catalog #665581.

169. Silicone Sheet (1.7 mm thickness, red, one-sided adhesive). Grace™ Bio-Labs Inc., Bend, OR USA. Catalog #665283.

170. Silicone Sheet (2.5 mm thickness, red, one-sided adhesive). Grace™ Bio-Labs Inc., Bend, OR USA. Catalog #665384.

171. Silicone - Premium FDA Grade White - 60A (1/48" thickness). Rubber-Cal Inc., Santa Ana, CA USA. [no longer available].

172. M10 DIN 6797-A-A2 Stainless Steel External Tooth Lock Washer. W. W. Grainger Inc., Lake Forest, IL USA. Catalog #6FE53.

173. Miltex® Sterile Disposable Biopsy Punches, 5 mm. Integra® LifeSciences Inc., York, PA USA. Catalog #33-35. Various Lots.

174. Miltex® Sterile Disposable Biopsy Punches, 8 mm. Integra® LifeSciences Inc., York, PA USA. Catalog

#33-37. Various Lots.

175. Mayhew Pro 66000 Hollow Punch Set. Mayhew Steel Products Inc., Turners Falls, MA USA.

176. Natrosol 250HHX PHARM. Hercules Inc., Wilmington, DE USA. Catalog #C1910.

177. 10mm Acu-Punch® Biopsy Punches. Acuderm® Inc., Ft. Lauderdale, FL USA. Catalog #P1050. Various Lots.

178. Rimadyl® (carprofen) Injectable 50 mg/mL. Zoetis, Parsippany-Troy Hills, NJ USA. Catalog #4019447. NADA #141-199. Various Lots.

179. JMP® Pro 14. SAS Institute Inc., Cary, NC USA.

180. IAF Hairless Guinea Pig. Charles River Laboratories, Wilmington, MA USA. Strain #161. Sex: male, Weight: approx. 300g.

181. Sueki, H., Gammal, C., Kudoh, K. & Kligman, A. M. Hairless guinea pig skin: anatomical basis for studies of cutaneous biology. *Eur. J. Dermatology* **10**, 357–64 (2000).

182. Dermal Jackets for Guinea Pigs, small. Lomir Biomedical Inc.®, Malone, NY USA. Catalog #GP J1D.

183. NIGHTSEA® Model SFA-CY Stereo Microscope Fluorescence Adapter. BlueLine NDT LLC, Lexington, MA USA.

184. Barrier Filter Glasses Model FG-CY. BlueLine NDT LLC, Lexington, MA USA.

185. C57BL/6J Mouse. The Jackson Laboratory, Bar Harbor, ME USA. Strain #000664. Sex: both, Age: 6-8 weeks.

186. Trypsin from bovine pancreas Type I. Sigma-Aldritch Corporation, St. Louis, MO USA. Catalog #T8003-100MG. Lot #010M7005V.

187. Collagenase Type 1, 0.22 µm Filtered. Worthington Biochemical Corporation, Lakewood, NJ USA. Catalog #LS004214. Various Lots.

188. BD Falcon™ Cell Strainer, 70 µm Nylon. BD Biosciences, Bedford, MA USA. Catalog #352350. Various Lots.

189. BD Falcon™ Cell Strainer, 100 µm Nylon. BD Biosciences, Bedford, MA USA. Catalog #352360. Lot #0277392.

190. Dulbecco's Modified Eagle Medium (1X) + Glutamax™-I 500 mL. Gibco Laboratories, Gaithersburg, MD USA. Catalog #10569-010. Various Lots.

191. Newborn Calf Serum, 500 mL. Cambrex Bio Science Walkersville Inc., Walkersville, MD USA. Catalog #14-416F. Lot #01106776.

192. L-Ascorbic acid 2-phosphate sesquimagnesium salt hydrate. Sigma-Aldrich Corporation, St. Louis, MO USA. Catalog #A8960-5G. Lot #SLBB7986V.

193. Amphotericin B, 250 µg/mL. Life Technologies Corporation, Grand Island, NY USA. Catalog #15290-026. Various Lots.

194. Pen Strep – Penicillin Streptomycin (5000 U/mL). Life Technologies Corporation, Grand Island, NY USA. Catalog #15070-063. Lot #1292393.

195. Gentamicin Reagent Solution (50 mg/mL). Life Technologies Corporation, Grand Island, NY USA. Catalog #15750-060. Lot #1670580.

196. Sony SH800S Cell Sorter. Sony Biotechnology Inc., San Jose, CA USA.

197. µ-Slide 2 Well ibiTreat: #1.5 polymer coverslip, tissue culture treated, sterilized. ibidi GmbH, Martinsried, BY DE. Catalog #80286. Lot #190725/2.

198. Collagen Type I Rat Tail High Concentration. Discovery Labware Inc., Bedford, MA USA. Catalog #354249. Lot #7254002.

199. CytoOne® Cell Scraper 220 mm Long 11 mm Blade Sterile. USA Scientific Inc., Ocala, FL USA. Catalog #CC7600-0220. Lot #0991602.

200. Albumin from bovine serum. Sigma-Aldrich Corporation, St. Louis, MO USA. Catalog #A9085-5G. Lot #050M1629V.

201. Benny, P., Badowski, C., Lane, E. B. & Raghunath, M. Making More Matrix: Enhancing the Deposition of Dermal–Epidermal Junction Components *In Vitro* and Accelerating Organotypic Skin Culture Development, Using Macromolecular Crowding. *Tissue Eng. Part A* **21**, 183–192 (2015).

202. Kumar, P., Satyam, A., Cigognini, D., Pandit, A. & Zeugolis, D. I. Low oxygen tension and macromolecular crowding accelerate extracellular matrix deposition in human corneal fibroblast culture. *J. Tissue Eng. Regen. Med.* **12**, 6–18 (2018).

203. Chen, C. *et al.* The Scar-in-a-Jar: studying potential antifibrotic compounds from the epigenetic to extracellular level in a single well. *Br. J. Pharmacol.* **158**, 1196–1209 (2009).

204. Chen, C., Loe, F., Blocki, A., Peng, Y. & Raghunath, M. Applying macromolecular crowding to enhance extracellular matrix deposition and its remodeling in vitro for tissue engineering and cell-based therapies. *Adv. Drug Deliv. Rev.* **63**, 277–290 (2011).

205. Ficoll™ PM70. GE Healthcare Bio-Sciences AB, Uppsala SE. Catalog #17-0310-10. Lot #10259302.

206. Ficoll, Type 400. Sigma Chemical Company, St. Louis, MO USA. Catalog #F-4375. Lot #95H0189.

207. Sodium Pyruvate (100mM). Life Technologies Corporation, Grand Island, NY USA. Catalog #11360-070. Lot #1790960.

208. Cell Therapy Systems GlutaMAX™ - I CTS™ (100X). Gibco Laboratories, Gaithersburg, MD USA. Catalog #A12860-01. Lot #1997613.

209. DMEM (1X) - Dulbecco's Modified Eagle Medium. Life Technologies Limited, Paisley UK. Catalog #31053-028. Lot #2031649.

210. #3 ANT peptide. Seq: Biotin-Ahx-RQIKIWFQNRRMKWKK. LifeTein LLC, Somerset, NJ USA. Catalog #LT110949. Lot #LT190718-LT110949.

211. #1 RV aCT1 (RR-25) peptide. Seq: Biotin-Ahx-RQIKIWFQNRRMKWKK-IELDDPRPR. LifeTein LLC, Somerset, NJ USA. Catalog #716142. Lot #LT190326-LT716142.

212. PerkinElmer Ultraview. PerkinElmer LAS, Llantrisant UK. Serial #03UV069.

213. Volocity (64 bit). PerkinElmer Life Sciences Inc., Waltham, MA USA. Version 6.3.

214. The Cube Heating Unit. Life Imaging Services, Basel CH. Model #CB02A.

215. The Box Live Imaging Containment. Life Imaging Services, Basel CH. Model #CB02A.

216. Ion Laser Power Supply. Melles Griot Laser Group, Carlsbad, CA USA. Model #176B-240B-011.

217. Ion Laser. Melles Griot Laser Group, Carlsbad, CA USA. Model #543-PEA-A01.

218. NEOS Driver. Neos Technologies, Melbourne, FL USA. Model #64040-75-.1-.

219. CSU 10 Confocal Scanner Unit. Yokogawa Electric Corporation, Musashino, Tokyo JP.

220. Vibraplane. Kinetic Systems, Boston, MA USA. Model #120944-03.

221. PeCon Plate #500540 (ibidi μ-Slides). PeCon GmbH, Erbach DE.

222. Ultraview ProSync 2. PerkinElmer LAS, Llantrisant UK. Part #L7200321.

223. Zeiss Axiovert 200M. Carl Zeiss Werk Gottingen, Gottingen DE.

224. Hamamatsu Orca-ER Camera & Controller. Hamamatsu Photonics K.K., JP. Model #C4742-80-12AG.

225. Hamamatsu ImagEM EM-CCD Digital Camera & Controller. Hamamatsu Photonics K.K., JP. Model #C9100-13.

226. Lambda 10-2. Sutter Instrument Company, Novato, CA USA. Model #LB10-2.

227. Filter Switcher. Sutter Instrument Company, Novato, CA USA. Model #LB10W-2391.

228. ASI MS-2000-500. Applied Scientific Instrumentation Inc., Eugene, OR USA. Model #WK-XYBH-APZ15-AV200.

229. ASI MIV-2000. Applied Scientific Instrumentation Inc., Eugene, OR USA. Model #AV200HEMQ.

230. Hoechst 33342, trihydrochloride, trihydrate. Life Technologies Corporation, Eugene, OR USA. Catalog #H3570. Lot #2064462.

231. Rabbit anti-Mouse Type I Collagen Antibody. MD Biosciences, Oakdale, MD USA. Catalog #203002. Lot #366d.

232. Invitrogen Alexa Fluor™ 568 donkey anti-rabbit IgG (H&L). Life Technologies Corporation, Eugene, OR USA. Catalog #A10042. Lot #1964370.

233. Invitrogen Paxillin Monoclonal Antibody (PXC-10). Thermo Fisher Scientific Corporation, Carlsbad, CA USA. Catalog #MA1-24952. Lot #RK2296065.

234. Invitrogen Alexa Fluor™ 647 goat anti-mouse IgG1 (γ1). Life Technologies Corporation, Eugene, OR USA. Catalog #A21240. Lot #1885955.

235. Leica TCS SP8 X Confocal Microscope. Leica Microsystems, Wetzlar, HE DE.

236. Croley, J. A., Reese, V., Wagner, R. F. & Jr. Dermatologic Features of Classic Movie Villains: The Face of Evil. *JAMA dermatology* **153**, 559–564 (2017).

237. Horio, T., Miyauchi, H. & Asada, Y. The hairless guinea pig as an experimental animal for photodermatology. *Photodermatol. Photoimmunol. Photomed.* **8**, 69–72 (1991).

238. Hayes, B. B. *et al.* Evaluation of Percutaneous Penetration of Natural Rubber Latex Proteins. *Toxicol. Sci.* **56**, 262–270 (2000).

239. Miyauchi, H. & Horio, T. A New Animal Model for Contact Dermatitis: The Hairless Guinea Pig. *J. Dermatol.* **19**, 140–145 (1992).

240. Keikhosravi, A. *et al.* Quantification of collagen organization in histopathology samples using liquid crystal based polarization microscopy. *Biomed. Opt. Express* **8**, 4243–4256 (2017).

241. Beanes, S. R. *et al.* Confocal Microscopic Analysis of Scarless Repair in the Fetal Rat. *Plast. Reconstr. Surg.* **109**, 160–170 (2002).

242. Larson, B. J., Longaker, M. T. & Lorenz, H. P. Scarless Fetal Wound Healing: A Basic Science Review. *Plast. Reconstr. Surg.* **126**, 1172–1180 (2010).

243. Brant, J. O., Lopez, M.-C., Baker, H. V., Barbazuk, W. B. & Maden, M. A Comparative Analysis of Gene Expression Profiles during Skin Regeneration in Mus and Acomys. *PLoS One* **10**, e0142931 (2015).

244. Hsu, M., Peled, Z. M., Chin, G. S., Liu, W. & Longaker, M. T. Ontogeny of Expression of Transforming Growth Factor-β1 (TGF-β1), TGF-β3, and TGF-β Receptors I and II in Fetal Rat Fibroblasts and Skin. *Plast. Reconstr. Surg.* **107**, 1787–1794 (2001).

245. Krummel, T. M. *et al.* Transforming growth factor beta (TGF-beta) induces fibrosis in a fetal wound model. *J. Pediatr. Surg.* **23**, 647–52 (1988).

246. Lauer-Fields, J. L., Juska, D. & Fields, G. B. Matrix metalloproteinases and collagen catabolism. *Biopolymers* **66**, 19–32 (2002).

247. Seifert, A. W. *et al.* Skin shedding and tissue regeneration in African spiny mice (Acomys). *Nature* **489**, 561–565 (2012).

248. Dudley, E. S. & Boivin, G. P. Gastric volvulus in guinea pigs: comparison with other species. *J. Am. Assoc. Lab. Anim. Sci.* **50**, 526–30 (2011).

249. Canty, E. G. & Kadler, K. E. Procollagen trafficking, processing and fibrillogenesis. *J. Cell Sci.* **118**,

1341–53 (2005).

250. Griffith, L. G. & Swartz, M. A. Capturing complex 3D tissue physiology in vitro. *Nat. Rev. Mol. Cell Biol.* **7**, 211–224 (2006).

251. Sung, K. E. *et al.* Understanding the Impact of 2D and 3D Fibroblast Cultures on In Vitro Breast Cancer Models. *PLoS One* **8**, e76373 (2013).

252. Chen, Z., Yang, J., Wu, B. & Tawil, B. A Novel Three-Dimensional Wound Healing Model. *J. Dev. Biol.* **2**, 198–209 (2014).

253. Olk, S., Zoidl, G. & Dermietzel, R. Connexins, Cell Motility, and the Cytoskeleton. *Cell Motil. Cytoskelet.* **66**, 1000–1016 (2009).

254. Provenzano, P. P., Inman, D. R., Eliceiri, K. W., Trier, S. M. & Keely, P. J. Contact guidance mediated three-dimensional cell migration is regulated by Rho/ROCK-dependent matrix reorganization. *Biophys. J.* **95**, 5374–84 (2008).

255. Kubow, K. E., Shuklis, V. D., Sales, D. J. & Horwitz, A. R. Contact guidance persists under myosin inhibition due to the local alignment of adhesions and individual protrusions. *Sci. Rep.* **7**, 14380 (2017).

256. Rouillard, A. D. & Holmes, J. W. Mechanical boundary conditions bias fibroblast invasion in a collagen-fibrin wound model. *Biophys. J.* **106**, 932–943 (2014).

257. Mrkonjić, S. *et al.* TRPV4 participates in the establishment of trailing adhesions and directional persistence of migrating cells. *Pflügers Arch. - Eur. J. Physiol.* **467**, 2107–2119 (2015).